

Observation of the decay mode

$$K_L \rightarrow \pi^+ \pi^- e^+ e^-$$

Yuji Takeuchi

January, 2000

A dissertation submitted

by

Yuji Takeuchi

to

The Graduate School

in Partial Fulfillment of Requirements

for the Degree of

Doctor of Science(physics)

in

Department of Physics

Faculty of Science

Kyoto University

Abstract

Observation of the $K_L \rightarrow \pi^+\pi^-e^+e^-$ mode and measurement of its branching ratio are presented in this thesis. In this decay mode, CP violation is expected to occur as an interference between two intermediate states with different CP properties: one is an internal bremsstrahlung associated with the CP violating $K_L \rightarrow \pi^+\pi^-$ decay, and the other is a direct emission process characterized by the CP conserving magnetic dipole transition. Thus it can provide a new testing ground for investigating CP violation. Prior to the experiment, only an upper limit was given to the branching ratio. Thus our main purpose was to establish its existence experimentally and to measure the branching ratio.

The experiment was performed with a neutral K^0 line at the 12 GeV proton synchrotron (KEK). The detector consisted of a magnetic spectrometer and a pure-CsI electromagnetic calorimeter. The former measured the momentum and track of a charged particle, and the latter determined the energy and position of an electromagnetic component (e^\pm and γ).

The data presented in this thesis were taken in 1996 and 1997, and the analysis followed subsequently. We observed 15 $K_L \rightarrow \pi^+\pi^-e^+e^-$ events with an expected background of 1.5 events. We also obtained 12212 $K_L \rightarrow \pi^+\pi^-\pi^0(\pi^0 \rightarrow e^+e^-\gamma)$ events; they were used to determine the incident K_L flux and various detector efficiencies.

Based on the 13.5 events observed as the $K_L \rightarrow \pi^+\pi^-e^+e^-$ mode, its branching ratio is measured to be

$$Br(K_L \rightarrow \pi^+\pi^-e^+e^-) = (4.4 \pm 1.3(\text{stat.}) \pm 0.5(\text{syst.})) \times 10^{-7} ,$$

where the first error is statistical and the second is systematic. This result agrees well with the theoretical prediction and the recent experimental measurement based on 36.6 ± 6.8 observed events at FNAL.

Contents

1	Introduction	1
1.1	Theoretical Interest	2
1.2	Experimental Status	7
2	Experimental Apparatus	9
2.1	Beam Line	9
2.2	Decay Volume	11
2.3	E162 Detector	12
2.3.1	Spectrometer	12
2.3.2	Electromagnetic Calorimeter	18
2.3.3	Gas Čerenkov Counter	21
2.3.4	Trigger Scintillation Counters	22
2.4	Trigger System	27
2.5	Data Acquisition System	33
3	Event Reconstruction	37
3.1	Track Reconstruction	37
3.1.1	Calibration of Drift Chambers	37
3.1.2	Track Search	39
3.2	Momentum of Charged Particles	44
3.3	Calorimetry	46
3.3.1	Energy Calibration	46
3.3.2	Cluster Finding and Cluster Position	47
3.3.3	Timing Requirement	50
3.4	Particle Identification	52
3.5	Pre-selection	54
3.6	Decay Vertex determination	55
3.6.1	Determination of Track-Vertex Resolution	56
3.6.2	Calculation of Vertex χ^2	58

4	Analysis of the Physics Modes	59
4.1	General Event Selection	59
4.1.1	Event Topology Selection	61
4.1.2	Loose Kinematical Cut	62
4.1.3	Backgrounds Rejection	63
4.2	Analysis of the Normalization mode $K_L \rightarrow \pi^+\pi^-\pi_D^0$	67
4.2.1	Reconstruction of $K_L \rightarrow \pi^+\pi^-\pi_D^0$	69
4.3	Analysis of the Signal mode $K_L \rightarrow \pi^+\pi^-e^+e^-$	74
4.3.1	π^0 Inclusive Cut	75
4.3.2	Backgrounds from $K_L \rightarrow \pi^+\pi^-\pi_D^0$ with missing γ	76
4.3.3	Signal Identification and Background Subtraction	79
4.4	Calculation of the Branching Ratio	82
4.5	Discussions on Systematic Error	86
4.5.1	Acceptance-efficiency Calculations	87
4.5.2	Estimation of the Number of the Events	92
4.5.3	Systematic Error from Other Sources	94
4.5.4	Summary of Systematic Errors	94
5	Conclusion	95
A	Monte Carlo Simulation	97
A.1	K_L Production and decays	97
A.2	System Cross Check	99

List of Tables

2.1	Physics and calibration trigger modes.	29
2.2	Level 1 trigger hit requirements.	31
2.3	Level 2 trigger logics	32
2.4	Trigger rates (Vacuum Run).	32
2.5	Contents of the data.	36
4.1	Number of events (N)	83
4.2	Detector acceptance (A)	83
4.3	Analysis efficiencies (η)	84
4.4	stability of the background subtraction	93
4.5	Summary of systematic errors in the branching ratio.	94

List of Figures

1.1	Diagrams contributing to $\pi^+\pi^-\gamma^*$	3
1.2	Schematic drawing for the definition of the angle ϕ , which is the angle between planes normal to the e^+e^- and $\pi^+\pi^-$ planes.	5
2.1	Side view of the neutral beam line : K0 line.	10
2.2	Schematic view of E162 detector system.	13
2.3	The structure of drift chamber, (a) schematic view of the arrangement and (b) the cell structure.	15
2.4	The pre-amplifier for drift chambers.	16
2.5	Examples of the drift chamber performance: (a) Efficiencies and (b) Position resolution.	17
2.6	Schematic drawing of the calorimeter.	20
2.7	The side view of GC sliced at X=0.	21
2.8	Electron efficiency and pion rejection factor of GC as a function of the threshold for light output.	23
2.9	The trigger counter plane TC0X.	24
2.10	Schematic diagram of TC0 output.	25
2.11	The efficiency of TC0X	26
2.12	The trigger counter plane TC1X.	27
2.13	The trigger counter plane TC2X and 2Y.	28
2.14	The trigger counter plane TC3X.	30
2.15	The DAQ system in E162 experiment.	34
3.1	(a) A typical drift chamber TDC distribution and (b) its cumulative distribution.	38
3.2	Schematic view of pair-hit search	40
3.3	Schematic view of track search procedure	42
3.4	Track C.L. distribution of 12 layer fitting.	44
3.5	The cut value of $DXMAG$ as a function of momentum	45
3.6	E/p distribution of all blocks for electrons.	47
3.7	Schematic drawings of the cluster finding procedure.	48

3.8	X position of electrons measured by drift chambers vs that by the center of gravity of a cluster in the calorimeter.	49
3.9	Position resolution of the calorimeter for electrons in the X-view.	50
3.10	TDC distributions of the block in the calorimeter.	51
3.11	Scatter plots which indicate distance between track position and cluster position for (a) MC and (b) one set of data.	52
3.12	E/p distribution for pions.	53
3.13	E/p distribution for the actual data	54
3.14	The distribution of a cross point Z position.	55
3.15	Track-vertex resolution as a function of Z position.	57
3.16	Resolution of (a) $d_e/(z_0 - z)$ and (b) $d_\pi/(z_0 - z)$ as a function of track momentum.	57
3.17	χ_v^2 distribution of $K_L \rightarrow \pi^+\pi^-\pi_D^0$ events without χ_v^2 cut.	58
4.1	Schematic flowchart of the analysis.	60
4.2	Vertex χ^2 distributions for the data, the $K_L \rightarrow \pi^+\pi^-e^+e^-$ MC and $K_L \rightarrow \pi^+\pi^-\pi_D^0$ MC	62
4.3	Definition of the target reconstruction angle θ	63
4.4	M_{ee} distributions.	64
4.5	N_{shared} distributions.	66
4.6	A_{+-} distributions.	68
4.7	$M_{ee\gamma}$ distribution for $K_L \rightarrow \pi^+\pi^-\pi_D^0$ candidates.	69
4.8	$M_{\pi\pi ee\gamma}$ distribution for $K_L \rightarrow \pi^+\pi^-\pi_D^0$ candidates.	70
4.9	(a) θ_x and (b) θ_y distributions of $K_L \rightarrow \pi^+\pi^-\pi_D^0$ candidates.	71
4.10	θ^2 distribution of $K_L \rightarrow \pi^+\pi^-\pi_D^0$ candidates.	72
4.11	θ^2 vs $M_{\pi\pi ee\gamma}$ scatter plot after M_{π^0} cut.	73
4.12	The scatter plot of θ^2 vs $M_{\pi\pi ee}$ with the signal region.	74
4.13	The scatter plot of $M_{ee\gamma}$ vs $M_{\pi\pi ee}$	75
4.14	$\sqrt{\chi_D^2}$ distributions of the reconstructed $\pi^+\pi^-\pi_D^0$	77
4.15	$\sqrt{\chi_D^2}$ distributions of $\pi^+\pi^-e^+e^-$ candidates.	77
4.16	The $\sqrt{\chi_D^2}$ distributions.	78
4.17	The θ^2 vs $M_{\pi\pi ee}$ scatter plot after the χ_D^2 cut.	79
4.18	The number of background events in $M_{\pi\pi ee}-\theta^2$ plane.	80
4.19	The θ^2 projection.	81
4.20	The reconstructed K_L momentum distributions.	87
4.21	(a) The z vertex distributions and (b)The $A \cdot \eta$ ratio of two mode.	89
4.22	(a) Efficiency ratio ε_{acc} and (b) ε_{acc} ratio of the normalization to signal mode as a function of beam intensity.	90
4.23	Over-veto probability by π^0 inclusive cut.	92

A.1	K_L momentum spectrum employed in the Monte Carlo simulation.	98
A.2	The comparison of e^+ and e^- momentum distribution for the $K_L \rightarrow \pi^+\pi^-\pi_D^0$ events.	99
A.3	The comparison of π^+ and π^- momentum distribution for the $K_L \rightarrow \pi^+\pi^-\pi_D^0$ events.	100
A.4	The comparison of M_{ee} distribution for the $K_L \rightarrow \pi^+\pi^-\pi_D^0$ events.	100
A.5	The comparison of M_{pp} distribution for the $K_L \rightarrow \pi^+\pi^-\pi_D^0$ events.	101

Acknowledgements

This thesis could not have been written without the help and support of many people. First and foremost I would like to thank my supervisor, Prof. Noboru Sasao, for his time, effort, and many useful advice. He gave me a chance to be engaged in high energy physics, and I could gain precious experience in design and construction of a thin and high rate hodoscope counter, TC0, for the first two years, as well as the physics analysis. All of them were very challenging works.

I would like to thank all the collaborators of the KEK-E162. Prof. H. Sakamoto and Dr. T. Nomura, who are staffs in Kyoto HE group, and Prof. Y. Hemmi and Prof. H. Kurashige, who were staffs in Kyoto HE group, gave me various essential advices and suggestions. Prof. Y. Fukushima, Dr. T. Taniguchi, Dr. Y. Ikegami and Mr. T. T. Nakamura, who belong to KEK, and Prof. M. Asai, who is the staff of Hiroshima Institute of Technology, gave great helps for me to finish this work. Especially, I owe analysis methods in this thesis to T. Nomura's prior works. Mr. M. Suehiro, Mr. Y. Matono, Mr. K. Murakami, who are graduate students of Kyoto HE group, gave me their friendship and generous supports.

Needless to say, I would like to thank to also former members of the experiment and the other members of Kyoto HE group for their help.

Thanks also to Professors H. Sugawara, S. Yamada, S. Iwata, K. Nakai, and K. Nakamura of KEK for their support and encouragement. I also acknowledge the support from the operating crew of the Proton Synchrotron, the members of Beam Channel group, Computing Center and Mechanical Engineering Center at KEK, in particular Mr. Y. Higashi, Mr. Y. Funahashi and Mr. S. Koike for their contributions in construction of the detector.

I would like to acknowledge receipt of Research Fellowships of the Japan Society for the Promotion of Science for Young Scientists (F.Y.1996–1998).

Finally, a special thanks goes to my family for their endless support, patience and encouragement.

Chapter 1

Introduction

Since the discovery of CP violation in the $K_L \rightarrow 2\pi$ mode [1] in 1964, understanding of its phenomena and origin has been a high priority both in theoretical and experimental particle physics. Up to the present time, its evidence comes only from K^0 decay, i.e. CP violation is observed in the specific K^0 decay modes in spite of numerous experimental efforts. In the theoretical field, many models have been published after its discovery. To name some, a superweak model [2] has sought for its origin in a new $\Delta S = 2$ interaction. The model still remains consistent with all existing data.¹ In another model, the Higgs sector was claimed to be a source of CP violation [5, 6]. Although the model has been excluded experimentally as its sole origin, it still presents viable as well as interesting possibilities. It is now widely believed that CP violation can be explained by the Kobayashi-Maskawa model [7]. According to the model, a complex phase in the quark mixing matrix (CKM matrix) induces the CP and/or T violation phenomena. We should stress that, although it is accepted as an essential part of the Standard Model, it has not been proven experimentally. Therefore, it is indispensable to establish CP violation in other system, for example, in the $B^0 - \bar{B}^0$ system and other K_L decay channels.

The decay mode $K_L \rightarrow \pi^+\pi^-e^+e^-$ may provide an interesting testing ground for investigating CP violation,² as described in next section. The purpose of this study is to observe a clear evidence of the decay mode $K_L \rightarrow \pi^+\pi^-e^+e^-$ and to establish its branching ratio as a foundation of new testing field for CP violation.

In this thesis, an experimental measurement of its branching ratio, con-

¹This model was most recently disclaimed by the existence of Direct CP violation which was established via the observation of undoubted non-zero ϵ'/ϵ in recent experiments [3, 4].

²In August, 1999, KTeV group reported the observation of the CP violation in $K_L \rightarrow \pi^+\pi^-e^+e^-$ decays [8].

ducted with 12-GeV/c proton synchrotron at High Energy Accelerator Research Organization (KEK), is presented. The data used in this thesis, which were almost all data available to analysis, were taken in two distinctive time periods. One is “Helium” run and the other is “Vacuum” run, which represent the condition of the decay volume, respectively (see Section 2.2). Specifically, data in the Helium run was taken during five weeks, spanning three beam cycles, before summer in 1996, while data in the Vacuum run was taken during about ten weeks, spanning five beam cycles, from January to June in 1997.

This thesis is organized as follows. At first, the physics motivation and the experimental status are introduced in this chapter. The experimental apparatus is presented in Chapter 2. Chapter 3 deals with events reconstruction, i.e. a procedure to obtain physics quantities from raw data. In Chapter 4, the analysis of the two physics modes, $K_L \rightarrow \pi^+\pi^-e^+e^-$ and $K_L \rightarrow \pi^+\pi^-\pi^0(\pi^0 \rightarrow e^+e^-\gamma)$, is described in detail. The latter modes, denoted as $K_L \rightarrow \pi^+\pi^-\pi_D^0$, is used to determine the incident K_L flux and various detector efficiencies. Having established the signal, we present the calculation of branching ratio and estimation of systematic errors. Finally, Chapter 5 summarizes the present experiment. The detailed description of Monte Carlo simulation is given in Appendix A.

1.1 Theoretical Interest

The decay $K_L \rightarrow \pi^+\pi^-e^+e^-$ is expected to occur via $\pi^+\pi^-\gamma^*$ intermediate state converting the virtual photon into an e^+e^- pair.

Prior to our signal mode $K_L \rightarrow \pi^+\pi^-e^+e^-$, the CP property of the decay $K_L \rightarrow \pi^+\pi^-\gamma$ is considered, which is closely related to the signal mode. In case of real γ , it was measured experimentally that the amplitude contains two components in view of the photon emission mechanism [9]. One is an internal bremsstrahlung (IB) associated with the $K_L \rightarrow \pi^+\pi^-$ and the other is a direct emission (DE), which are seen in Figure 1.1(a) and (b), substituting γ^* for real γ . The photon emission by electric and magnetic multipoles (EJ and MJ, where J denotes the angular momentum), has $CP = (-1)^{J+1}$ and $CP = (-1)^J$ eigenstate, respectively. The internal bremsstrahlung amplitude can be expressed by a form equivalent to the EJ term with odd J. Since $\pi^+\pi^-$ system is always a CP-even state, the final state $\pi^+\pi^-\gamma$ has both $CP = +1$ and -1 states, corresponding to IB/E1 and M1 contributions respectively, in the approximation of retaining only dipole terms in direct emission. The interference between these two different CP states, however,

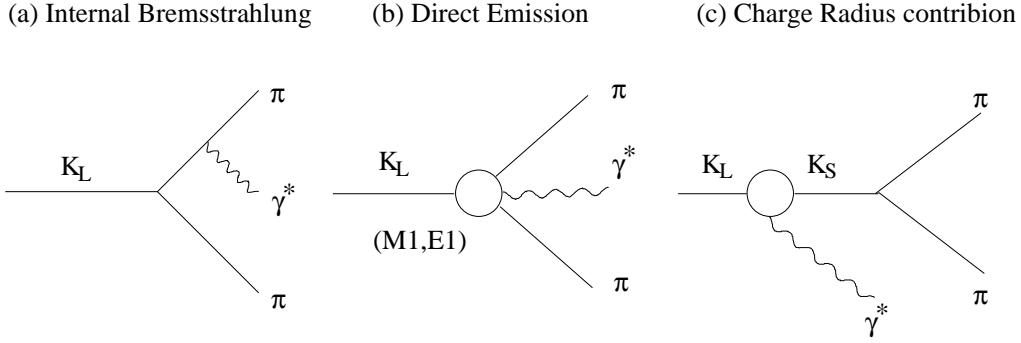


Figure 1.1: Contributions to $\pi^+\pi^-\gamma^*$ from (a) internal bremsstrahlung, (b) direct M1 or E1 emission and (c) K^0 charge radius.

doesn't appear if the photon polarization is not measured. Thus, in order to study CP violation experimentally in this mode, we must measure the photon polarization directly or indirectly.

On the other hand, in this respect, we have a good probe of the photon polarization in the case of the $\pi^+\pi^-e^+e^-$ mode, that is its internal conversion process. The photon polarization can be measured indirectly by studying the correlation of the e^+e^- plane relative to the $\pi^+\pi^-$ plane, and CP violating interference is unveiled. Calculations of the decay $K_L \rightarrow \pi^+\pi^-e^+e^-$ have been carried out in several papers [10]. Along their procedure, calculations and results are reviewed below.

The matrix element of the decay $K_L \rightarrow \pi^+\pi^-e^+e^-$ is represented as

$$\mathcal{M}(K_L \rightarrow \pi^+\pi^-e^+e^-) = \mathcal{M}_{IB} + \mathcal{M}_{DE}^{M1} + \mathcal{M}_{DE}^{E1} + \mathcal{M}_{CR}, \quad (1.1)$$

where the term \mathcal{M}_{IB} denotes the internal bremsstrahlung amplitude, and \mathcal{M}_{DE}^{E1} and \mathcal{M}_{DE}^{M1} are direct emission amplitudes for electric- and magnetic-dipole radiation, respectively. An additional term \mathcal{M}_{CR} is the contribution of the K^0 charge radius, illustrated in Fig.1.1(c), which can contribute when the photon is virtual.

Here we use the notation: $K_L(\mathcal{P}) \rightarrow \pi^+(p_+)\pi^-(p_-)e^+(k_+)e^-(k_-)$, then the matrix element can be written as

$$\begin{aligned} & \mathcal{M}(K_L \rightarrow \pi^+\pi^-e^+e^-) \\ &= e|f_s| \left[g_{IB} \left[\frac{p_{+\mu}}{p_+ \cdot k} - \frac{p_{-\mu}}{p_- \cdot k} \right] \right. \\ &+ \left. \frac{g_{E1}}{m_K^4} [(\mathcal{P} \cdot k)p_{+\mu} - (p_+ \cdot k)\mathcal{P}_\mu] \right] \end{aligned}$$

$$\begin{aligned}
& + \frac{g_{M1}}{m_K^4} \epsilon_{\mu\nu\rho\sigma} k^\nu p_+^\rho p_-^\sigma \\
& + \frac{g_{CR}}{m_K^2} \left[k^2 \mathcal{P}_\mu - (\mathcal{P} \cdot k) k_\mu \right] \frac{1}{k^2 - 2\mathcal{P} \cdot k} \left] \frac{e}{k^2} \bar{u}(k_-) \gamma^\mu v(k_+), \quad (1.2)
\end{aligned}$$

where $k = k_+ + k_-$. The parameters in the above expression are defined as follows;

- (a) f_s is the coupling constant for $K_S \rightarrow \pi^+ \pi^-$ defined by

$$\Gamma(K_S \rightarrow \pi^+ \pi^-) = \frac{|f_s|^2}{16\pi m_K} \left[1 - \frac{4m_\pi^2}{m_K^2} \right]^{1/2}. \quad (1.3)$$

- (b) The parameter g_{IB} defines the internal bremsstrahlung. It is given by $g_{IB} = \eta_{+-} \cdot f_s / |f_s|$, where η_{+-} is the CP violating parameter, $A(K_L \rightarrow \pi^+ \pi^-) / A(K_S \rightarrow \pi^+ \pi^-)$. The phase of g_{IB} is $\Phi_{+-} + \delta_0$, where Φ_{+-} is the phase of η_{+-} and δ_0 is the $I = 0$ $\pi\pi$ s-wave phase shift at $\sqrt{s_\pi} = m_K$ ($\delta_0(m_K^2)$). Here s_π is the square of the $\pi\pi$ invariant mass, i.e. $s_\pi = (p_+ + p_-)^2$. g_{IB} is rewritten as

$$g_{IB} = \eta_{+-} e^{i\delta_0(m_K^2)}, \quad (1.4)$$

- (c) The parameter g_{M1} defines the direct M1 radiation. The absolute value of g_{M1} is measured by the decay rate of the M1 radiation in the $K_L \rightarrow \pi^+ \pi^- \gamma$, and one obtained $|g_{M1}| = 0.76$. The phase of g_{M1} is that of p-wave $I = 1$ $\pi\pi$ scattering at $\sqrt{s_\pi}$ ($\delta_1(s_\pi)$) and also factor of i as a consequence of CPT invariance. g_{M1} is rewritten as

$$g_{M1} = i(0.76) e^{i\delta_1(s_\pi)}, \quad (1.5)$$

- (d) The parameter g_{E1} was estimated to be small in Ref.[10], compared with g_{M1} and/or g_{IB} . Also the parameter g_{CR} resulted in small contribution. So detail explanation of them is skipped here.

From the matrix element in Eq.(1.2), differential decay rate is calculated in three variables:

- (i) $x = (p_+ + p_-)^2 / m_K^2$ (normalized invariant mass of pions),
- (ii) $y = (k_+ + k_-)^2 / m_K^2$ (normalized invariant mass of electrons), and
- (iii) ϕ (the angle between normals to the $e^+ e^-$ and $\pi^+ \pi^-$ planes).

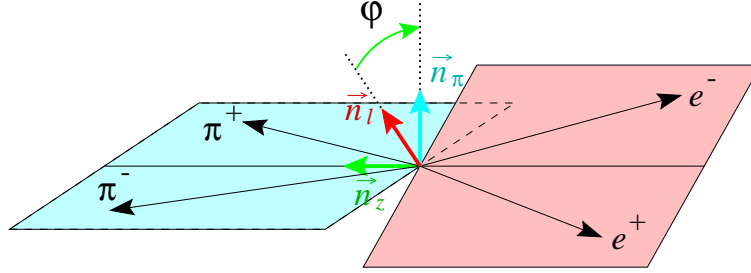


Figure 1.2: Schematic drawing for the definition of the angle ϕ , which is the angle between planes normal to the e^+e^- and $\pi^+\pi^-$ planes.

The last variable ϕ , illustrated in Fig.1.2, is determined as follows. Let $(\vec{p}_+ + \vec{p}_-)$ be parallel to the positive z direction in the K_L rest frame. Then the unit vector pointing to the $+z$ direction is represented as

$$\vec{n}_z = (\vec{p}_+ + \vec{p}_-) / |(\vec{p}_+ + \vec{p}_-)| . \quad (1.6)$$

The unit vectors normal to the $\pi^+\pi^-$ plane

$$\vec{n}_\pi = (\vec{p}_+ \times \vec{p}_-) / |(\vec{p}_+ \times \vec{p}_-)| \quad (1.7)$$

and to the e^+e^- plane

$$\vec{n}_l = (\vec{k}_+ \times \vec{k}_-) / |(\vec{k}_+ \times \vec{k}_-)| \quad (1.8)$$

then lie in the x - y plane and have components

$$\vec{n}_\pi = (\cos \phi_\pi, \sin \phi_\pi, 0) ,$$

$$\vec{n}_l = (\cos \phi_l, \sin \phi_l, 0) ,$$

where ϕ_π and ϕ_l lie between 0 to 2π . The angle ϕ is defined as

$$\phi = (\phi_\pi - \phi_l) \text{mod}(2\pi)$$

and ranges from 0 to 2π . Note that the relation between the angle ϕ and the unit vectors can be written as

$$\cos \phi = \vec{n}_l \cdot \vec{n}_\pi , \quad (1.9)$$

$$\sin \phi = (\vec{n}_l \times \vec{n}_\pi) \cdot \vec{n}_z . \quad (1.10)$$

The result for the decay rate, normalized by that of $K_S \rightarrow \pi^+\pi^-$, is

$$\begin{aligned} & \frac{\Gamma(K_L \rightarrow \pi^+\pi^-e^+e^-)}{\Gamma(K_S \rightarrow \pi^+\pi^-)} \\ &= \frac{\alpha^2}{16\pi^2\lambda^{1/2}(1, \mu^2, \mu^2)} \int_{4\nu^2}^{(1-2\mu)^2} dy \frac{\lambda^{1/2}(y, \nu^2, \nu^2)}{y^2} \\ & \quad \int_{4\mu^2}^{(1-\sqrt{y})^2} dx \lambda^{1/2}(1, x, y) \int_0^{2\pi} \frac{d\phi}{2\pi} F(x, y, \phi), \end{aligned} \quad (1.11)$$

where the notation

$$\mu^2 = \frac{m_\pi^2}{m_K^2}, \quad \nu^2 = \frac{m_e^2}{m_K^2}$$

is introduced and $F(x, y, \phi)$ is given by, neglecting the electron mass and terms concerned with small g_{E1} ,

$$\begin{aligned} & F(x, y, \phi) \\ &= \frac{8}{3}|g_{IB}|^2 \left\{ \frac{-16\lambda^{1/2}(x, \mu^2, \mu^2)x\mu^2}{x^2(x+y-1)^2 - \lambda(1, x, y)\lambda(x, \mu^2, \mu^2)} \right. \\ & \quad \left. + \frac{4(x-2\mu^2)}{(x+y-1)\lambda^{1/2}(1, x, y)} \ln(L) \left[\frac{1}{2}(1+2\sin^2\phi) \right] \right\} \\ &+ \frac{8}{3}|g_{IB}|^2 \left\{ \frac{16x^2y\lambda^{1/2}(x, \mu^2, \mu^2)x\mu^2}{\lambda(1, x, y)[x^2(x+y-1)^2 - \lambda(1, x, y)\lambda(x, \mu^2, \mu^2)]} \right. \\ & \quad \left. - \frac{8x^2y}{(x+y-1)\lambda^{3/2}(1, x, y)} \ln(L) \left[\frac{1}{2}(1-2\sin^2\phi) \right] \right\} \\ &+ \frac{8}{3}\text{Re}(g_{M1}g_{IB}^*) \frac{1-x-y}{\lambda^{1/2}(1, x, y)} \\ & \quad \left\{ -2\frac{\mu^2(1-x-y)^2 + y\lambda(x, \mu^2, \mu^2)}{(x+y-1)\lambda^{1/2}(1, x, y)} \ln(L) + \lambda^{1/2}(x, \mu^2, \mu^2) \right\} [\sin\phi \cos\phi] \\ &+ \frac{1}{18}|g_{M1}|^2 \frac{1}{x^2} \lambda(1, x, y) \lambda^{3/2}(x, \mu^2, \mu^2) \left[\frac{1}{2}(1+2\cos^2\phi) \right] \\ &+ \frac{1}{3} \frac{|g_{CR}|^2}{(x-1)^2} \frac{y}{x} \lambda(1, x, y) \lambda^{1/2}(x, \mu^2, \mu^2). \end{aligned} \quad (1.12)$$

The dependence of each term on the angle ϕ is indicated in square brackets. Here, the abbreviations

$$\begin{aligned} L &= \frac{(x+y-1)x + \lambda^{1/2}(1, x, y)\lambda^{1/2}(x, \mu^2, \mu^2)}{(x+y-1)x - \lambda^{1/2}(1, x, y)\lambda^{1/2}(x, \mu^2, \mu^2)}, \\ \lambda(x, y, z) &= x^2 + y^2 + z^2 - 2(xy + yz + zx) \end{aligned}$$

are used. Their resultant total branching ratio is

$$\begin{aligned}
B(K_L \rightarrow \pi^+ \pi^- e^+ e^-) &= (1.3 \times 10^{-7})_{IB} + (1.8 \times 10^{-7})_{M1} \\
&\quad + (0.04 \times 10^{-7})_{CR} \\
&\approx 3 \times 10^{-7}.
\end{aligned} \tag{1.13}$$

In the formula of the decay rate, ϕ dependence of each term characterizes its property under CP transformation. From the expressions in Equations (1.7)–(1.10), it can be obtained that $\cos \phi$ doesn't change its sign and $\sin \phi$ changes sign under the sequence of transformation C ($\vec{p}_\pm \rightarrow \vec{p}_\mp, \vec{k}_\pm \rightarrow \vec{k}_\mp$) and P ($\vec{p}_\pm \rightarrow -\vec{p}_\pm, \vec{k}_\pm \rightarrow -\vec{k}_\pm$). As can be seen in Eq.(1.12), the interference term ($g_{M1}g_{IB}^*$) has the ϕ dependence of $\sin \phi \cos \phi$, and then it changes sign under CP transformation and so is the CP violating one. We can see the effect through the asymmetry such as

$$A = \frac{\int_0^{\pi/2} \left(\frac{d\Gamma}{d\phi} \right) d\phi - \int_{\pi/2}^{\pi} \left(\frac{d\Gamma}{d\phi} \right) d\phi}{\int_0^{\pi/2} \left(\frac{d\Gamma}{d\phi} \right) d\phi + \int_{\pi/2}^{\pi} \left(\frac{d\Gamma}{d\phi} \right) d\phi}.$$

This asymmetry, integrated over x and y , is calculated to be $|A| \approx 15\% \sin \Theta$,³ where

$$\Theta = \text{arg}(g_{M1}g_{IB}^*) = \Phi_{+-} + \delta_0 - \bar{\delta}_1,$$

and $\bar{\delta}_1$ denotes an average phase in the $\pi\pi$ p-wave $I = 1$ channel. Inserting $\Phi_{+-} = 43^\circ$, $\delta_0 = 40^\circ$, and $\bar{\delta}_1 \approx 10^\circ$ (assuming an average $\pi\pi$ mass of approximately 0.4 GeV), $|A|$ is estimated to be about 14%. This effect arises from the admixture of CP-even component in the K_L wave function. In this sense, it is an example of indirect CP violation.

In another paper [11], effects of direct CP violation are estimated but are found to be small. In summary, the decay $K_L \rightarrow \pi^+ \pi^- e^+ e^-$ is quite interesting for studying CP violation effect. The observable parameter is relatively large and well calculated. Although our sensitivity for the mode, described in Section 4.4 does not reach to the level to see CP asymmetry effect, it is important to study for the decay mode $K_L \rightarrow \pi^+ \pi^- e^+ e^-$ and to build up a foundation of new testing field for CP violation.

1.2 Experimental Status

The experimental status of the $K_L \rightarrow \pi^+ \pi^- e^+ e^-$ and its related decay modes are summarized in this section.

³Although $\cos \Theta$ instead of $\sin \Theta$ was used here in Ref.[10], it was corrected in the Erratum [10].

In the decay $K \rightarrow \pi^+\pi^-\gamma$, the branching ratio was measured separately for a direct emission component (DE) and for an internal bremsstrahlung component (IB) [9]. In this experiment, both K_L and K_S decays were collected simultaneously. The branching ratio of $K_S \rightarrow \pi^+\pi^-\gamma$ was measured:

$$\frac{B(K_S \rightarrow \pi^+\pi^-\gamma; E_\gamma^* > 20\text{MeV})}{B(K_S \rightarrow \pi^+\pi^-)} = (6.36 \pm 0.09 \pm 0.05) \times 10^{-3},$$

where E_γ^* is the energy of photon in the kaon rest frame. Since this mode is dominated by the internal bremsstrahlung process, the energy spectrum of photons from IB contribution could be obtained.

In the measurement of K_L decay, relative strength of two amplitudes was determined by analyzing the energy spectrum of γ . The energy spectrum was fitted to a linear combination of the K_S spectrum, which was assumed to be same as the K_L IB contribution, and a Monte Carlo prediction for the photon energy spectrum resulting from the direct emission (DE) K_L decay. The resultant branching ratios of IB and DE contribution were reported to be

$$\frac{Br(K_L \rightarrow \pi^+\pi^-\gamma; IB, E_\gamma^* > 20\text{MeV})}{Br(K_L \rightarrow \pi^+\pi^-)} = (6.90 \pm 0.21) \times 10^{-3},$$

and

$$\frac{Br(K_L \rightarrow \pi^+\pi^-\gamma; DE, E_\gamma^* > 20\text{MeV})}{Br(K_L \rightarrow \pi^+\pi^-)} = (15.0 \pm 0.6) \times 10^{-3},$$

respectively.

In the signal mode $K_L \rightarrow \pi^+\pi^-e^+e^-$, our group (KEK-E162) reported the result of the experimental search for this decay mode, which was based upon the data of Helium run and established the upper limit of

$$Br(K_L \rightarrow \pi^+\pi^-e^+e^-) < 4.6 \times 10^{-7} \text{ (90\% CL)}$$

on its branching ratio [12, 13], and a preliminary result of the present experiment was presented in Ref.[14].

On the other hand, recently a group at the Fermilab (KTeV) reported the measurement of its branching ratio

$$Br(K_L \rightarrow \pi^+\pi^-e^+e^-) = (3.2 \pm 0.6 \pm 0.4) \times 10^{-7},$$

which was based on a sample 46 candidate events with an expected background level of 9.4 events [15].

Chapter 2

Experimental Apparatus

An experiment for $K_L \rightarrow \pi^+\pi^-e^+e^-$ was performed using KEK 12-GeV/c Proton Synchrotron (KEK-PS). This experiment(KEK-E162) originally aimed to search for $K_L \rightarrow \pi^0e^+e^-$ and other rare decay modes with electromagnetic products (e^+, e^-, γ). To achieve high sensitivities for these decay modes, large amount of data had to be taken and thus the experiment had to be performed at very high counting rate. This required a well-defined beam line, a detector system which could be operated in an extremely high rate environment, and good background rejection in an early stage of data taking.

In this chapter, descriptions of the instruments in the E162 experiment are presented.

2.1 Beam Line

The K_L beam was produced by a proton beam striking a target. KEK-PS delivered a 12 GeV/c primary proton beam to the target with a typical intensity of 1×10^{12} during 2-second spill per 4-second cycle. Figure 2.1 shows the side view of the neutral beam line, called K0 line which was located in the East Counter Hall of KEK-PS.¹ Before the target the primary protons were bent upward ($+2^\circ$) by a steering magnet (BS1) and then downward (-4°) by BS2 to strike the target at an angle of 2° . The production angle was determined taking account of the K_L yield and the ratio of produced K_L to neutrons. The target was 60-mm-long copper cylinder with 10-mm-diameter. Secondary neutral beam had the divergence of ± 4 mrad horizontally and

¹In our experiment, a position was represented in the right-hand coordinate system, where X- and Y-axis almost corresponded to the horizontal and vertical direction, respectively, and Z-axis was almost the neutral beam direction. Its origin was set at the center of the target.

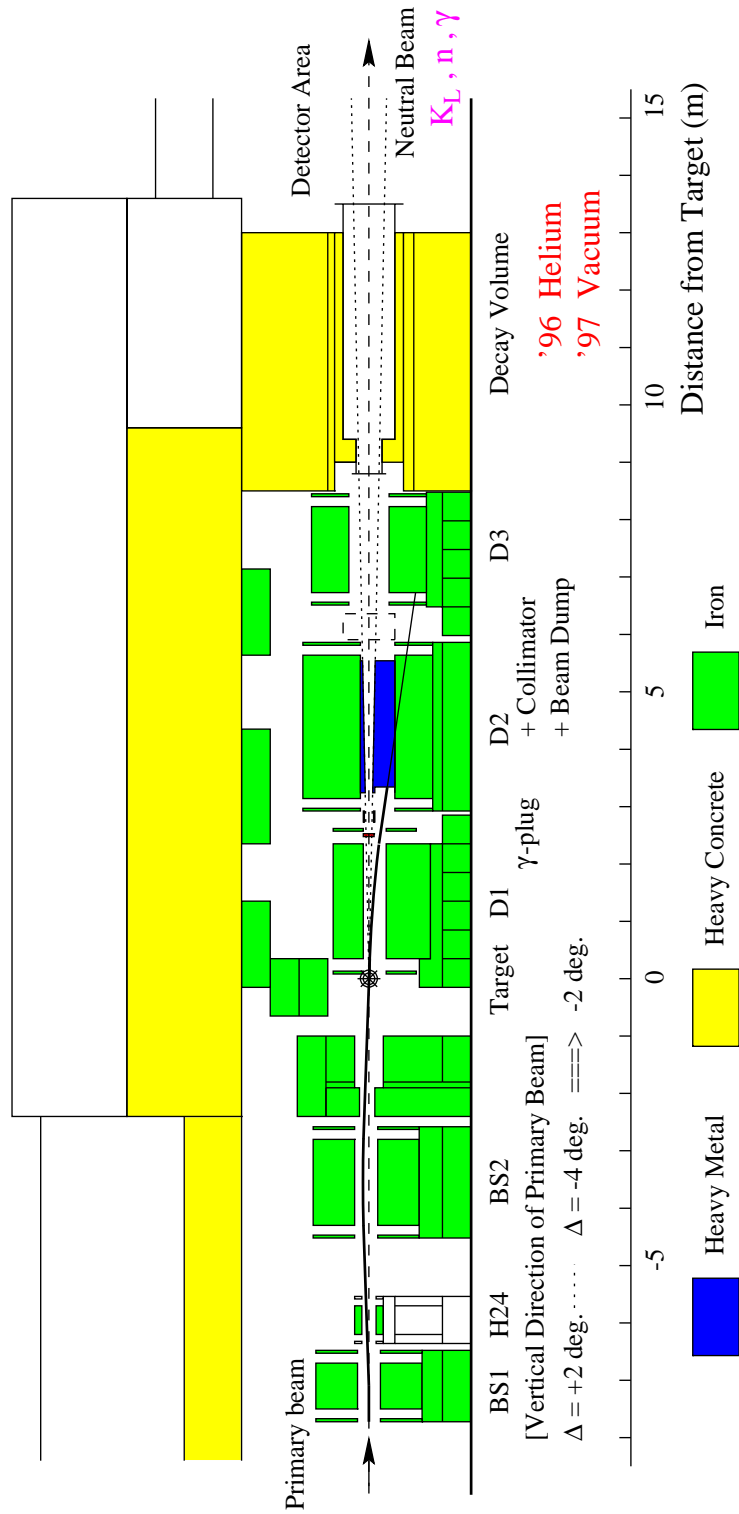


Figure 2.1: Side view of the neutral beam line : K0 line.

± 20 mrad vertically, defined by a series of collimators embedded in sweeping magnets. The rectangular beam with fairly large aspect ratio (1:5) was a compromise between large aperture (i.e. many kaons) and narrow width (i.e. small beam hole in detectors).

A 2-m-long magnet immediate downstream of the target (D1) bent down the primary beam to the beam dump and swept out charged particles produced at the target. Near the end of D1 magnet, at 2.5 m downstream of the target where the primary beam was separated from the neutral beam path, a 50-mm-thick lead block (γ -plug) was placed in the neutral beam, to remove photons produced at the target. Photons were converted into e^+e^- pairs and then were swept out by the magnetic field. The main collimator, as well as the primary beam dump, was embedded in the second sweeping magnet (D2). It was 2.5-m-long in the beam direction and made of the heavy metal (about 90 % tungsten, density of 17.13 g/cm³). The third 2-m-long sweeping magnet (D3) was placed at Z=6.5m which also had a brass collimator in it. These sweeping magnets were operated at about 2 Tesla.² The beam duct in D3 magnet pneumatically connected with the a decay volume, described below.

2.2 Decay Volume

Following the series of collimators and magnets, a 4-m-long decay volume started from Z=9.5m. The detector system was designed to measure K_L decays in the decay volume.

The neutral beam after D3 magnet still included not only neutral kaons but also neutrons and photons. They created background events by the interaction with materials in the beam region. Management of these background events at the trigger level as well as the offline analysis was one of the hurdles to overcome in the course of the experiment. Thus, it was preferable to reduce material density in the decay volume in order to keep unwanted interactions as small as possible.

Before it became ready to be evacuated, the decay volume was filled with helium gas at atmospheric pressure. To prevent detectors from being damaged by penetrating helium gas, its downstream window should have low gas permeability, and should be thin at the same time. We used a laminated film of Mylar ($12 \mu\text{m} \times 2$) and aluminum foils ($9 \mu\text{m} \times 2$) for the window in this time. It had been found in previous analysis [12, 13] that backgrounds from beam interactions with helium atoms were not negligible to achieve

²D2 magnet could not be operated due to trouble during the experiment. The influence on the counting rate was examined and found to be small.

further sensitivity for $K_L \rightarrow \pi^+\pi^-e^+e^-$. Since early 1997, it was evacuated down to 8×10^{-3} Torr by a oil rotary pump. The window in this time was a 180 μm -thick Mylar film reinforced with a cloth of Technora (0.09 g/cm²), high tenacity aramid fiber (Teijin Ltd.). The degree of vacuum was monitored by a pirani gauge throughout the beam cycles. Hereafter, we call the two periods of beam time as “Helium” and “Vacuum” run, respectively.

2.3 E162 Detector

The E162 detector region started at 13.5 m downstream of the target. Figure 2.2 shows the schematic view of the E162 detector system. The E162 detector system was originally designed to be optimum for the decay $K_L \rightarrow \pi^0 e^+ e^-$, whose final state consists of two electrons and two photons. The detectors were designed as follows. The system should measure energies and momenta of all components to reconstruct events. We selected the configuration of a spectrometer to determine momenta of charged particles, and a calorimeter placed at the most downstream position of detectors to measure energies and positions of electrons and photons. Several sets of trigger scintillators and gas Čerenkov counter were added to notify passages of fast charged particles and to identify electrons mainly during data acquisition. In the arrangement of components above, the design concept was to maximize acceptances for K_L decays: the detectors should have as large active areas as possible and should be put upstream within practical range. Thus, for example, the radiator part of gas Čerenkov counter was located inside an analyzing magnet gap, and there was only minimum vacant space between detectors. Another design philosophy was to achieve good performance in high counting rate environments, keeping high efficiencies and good resolutions. This required detectors to have narrow signal width, good time resolving power, and constant gain in any operating conditions. It was one of the most important points to determine structures of detectors and readout systems. In following subsections, each component of detectors is described in detail.

2.3.1 Spectrometer

The E162 spectrometer, whose function was to measure a trajectory, a sign of charge and momentum of charged particles, consisted of two sets of upstream drift chambers, an analyzing magnet, and two sets of downstream drift chambers.

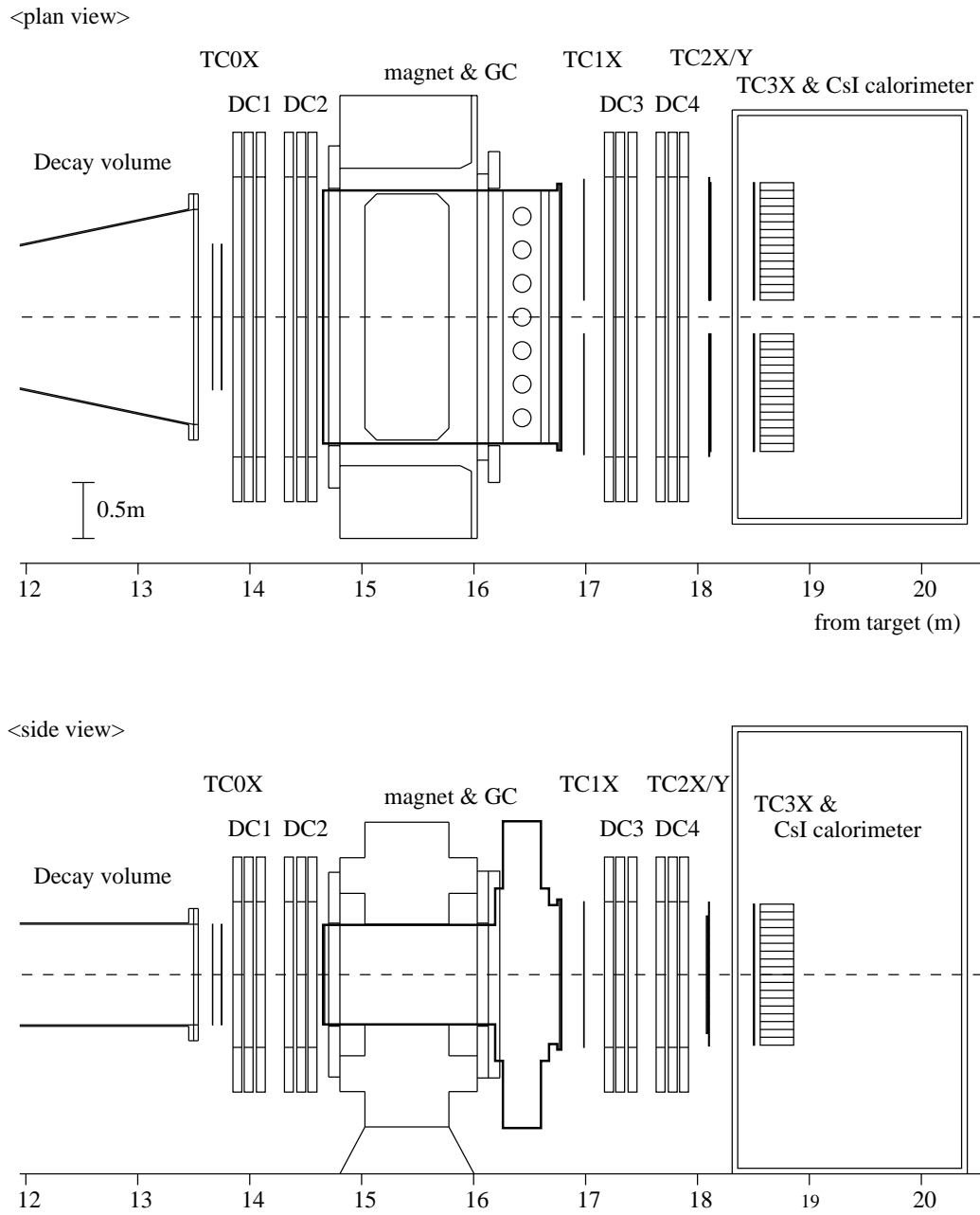


Figure 2.2: Schematic view of E162 detector system.

Analyzing magnet

The analyzing magnet was a dipole magnet located between upstream and downstream drift chambers. The pole piece was 0.75 m long in the beam direction, and its aperture was 2.2 m wide and 0.9 m high. The magnet provided a vertical field of 0.5 Tesla at the center. Its average field integral was 0.454 Tesla·m, corresponding to horizontal momentum kick of 136 MeV/c. The field strength was monitored by a NMR probe throughout the experiment.

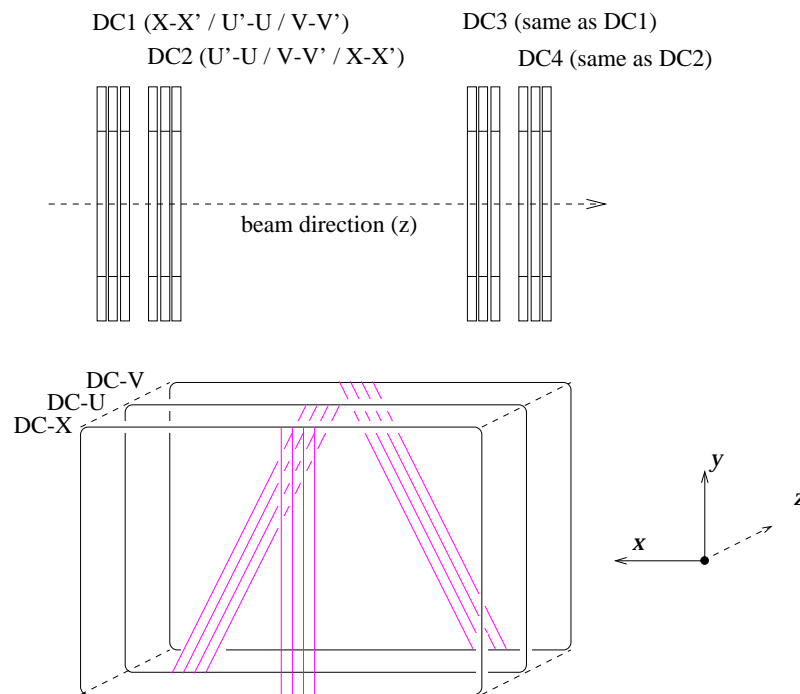
Drift Chamber

The structure of the drift chambers is shown in Figure 2.3. Each drift chamber set consisted of six readout planes, X-X', U-U', V-V', in which wires were strung vertically and obliquely by $\pm 30^\circ$, respectively. Note that two planes, for example, X- and X'-plane was staggered by a half-cell as shown in Fig.2.3(b) to resolve the left-right ambiguity of drift length. They had active area of 2.5 m wide by 1.3 m high, covering the neutral beam region. The chamber gas consisted of 50% Argon and 50% Ethane.³ The window used was 50- μm -thick Mylar aluminized on both surface. Each detecting cell consisted of a sense wire (30 μm diameter gold-plated tungsten with tension of 50 gf) surrounded by field wires (100 μm diameter gold-plated copper-beryllium alloy with tension of 100 gf). The half-cell size was 4 mm, which was a compromise between rate capability of chambers and total number of readout wires. Pitches of sense wires in a plane were measured by an optical sensor in construction process and their deviations from nominal values were kept within 50 μm . All chambers were operated with a voltage of -2150 V.

The signals from sense wire were amplified and discriminated immediately at the chamber. The amplifier, shown in Figure 2.4, was composed of three stage of common base amplifiers, pole-zero circuits to cancel out 1/t tail of a chamber signal, baseline restorers, and a pulse height limiter which prevented dead time by large (wide) pulses. For the upstream chambers and downstream X-view chambers, the output from the discriminator was then transported to the counting hut and received by a buffer module which supplied power and threshold voltage to the amplifiers and discriminators. To reduce influence by accidental hits, 1 GHz pipelined time-to-digital converter (PLTDC) [18] was used to record hit time information. For the downstream U/V-view chambers, the output from the discriminator was di-

³Although we had planned to use a gas mixture containing CF_4 which has fast drift velocity of electron [16, 17], for the rate capability, we employed a standard gas mixture of $\text{Ar}(50) - \text{C}_2\text{H}_6(50)$ for the simplicity of the calibration.

(a) The arrangement of Drift Chambers



(b) The Cell structure of Drift Chamber

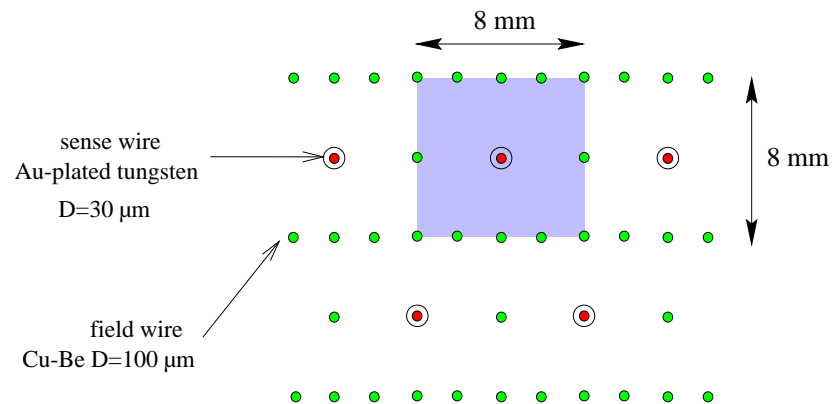


Figure 2.3: The structure of drift chamber, (a) schematic view of the arrangement and (b) the cell structure.

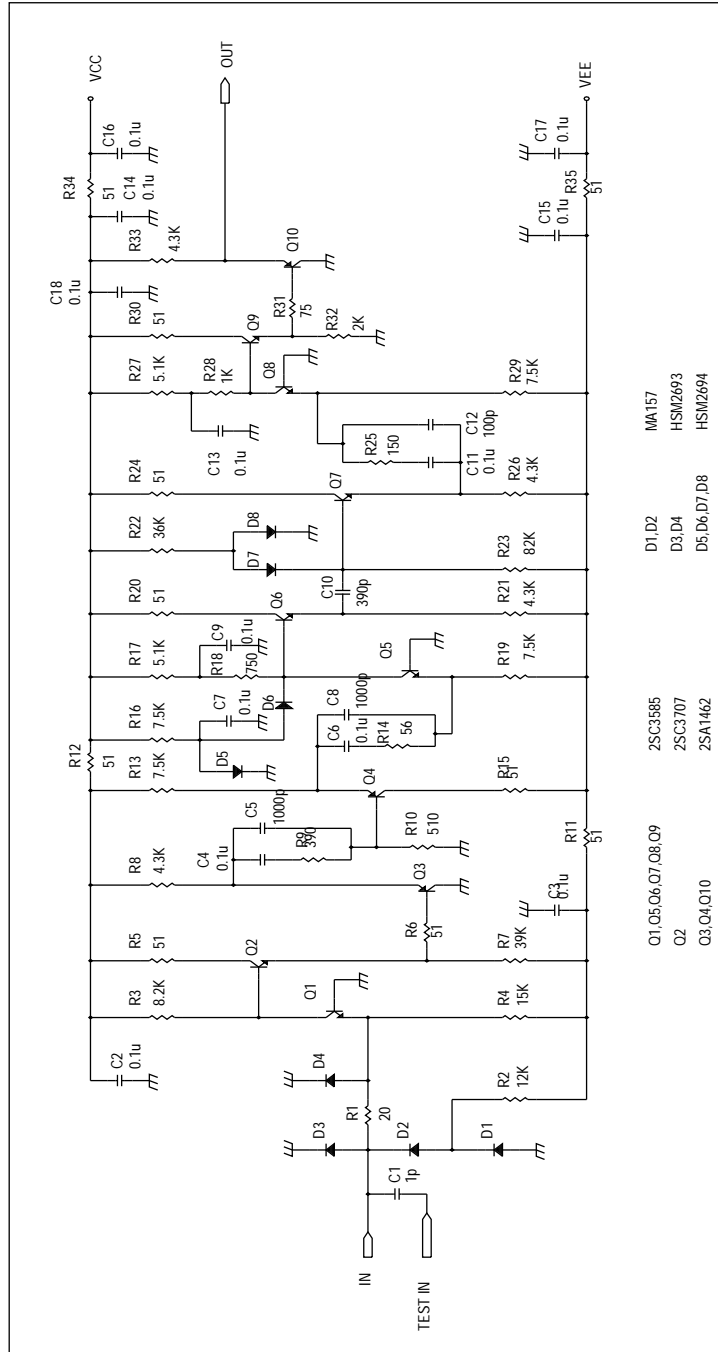


Figure 2.4: The pre-amplifier for drift chambers. It was composed of three stage of common base amplifiers (around Q1,Q5,Q8), three pole-zero circuits (two for $1/t$ tail of a chamber signal and one for the pole of first stage amplifier), baseline restorers, and a pulse height limiter equipped at the second common base amplifier.

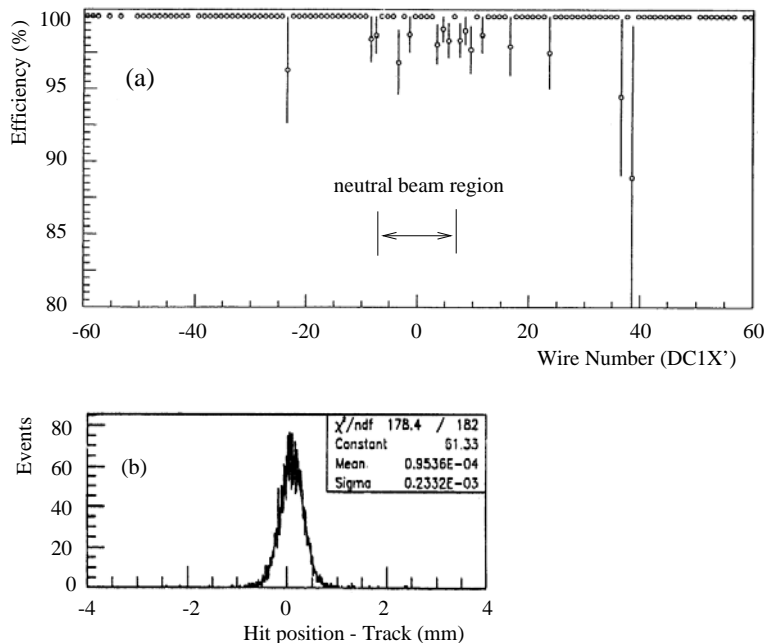


Figure 2.5: Examples of the drift chamber performance: (a) Efficiencies in DC1X' as a function of wire number, where the number 0 means a central wire. (b) position resolution of DC1X', defined as the deviation of the hit position of the wire to be examined from the expected position obtained with the other chamber information. Fitting to the Gaussian form, the resolution is found to be $\sim 220 \mu\text{m}$ (after the correction of the track interpolation error). The offset of the distribution indicates the shift in the position of this layer. This offset was used and corrected in the chamber alignments (see Section 3.1).

rectly received by a compound module of time-to-analog and analog-to-digital converter (TAC).

Efficiencies and position resolutions under typical beam conditions were examined by using straight tracks which were taken in the special run with the analyzing magnet off. Tracks were reconstructed without hit information of the object plane to be examined. Figure 2.5(a) and (b) shows examples (as to DC1X') of the efficiency and position resolution measurements of the drift chamber. A detection efficiency of each wire was evaluated by checking whether or not corresponding wire had an on-time hit, and was found to be more than 98% in all region. The position resolution was defined as the deviation of the hit position of the wire to be examined from the expected position by track fitting using other chambers, and the typical resolution was

found to be about $220 \mu\text{m}$.⁴

2.3.2 Electromagnetic Calorimeter

Two banks of calorimeters were placed at both sides of neutral beam line (apart 300 mm), each consisted of $15(\text{H}) \times 18(\text{V})$ undoped Cesium Iodide (CsI) crystal blocks. Their main function was to measure energies of electrons and photons, and the position of the photons and charged particles. Each CsI block was $70 \text{ mm} \times 70 \text{ mm}$ in cross section and 300 mm in length (about 16 radiation length). And a photomultiplier (PMT) was attached to the downstream end of each block to read a scintillation light output. The active area of each bank was 1.05 m wide by 1.26 m high. The calorimeter was placed in an air-conditioned housing box, where the temperature was kept constant (25°C) within $\pm 0.2^\circ\text{C}$ and the humidity was less than 30%.

Features of undoped Cesium Iodide scintillator are summarized below.

- (i) High Z materials ($Z = 53(\text{Cs}), 55(\text{I})$) and thus short radiation length ($X_0 = 1.85 \text{ cm}$)
- (ii) Two components (fast and slow) of scintillation light [19]
The fast component is characterized by short decay time constants ($\tau = 10$ and 36 ns) and relatively narrow emission spectrum at 305 nm. The slow component is emitted over a several μsec with wide spectrum above 400 nm.
- (iii) Relatively large light output
The light yield of the fast component is about 4% of standard NaI(Tl) scintillator, while that of the slow component differs from one crystal to another, which depend on impurities in crystals among other factors.
- (iv) Temperature dependence of light yield
The temperature coefficients for both fast and slow components are similar. They were measured to be $-1.5\%/^\circ\text{C}$.
- (v) Slightly hygroscopic
Although care should be taken not to expose crystals to humid atmosphere, it is unnecessary to seal them hermetically (like NaI).

⁴We also measured the position resolution from the distribution of “sum of distance”, which was the sum of two drift length of staggered two wires, for example, in DC1X and DC1X'. The resolution was found to be less than $160 \mu\text{m}$. The resolution, $220 \mu\text{m}$ in the text contained the effect of multiple scatterings in charged tracks, and was adopted as a representative value in track fitting.

Among the lists, the characteristic of fast scintillation response is especially suited for our purpose, to achieve high rate capability. Each block was wrapped with thin Teflon sheet and aluminized Mylar to improve light collection efficiency.

We employed a 2" head-on type photomultiplier (Hamamatsu R4275-02) to detect a scintillation light. It had a UV-glass window to transmit a fast component light from a CsI crystal, and had a 8-stage linear focus dynodes structure. Voltages between dynodes were supplied by a transistorized base (Hamamatsu E4270), designed by us with Hamamatsu Photonics Co., which stabilized voltage distribution even under a high counting rate environment. By using them, a photomultiplier gain was kept constant (within 2% decrease) up to an anode current of 400 μA , which was equivalent to the case when a 1 GeV electron struck a block at the rate of 2 MHz. A pulse linearity was also measured on the bench and found to be within 2% during the current range from 0.7 to 5.5 GeV in the equivalent electron energy. To avoid heat localization, each PMT base was temperature-controlled by air blow.

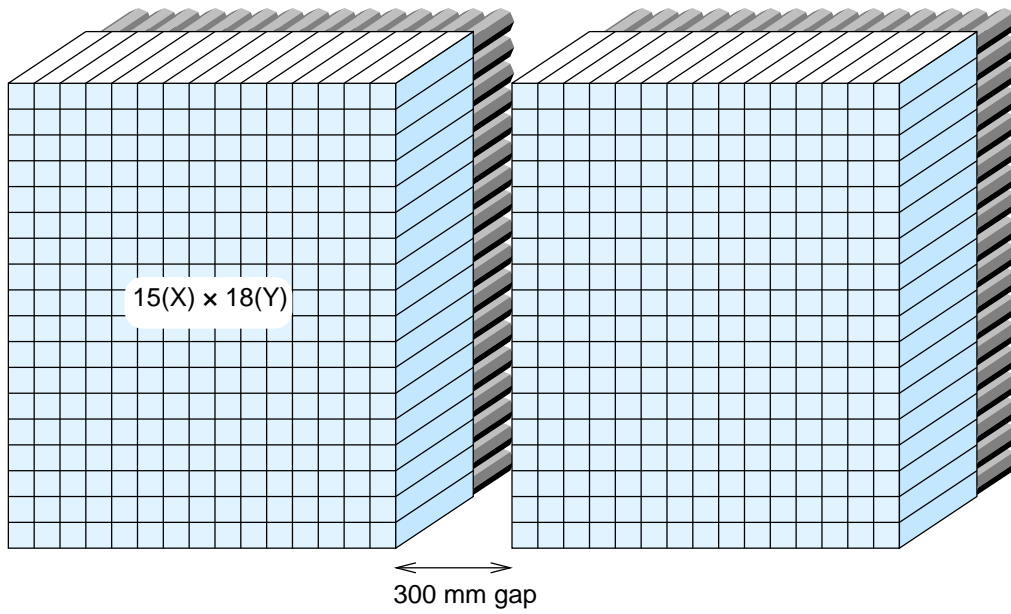
Several optical elements were equipped, as shown in Figure 2.6, between a CsI crystal and a photomultiplier window. A 30 mm-thick quartz light guide was glued onto a photomultiplier window by the epoxy resin (Epotec-305), whose transmittance at the wavelength of 300 nm was above 80%. Next, a bandpass optical filter (KENKO U-330) was glued to pass selectively the fast component. It cut off most of the slow component which could cause a baseline shift by pile-up effects. A silicone "cookie" was put between a crystal and an optical filter to make a photomultiplier detachable from a CsI block.

Each block had two quartz fiber inputs on its downstream end. Through one of them, a light from a Xe flash lamp was injected into a crystal to monitor the light transmittance of a crystal and/or the gain variation of a photomultiplier. The other was reserved for the light from a YAG laser, which, however, was not implemented in the experiment.

An analog signal from each PMT was transported into a buffer module in the electronics hut. It divided the signal into several ways: to an analog-to-digital converter (ADC [20]), to sum-amplifiers, to a time-to-digital converter (TDC [21]) via a discriminator, and to a processor used in the level 2 trigger. The sum-amplifier module produced an analog signal proportional to the energy deposit, summed over 18(15) CsI blocks in each column(row) in the stack. It had a baseline restorer to prevent an output signal from the baseline shift due to the pile-up. This output, called column(row)-sum, was discriminated and then used in the level 1 trigger.

The energy and position resolutions were found to be about 3% and 7 mm for one GeV electrons; the experimental procedure to determine these values

(a) Schematic view of the pure CsI array



(b) A module of the CsI calorimeter

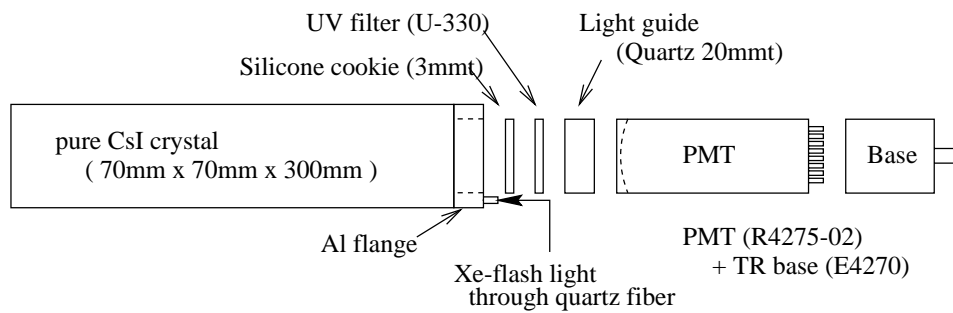


Figure 2.6: Schematic drawing of the calorimeter.

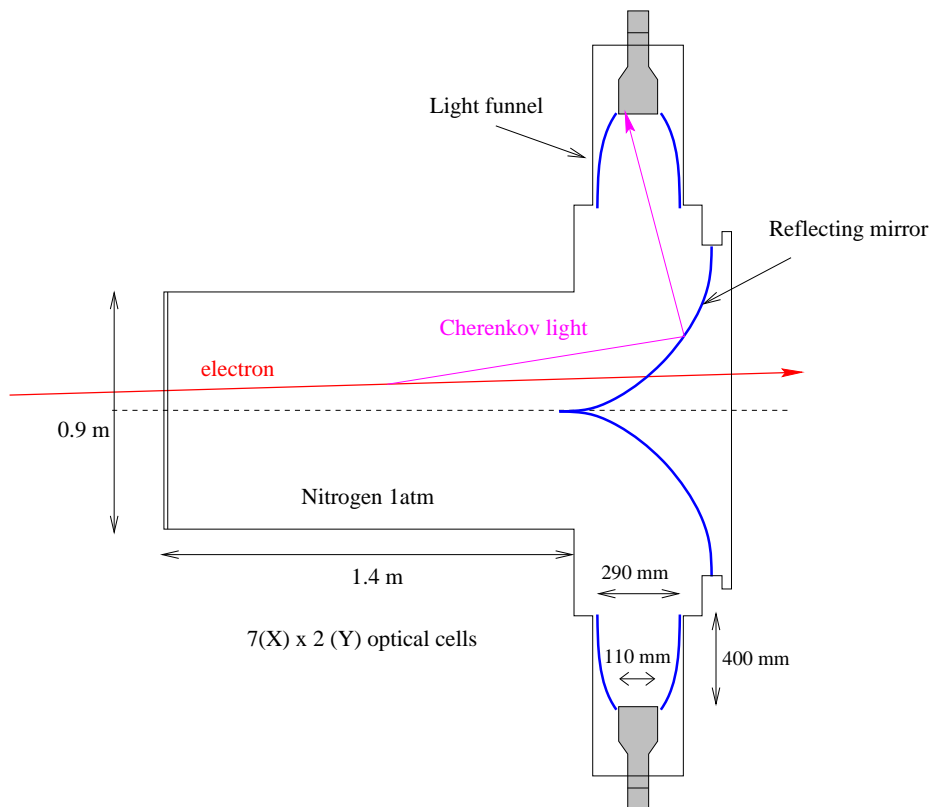


Figure 2.7: The side view of GC sliced at $X=0$. The arrangement of mirrors, light funnels and PMTs are shown in the figure.

will be described in next chapter.

2.3.3 Gas Čerenkov Counter

A 1.4m-long threshold gas Čerenkov counter (GC) was used to identify electrons. It was placed inside the gap of the analyzing magnet and filled with pure nitrogen at atmospheric pressure. It had 7 (horizontal) \times 2 (vertical) optical cells, each consisted of a reflecting mirror, a light collecting funnel and a photomultiplier. Figure 2.7 shows the side view of GC sliced at $X=0$.

Since the emission spectrum of Čerenkov light obeys $1/\lambda^2$ distribution, where λ indicates its wavelength, we made efforts to detect ultra-violet lights (down to 160 nm), to achieve good efficiency for electrons.

A reflecting mirror was made of 2 mm-thick acrylic substrate, coated with aluminum (Al) and magnesium fluoride (MgF_2) by vacuum evaporation. It had a parabolic shape to focus Čerenkov lights onto the PMT cathode. It was

produced as follows. An acrylic sheet was heat-formed in an oven by pressing a substrate to a convex model made of wood. Then it was trimmed by a laser cutting machine into an appropriate size (300 mm×800 mm). Supporting ribs were glued onto its backside. After that, its front surface was coated with 1000Å Al and 400Å MgF₂ in a vacuum chamber (1.5×10^{-6} Torr). Reflectivity of the mirror was monitored by a small sample which was coated together, and was found to be 80% or greater in the wavelength region between 160 nm to 200 nm and more than 85% above 200 nm.

A light funnel was the Winston type light collector [22], equipped in front of a photomultiplier to increase the effective detecting area. It was press-formed from a 1.5 mm-thick aluminum plate. Its inside surface was coated with Al and MgF₂, same as above.

A 5" photomultiplier (Hamamatsu R1251) was used to detect Čerenkov light. It has a quartz window to detect ultra-violet lights down to the wavelength of 160 nm. A gain of each photomultiplier was monitored throughout the experiment. Actually, it was carried out by observing a pulse height corresponding to single photo-electron emission, provoked by a green LED light.

To study performance of the counter, we used the $K_L \rightarrow \pi e \nu$ (K_{e3}) data which was taken by a special trigger; hit information from the gas Čerenkov counter was not used in any form in the trigger. Efficiency for e^+/e^- and pion rejection factor are shown in Figure 2.8 as a function of the threshold for light output, in units of number of photoelectrons (p.e.) For the actual trigger, we set the threshold level at about 1.5 p.e., where the pion rejection of 1/50 was achieved with the electron efficiency of 99.7%.

2.3.4 Trigger Scintillation Counters

Trigger scintillation counters were the main components to provide trigger. There were four sets of trigger scintillation counters (see Figure 2.2), labeled TC0X, TC1X, TC2X/2Y and TC3X, where X(Y) represented a horizontally (vertically)-segmented hodoscope. One set (TC0X) was located just downstream of the decay volume. The other sets were located downstream of the analyzing magnet.

The crucial function of TC0X was to enhance the existence of charged particles coming from the decay volume, and to reduced background events which were originated from photon conversions in the detector materials, both at the trigger stage and in the offline analysis. TC0X consisted of two layers of plastic scintillation counters, labeled TC0F and TC0R, which were placed 90 mm apart in the beam direction. These counter were located upstream of the analyzing magnet. Therefore they had an active area also in

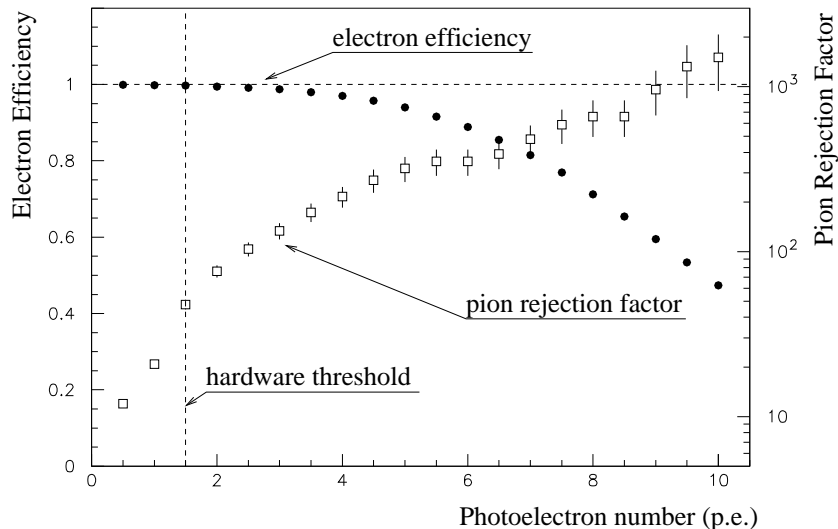


Figure 2.8: Electron efficiency and pion rejection factor of GC as a function of the threshold light output. The threshold is represented in photoelectron number of GC signal.

the neutral beam region to avoid the loss of acceptance. The dimensions of the individual counter segments were 900 mm in height and 1.5 mm in thickness. As for the width, there were two kinds, 25 mm and 50 mm. The narrow counters were placed inside/near the beam region to reduce counting rate of each counter. Each scintillator was wrapped with 25 μm -thick aluminized Mylar to avoid a crosstalk of scintillation lights. The arrangement of the scintillators is schematically shown in Figure 2.9. The scintillation light output of each component was read by two 1-1/8" photomultipliers (Hamamatsu R1398) which were attached to top and bottom ends of a scintillator. The photomultiplier equipped with a transistorized base [23] and operated with a subdued gain ($\sim 4 \times 10^5$) to keep good gain stability in high counting rate environments. In addition, we used an AC-coupled preamplifier (with ~ 30 db gain) to supplement the photomultiplier gain, and a base-line restorer to compensate base-line shifts at high counting rate. The typical counting rate of a photomultiplier in the beam region was about 2 MHz, while the gain stability of a photomultiplier tube with its base was checked up to 5 MHz on a bench test [24]. Figure 2.10 schematically shows the output signal flow of TC0. The output signal from the photomultiplier was processed by a discriminator via the preamplifier and base-line restorer. Then, coincidence was required between one channel in TC0F and one of the two adjacent channels in TC0R right behind it to enhance a charged particle going through.

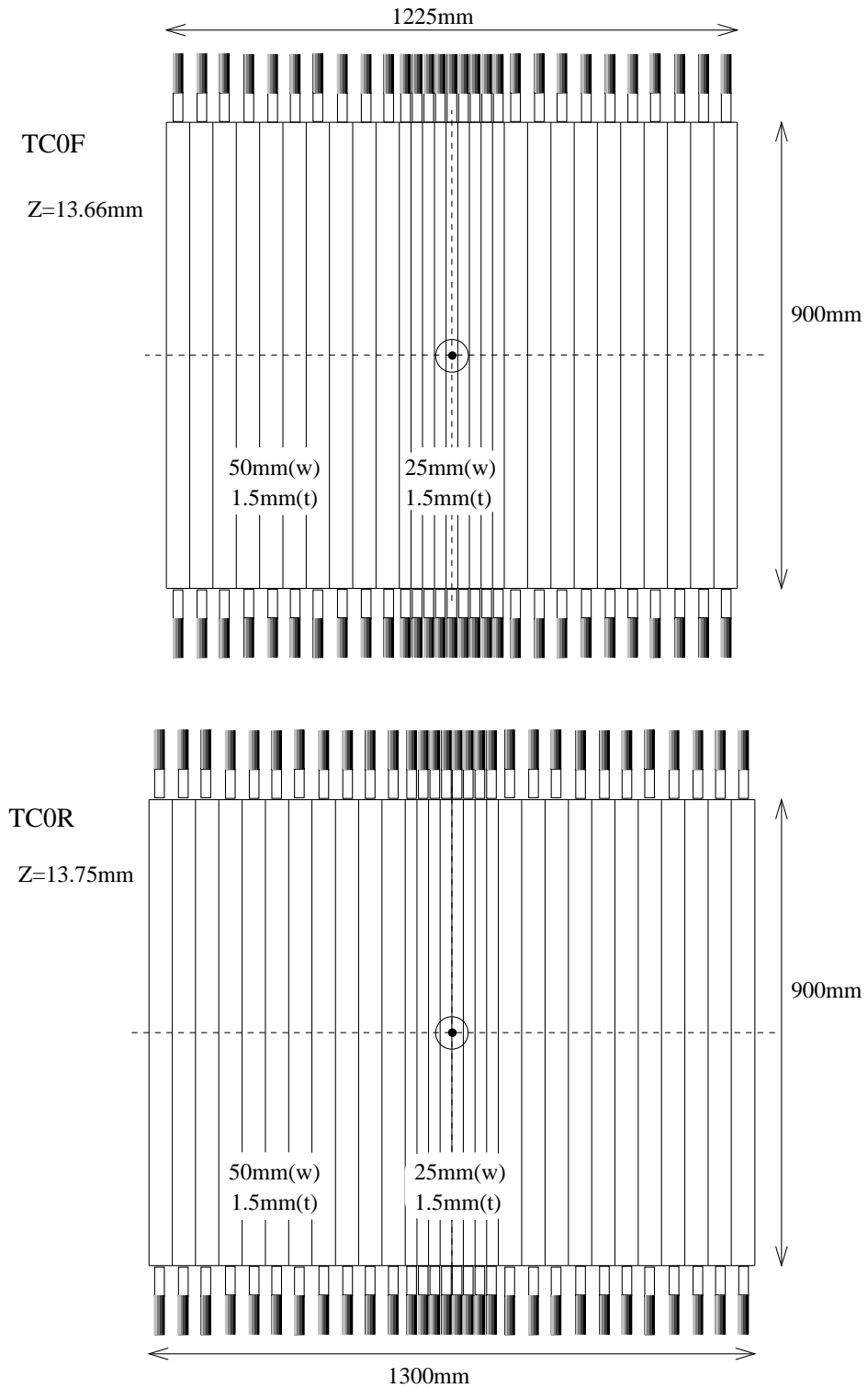


Figure 2.9: Schematic view of the TC0X hodoscope. The counter consisted of two hodoscope planes, TC0F and TCOR, and was active even in the beam region.

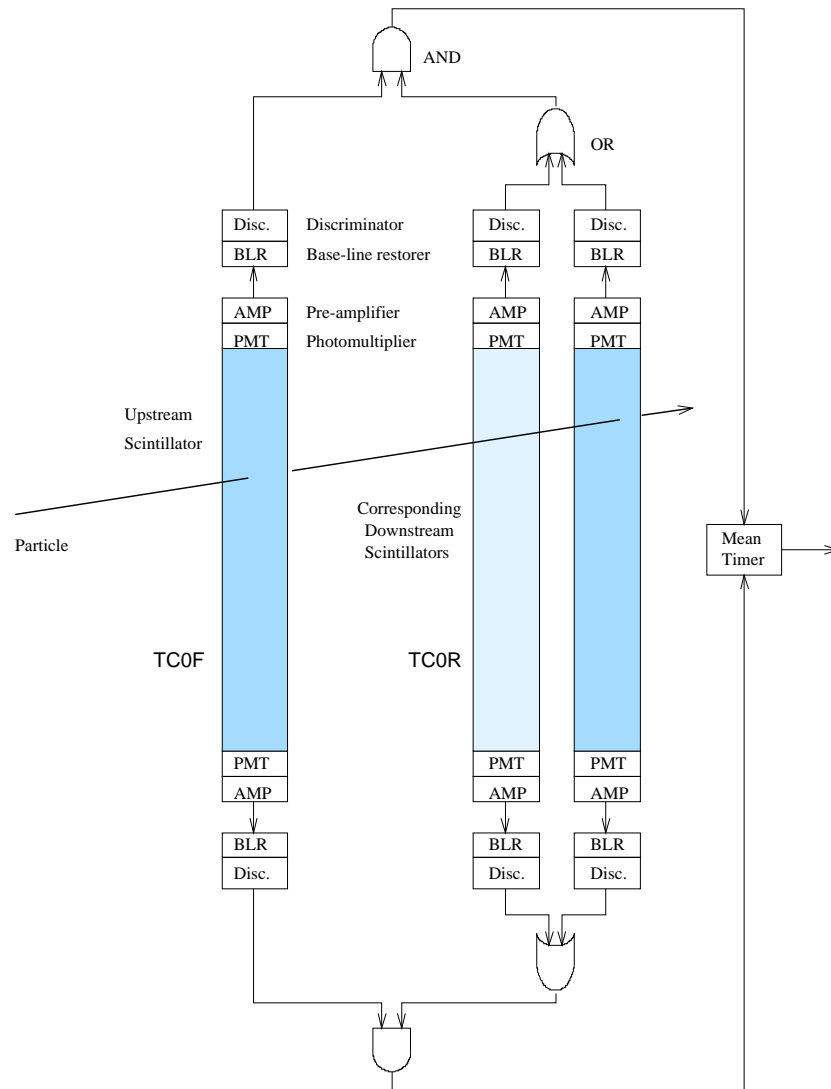


Figure 2.10: Schematic diagram of TC0 output signal flow.

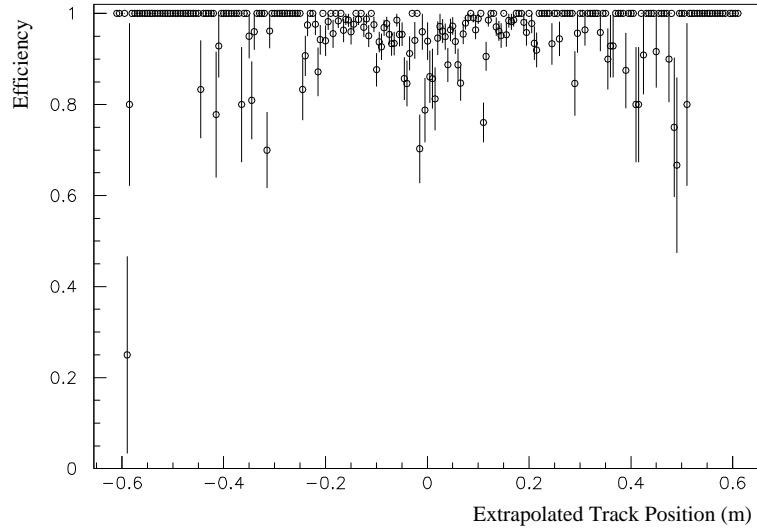


Figure 2.11: The detection efficiencies of TC0X for charged track as a function of the extrapolated track position at TC0X plane.

Finally, a mean-timer module was used to produce a coincidence signal between the top and bottom ends of the scintillator to reduce the timing jitter due to the variation of hit positions. The efficiency for charged tracks was measured in the typical beam intensity, by checking mean-timer output corresponding to extrapolated position of a track which was reconstructed by the drift chambers. Figure 2.11 shows the efficiencies as a function of the extrapolated track position at TC0X plane. It was found that the over-all efficiency of TC0 was 96% for a track, and that the inefficiency was mainly due to geometrical reason: gaps between adjacent scintillators.

The other sets of trigger scintillation counters were located downstream of the analyzing magnet. Their dimensions were schematically shown in Fig.2.12–2.14. Each plane had a 300-mm-wide gap at the center for the neutral beam to pass through. TC1X and TC2X/Y were located in front of and behind drift chamber sets, respectively. TC1X(2X) consisted of 13(16) counters in each arm, with the thickness of 2.6(10) mm and the width of 45(35) mm for most inside two counters and 90(70) mm for others. TC2Y, segmented vertically, had 18 counters in each arm with the thickness of 10 mm and the width of 70 mm. TC3X was placed immediate upstream of CsI calorimeter in its housing box. It was composed of 15 counters in each arm, with the thickness of 10 mm and the width of 70 mm. Each counter was read by a 2" photomultiplier (Hamamatsu R329-02) equipped with a transistorized base (E4524) similar to the one used for the calorime-

TC1X

Z = 16.90 m

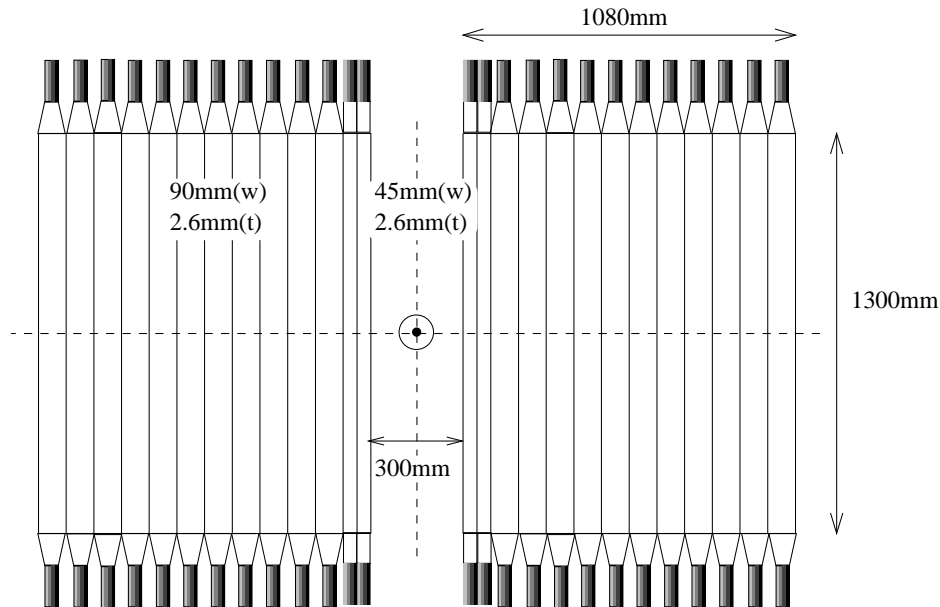


Figure 2.12: The trigger counter plane TC1X.

ter. Counters in horizontally-segmented hodoscopes were viewed from both top and bottom ends of scintillators, and those in vertically-segmented one (TC2Y) were viewed from one side, opposite to the beam region. Signals were discriminated in the counting room and were used to make up trigger information.

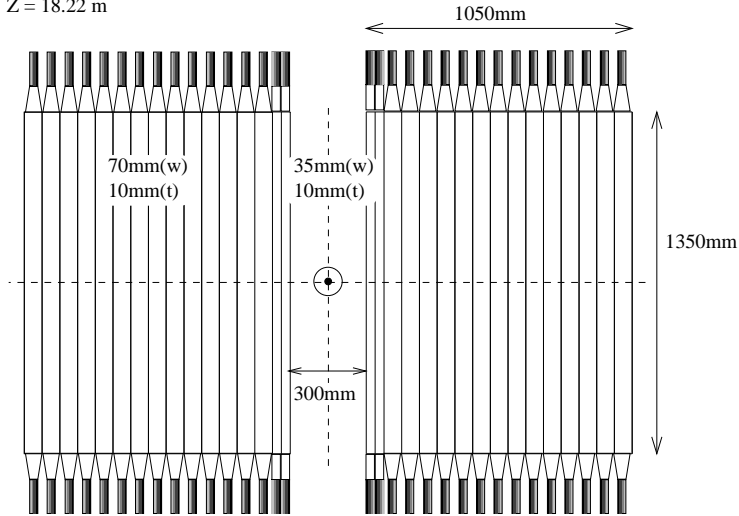
2.4 Trigger System

The triggers in our experiment had 4 types of logic according to target physics modes (Trig.0, 1, 2, 3). In addition, it had one type to study beam-associated backgrounds (Trig.4), and three types for calibrations of detectors and electronics (Trig.5, 6, 7), listed in Table 2.1. The trigger system was designed to take data for the physics mode (Trig.0–3) and some calibration mode (Trig.4 and 7) simultaneously. Each logic for physics modes was composed of two levels. The level 1 trigger was produced by fast NIM logics within 100 nsec after the particle passage through the detectors. The level 2 trigger was made by a set of hardware processors within 10 μ sec.

The information used at the level 1 was the number of counter hits and

TC2X

Z = 18.22 m



TC2Y

Z = 18.21 m

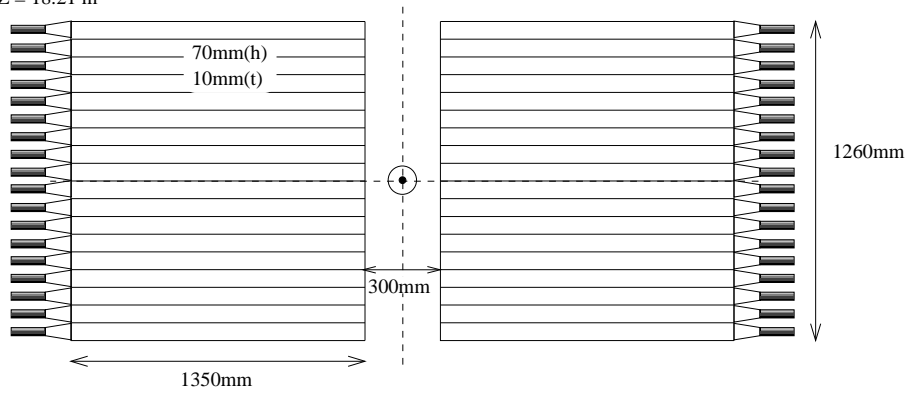


Figure 2.13: The trigger counter plane TC2X and 2Y.

Table 2.1: Physics and calibration trigger modes.

Trigger mode		Target
Physics	Trig.0	$K_L \rightarrow e^+e^-\gamma$ $K_L \rightarrow \pi^0e^+e^-$, $K_L \rightarrow \pi^0\gamma e^+e^-$ ^a
	Trig.1	$K_L \rightarrow \pi^+\pi^-\pi^0$
	Trig.2	$K_L \rightarrow e^+e^-e^+e^-$
	Trig.3	$K_L \rightarrow \pi^+\pi^-e^+e^-$
Calibration	Trig.4	Random Trigger ^b
	Trig.5	CsI Energy Calibration (K_{e3}) GC Efficiency (K_{e3}) TC0/DC Efficiency (magnet off)
	Trig.6	Pedestal Run GC LED Run
	Trig.7	Xe Flash Lamp

^a We reported a 90% C.L. upper limit of the branching ratio on this mode [25].

^b created by the coincidence of unrelated two counters.

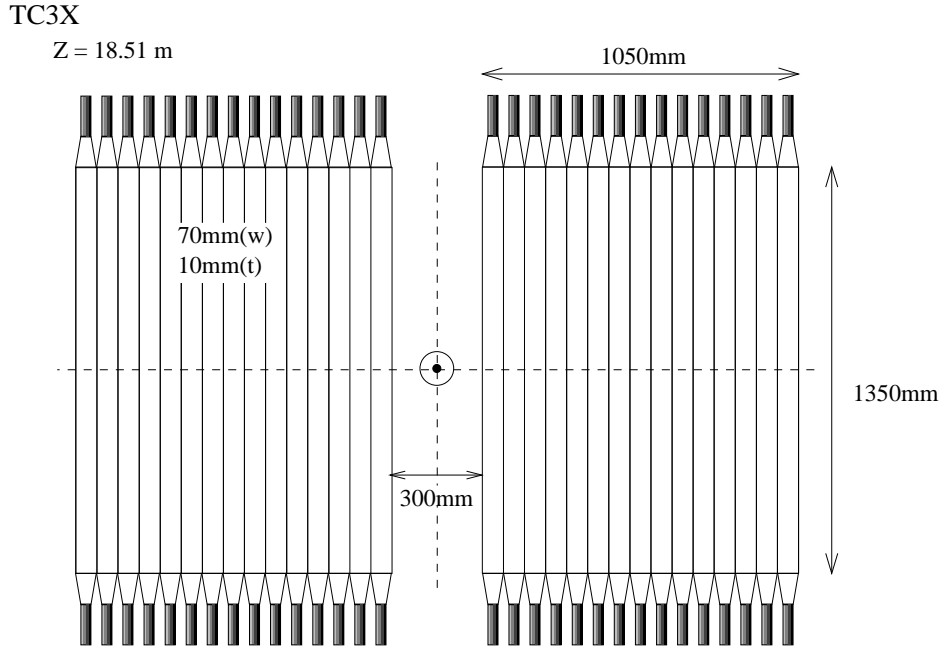


Figure 2.14: The trigger counter plane TC3X. It was placed in the housing box of the calorimeter.

their coincidences. The logical requirements imposed on the counter hits at the level 1 are listed in Table 2.2. A logic “TC23” in the table denotes the coincidence of one counter in TC2X with immediate downstream counters (three or four counters) in TC3X. A logic “TC0” represents the coincidence of one counter in TC0F and one of the two counters right behind it in TC0R. A logic “CSIX(Y)” is a discriminated signal of column(row)-sum, described in Section 2.3.2, with the threshold voltage equivalent to 300 MeV. Once one of the level 1 logics was satisfied, gate signals were provided into ADCs, TDCs and processors in the level 2 logic.

The level 2 trigger had two objects. One was to count the number of track candidates; this task was done by a coarse tracking processor (CTP), by looking for the correlated hits in downstream trigger hodoscopes. The other was to search for clusters on the calorimeter; it was done by a cluster finding processor (CFP), using the hit positions in the CsI blocks.

The CTP was composed of a sequencer part and a lookup memory in which possible track patterns had been pre-recorded. There were four CTPs, two for left arm and two for right arm. Modules in one arm had different patterns for positive and negative charged tracks. A track to be searched was defined as specific combinations of TC1X, TC2X and TC3X. The CTP

Table 2.2: Level 1 trigger hit requirements.

Source	Trigger mode			
	Trig.0	Trig.1	Trig.2	Trig.3
N(TC23) ¹	≥ 2	≥ 2	≥ 3	≥ 3
N(TC0X)	≥ 2	≥ 2	$\geq 2^b$	≥ 3
N(TC1X)	≥ 1	≥ 1	$\geq 2^a$	$\geq 2^a$
N(TC2Y)	≥ 1	≥ 1	$\geq 2^a$	$\geq 2^a$
N(GC)	≥ 2	—	≥ 3	≥ 2
N(CSIX) ²	$\geq 3^a$	$\geq 2^a$	$\geq 3^a$	$\geq 2^a$
N(CSIY) ³	$\geq 3^a$	$\geq 2^a$	$\geq 3^a$	$\geq 2^a$

¹ Number of the coincidence signal between TC2X and TC3X.

See the text for detail.

² Number of the column-sum hits in the calorimeter.

³ Number of the row-sum hits in the calorimeter.

^a At least 1 in both arm.

^b ≥ 3 in the Helium run.

also searched electron candidates among the found tracks, by matching the hit pattern in GC and CSIX. Each module produced an encoded output, containing the number of charged tracks and the number of electrons. The information was sent to the decision modules, which will be described below.

The CFP consisted of 16 modules (8 for each arm) and a sequence controller. Each module received analog signals of CsI blocks from two adjacent columns. It then discriminated them with a threshold equivalent to 250 MeV, which was determined to be higher than the energy deposit of a minimum ionizing particle. The information of hits was latched and converted to a bit pattern. Then the modules tried to find clusters by matching the actual hit pattern with prescribed patterns. The pattern recognition was carried out sequentially from the bottom row to the top row under the instruction of the controller. Using the information of hits in TC3X and TC2Y, the modules also examined whether or not the found cluster was associated with a charged particle. Since the threshold was set higher than the energy deposit by minimum ionizing particles, the cluster associated with a charged particle was considered as an electron cluster. After the finding sequence, the number of clusters and that of electron clusters in each arm were sent to corresponding decision modules.

Two decision modules with XILINX XC3190 logic cell arrays (XLP/XRP)

Table 2.3: Level 2 trigger logics

Logic	Trigger mode			
	Trig.0	Trig.1	Trig.2	Trig.3
N(tracks) ¹ by CTP	$(\geq 2)^a$	$\geq 2^b$	$(\geq 3)^a$	≥ 3
N(clusters) ² by CFP	≥ 3	$\geq 2^b$	≥ 3	$\geq 2^b$
N(e-TRK) ³ by CTP and CFP	≥ 2	—	≥ 3	$\geq 2^b$

¹ Number of charged track candidates.

² Number of clusters in the calorimeter.

³ Number of electron candidates.

^a Effective constraint through the requirement of N(e-TRK).

^b At least 1 in both arm.

Table 2.4: Trigger rates (Vacuum Run).

Stage	Trigger rate (counts/spill)						Total (Logical OR)
	Trig.0	Trig.1	Trig.2	Trig.3	Trig.4	Trig.7	
Level 1	1.7K	30K	290	490	51	40	1.9K
Prescale	1/1	1/80	1/1	1/1	1/3	—	
Level 2	660	220	80	170	17	40	850

received the information from the CTP and the CFP system. Their task was to distinguish electron candidates (e-TRK) more exactly by combining track and cluster information.

Finally, a master decision module (XDM), which was the same module as XLP/XRP but loaded different logic program, produced “accept” signals for various trigger types. Trigger logics for four physics modes were summarized in Table 2.3.

If no accept signal was asserted within 10 μ sec from the gate signal by the level 1 trigger, conversion processes in ADCs and TDCs were stopped and the event was discarded.

The trigger rates under a typical running condition were summarized in Table 2.4. The dead time was from 10% to 20% typically.

2.5 Data Acquisition System

If an event was accepted by one or more trigger modes, the data acquisition (DAQ) system read out and then registered the information of detectors. Table 2.5 lists contents of the registered data, which consist of digitized data from ADCs and TDCs, latched hit patterns of hodoscope channels, and logics of them. The composition of DAQ system is shown schematically in Figure.2.15. A sequence of data processing is described below.⁵

At first, when an event was accepted by the level 1 trigger, front-end electronics modules began processing the information from various detectors. The most of the front-end modules were controlled on the basis of TKO standard which had been developed at KEK[27]. Analog signals from CsI blocks were digitized by charge-sensitive ADCs with 110-nsec-wide gate. Discriminated signals from drift chambers were processed by 1GHz pipelined TDCs. Discriminated signals from hodoscopes were latched with 60-nsec-wide gate by strobed coincidence (SC) modules, and then digitized by TDCs.

Each front-end module in TKO boxes performed three steps of data processing: sample-and-hold, digitization, and readout. If these processes were executed in series, modules had been busy for a long time. To avoid this type of dead time in data processing, we adopted a pipeline operation between these stages. Once a gate signal was received, a module started the sample-and-hold and the digitization process. The digitized data were transferred to a register where they were held until the readout cycle. After the transfer, the sample-and-hold part of the module became free to process the next event even before the readout process for the previous data. This parallel processing reduced the dead time substantially.

If an accept signal by the level 2 trigger was asserted, a controller (SCH) in each TKO crate scanned modules sequentially and examined whether or not data existed in the registers. If existed, digitized data were read out by SCH and transferred to a corresponding memory module (MP) in a VME crate through a twisted flat cable. Data had been stored in the MPs during one beam extraction cycle.

After a beam extraction period, all the data in the MPs were transferred into memories on CPU boards via the VME bus.⁶ The role of these CPUs was to build up the event data. The event-building task was shared by three CPUs (CPU-A/B/C) to speed up processing at the first stage. Then the data built by each CPU were sent to another CPU (CPU-M) via dual port

⁵Detailed description can be found in Ref.[26].

⁶One CPU was operated on OS-9 68020 system (CPU-B in the figure) that is a real-time operating system for Motorola 68000 family. Other CPUs including master event-builder (CPU-M) had SPARC architecture and worked on SunOS.

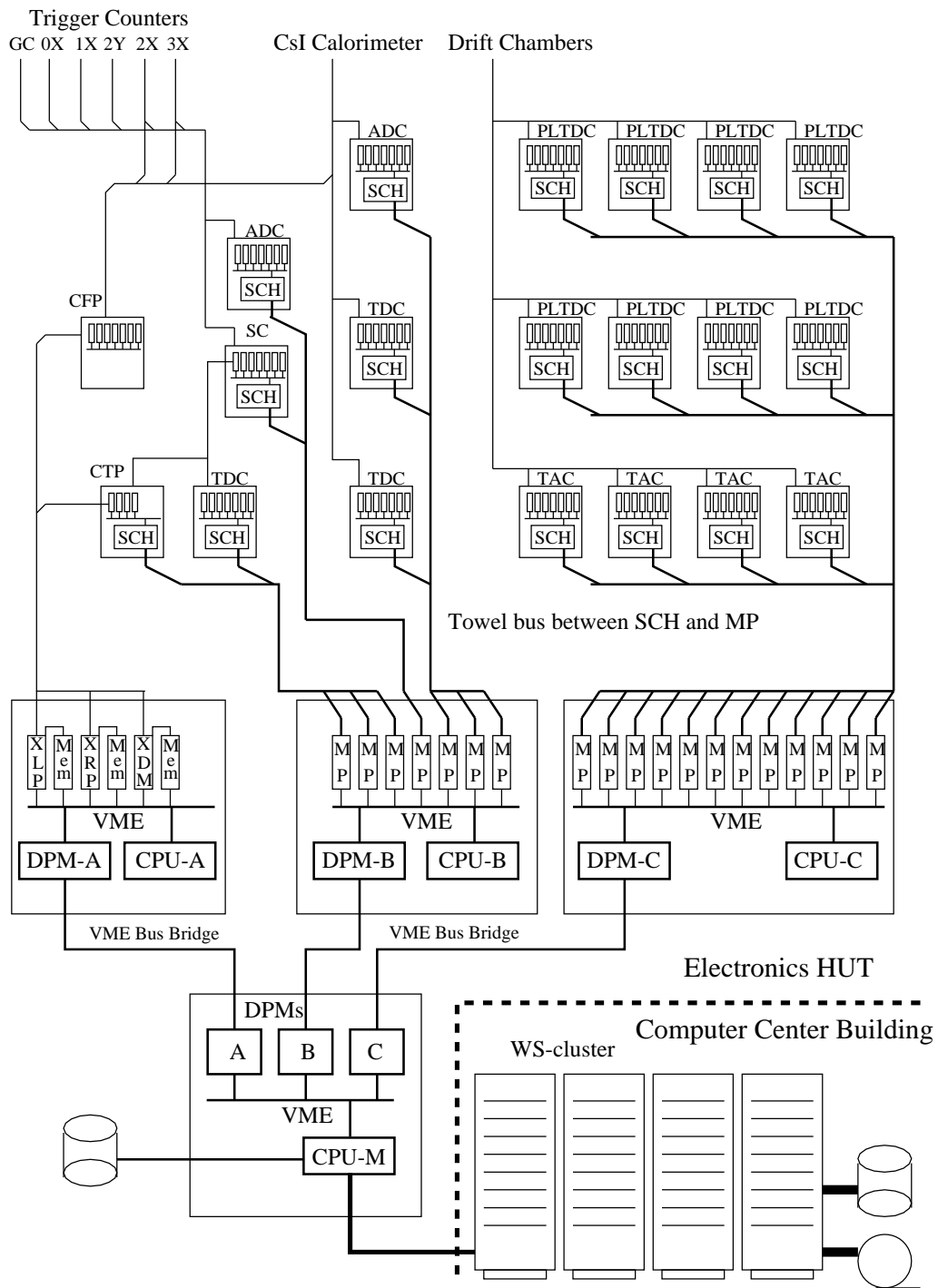


Figure 2.15: The DAQ system in E162 experiment.

memories, and were integrated by a master event-builder.

After the event-building procedure was finished, integrated data were transferred to a local disk for quick analysis, to a local DAT via a SCSI bus, and also to the workstation cluster via FDDI LAN for main analysis.

Table 2.5: Contents of the data.

Source		Sort
Detectors	TC0X	SC ^a , PLTDC ^b
	TC1X	SC, TDC
	TC2X/Y	SC, TDC, ADC ^c
	TC3	SC, TDC, ADC ^c
	GC	SC, TDC, ADC
	calorimeter	TDC, ADC
	drift chamber	TAC (DC3U/V,DC4U/V) PLTDC(others)
Logic	TC23	SC, TDC
	CSIX/Y	SC, TDC
Trigger info.	CTP	track info. (encoded)
	CFP	block hit pattern (latched) cluster info. (encoded)
Scaler	beam condition	spill count, clock target monitor (TM) intensity monitor (SEC)
	live-time monitor	w/ and w/o BUSY ^d

^a The latched information by the strobed coincidence module.

^b Of individual PMTs (TC0F:U/D,TC0R:U/D) and of logic "TC0X".

^c Of individual PMTs (TC2X:U/D,TC3X:U/D).

^d BUSY signal was asserted by trigger control module.

Chapter 3

Event Reconstruction

The data analysis is classified into two phases. The first phase is called “event reconstruction”, and is presented in this chapter. This is an analysis step to obtain basic physical quantities from raw data. The second phase is to identify the signal mode $K_L \rightarrow \pi^+\pi^-e^+e^-$ from the events reconstructed in the previous phase. This phase is a heart of physics analysis, and will be described in the next chapter in detail.

The event reconstruction proceeds as follows. First, hit positions on the drift chambers are reconstructed and trajectories of charged tracks, their charge signs and their momenta are determined. Then obtained are hit positions and deposited energies on the calorimeter. With these quantities, particle species of the charged tracks are identified and photon candidates are singled out. Finally, the decay vertex point is calculated.

3.1 Track Reconstruction

In this experiment, a track registered by a charged particle was measured with 4 sets of drift chambers. The track reconstruction thus started with determination of hit positions in the chambers. Next, charged track candidates are found from a set of hits on the drift chambers. They are fitted as the track and their 3-dimensional track parameters are evaluated. In the following, these procedure will be explained in detail starting with the drift chamber calibration.

3.1.1 Calibration of Drift Chambers

In order to calculate a hit position from hit time information (registered as TDC channels), we need two basic quantities; one is the TDC channel ($T0$)

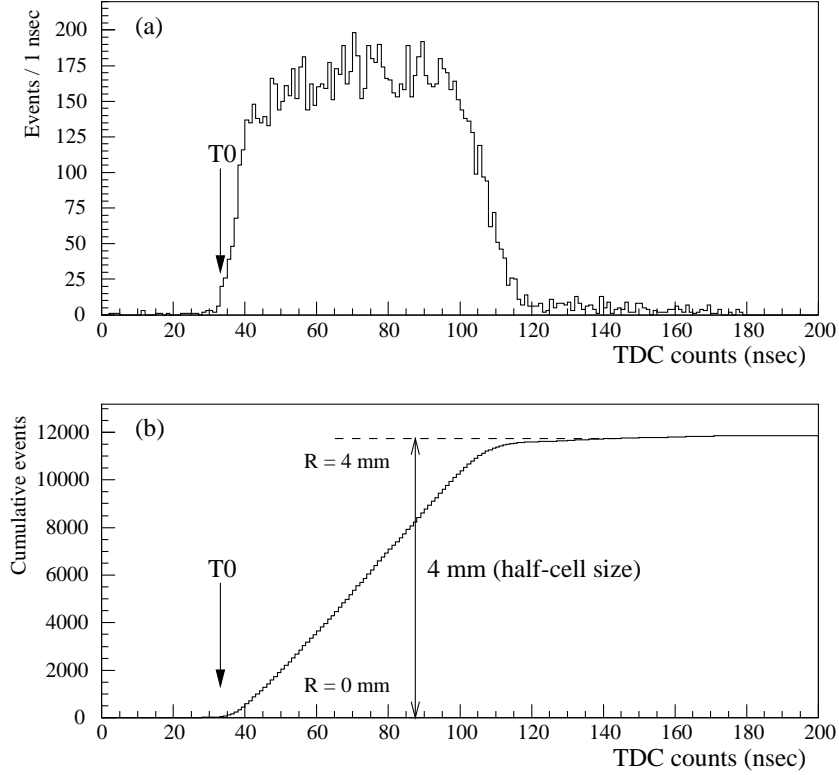


Figure 3.1: (a) A typical drift chamber TDC distribution and (b) its cumulative distribution.

that corresponds to a zero drift time, and the other is a precise relationship between drift time and drift length (R - t relation). Of course, precise position information of chambers themselves in the detector system is also in need.

Figure 3.1(a) shows an example of a TDC distribution. Roughly speaking, the left edge of the trapezoid distribution corresponds to T_0 . To be specific, it is defined by the intersecting point of a straight line which is fitted to the left side (steep-rising part) of this distribution with the time axis. The R - t relation is determined as follows. A time spectrum of a hit can be expressed by

$$\frac{dN}{dt} = \frac{dN}{dR} \times \frac{dR}{dt}, \quad (3.1)$$

where N denotes the number of events and R denotes the minimum distance from a wire to a track. Suppose distribution of track positions in a cell is uniform, i.e. $dN/dR = C$ (=constant). The assumption was met very well for our drift chambers if tracks were selected to pass normal to the chamber

plane. Then, the integral of Eq.(3.1) gives the R-t relation;

$$\int_{T_0}^T \frac{dN}{dt} dt = C \times [R(T) - R(T_0)] = C \times R(T) , \quad (3.2)$$

where $R(T_0)$ equals to zero by definition. Figure 3.1(b) shows an example of the integrated distribution, i.e. the left hand side of Eq.(3.2), as a function of the integration limit T . The distribution levels off when $R(T)$ reaches its maximum, i.e. a half of the cell size (4 mm). Thus R-t relation, namely the distance R as a function of T , is given by the curve in Figure 3.1(b).

We now discuss about determination of the chamber positions in our experimental setup. Prior to the experiment, a rough survey was performed with levels and optical instruments. Its nominal accuracy was 1 mm. Much more precise positioning was required to achieve high-resolution tracking, and hence determination of momentum and/or vertex position. We took the following paths to realize it. At first, calibration data were taken with the analyzing magnet turned off; this gave abundant straight tracks. Using these events chamber's mutual positions were adjusted until they correctly reconstructed these "straight" tracks.

Next, the chamber's local coordinate system was located with respect to the calorimeter and the target.¹ To this end, we used events containing electron or positron tracks, and events reconstructed as the $K_L \rightarrow \pi^+ \pi^- \pi^0$ ($\pi^0 \rightarrow 2\gamma$) decay. With the former events, the track position projected on the calorimeter by the chamber system was compared with the cluster position determined by the calorimeter itself (see Section 3.3.2). With the latter events, the reconstructed K_L momentum vector was extrapolated back to the target position. In this way, the chamber's local coordinate system was re-positioned to conform with the other detectors.²

3.1.2 Track Search

In the spectrometer system, a track was sectionally straight in both upstream and downstream sections of the magnet and was bent horizontally by the magnetic field. Thus, a track finding and fitting procedure was to reconstruct straight tracks separately in both sides of the magnet, and to match them at the center.

¹The absolute coordinate system was defined using the plane of the calorimeters front face and the center of the production target. Thus it was essential to establish the relation.

²It was necessary to use these two sets of events to fix the offset and direction of the local coordinate system.

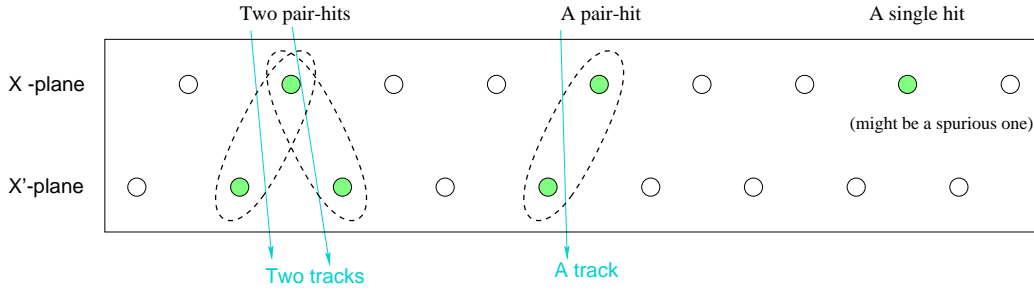


Figure 3.2: Schematic view of pair-hit search

Track finding (2-dimensional)

The track finding is a procedure to form a straight line by connecting hit wires. In this subsection, chambers having the same view (X or U or V) on one side of the magnet (upstream or downstream) are grouped together, and straight tracks in a plane (2-dimensional) are searched separately in each group.⁸ As described in previous chapter, each drift chamber set consisted of 6 readout planes X-X', U-U', and V-V'. Adjacent planes, primed and non-primed, were staggered by a half-cell size and were treated as pair in the following analysis. We requested a track to register hits in both planes. This “pair-hit search” procedure is schematically shown in Figure 3.2. A genuine track candidate, shown at the center in the figure, had to have a “pair-hit”, i.e. two single hits adjacent each other. Successive two hits in a plane and a sandwiched single hit in the other, as shown on the left, were treated as two pair-hits here though they might belong to a single track. An isolated single hit, shown on the right, was assumed to be a spurious one. To be identified as a hit, its hit time was required to be within a window from $T_0 - 10$ ns to $T_0 + 120$ ns which covered drift time corresponding to a half cell size plus a margin. Also note that if plural hits existed within this time window only the first hit was used for simplification.

The next step of track finding was to search for a combination of pair-hits belonging to a single track. This task was started with the downstream X-view chambers (DC3X and 4X) due to the following two reasons. First, there were in general fewer hits in downstream chambers because background particles, especially low momentum particles, were swept out by the analyzing magnet. Second, they were sandwiched between two trigger hodoscopes

⁸We treat the downstream U and V chambers differently. As mentioned in Sec.2.3.1, the readout electronics of these chambers were different from the others, and it resulted in somewhat worse position resolutions. We thus decided to use their hit positions as auxiliary information in the finding and fitting procedure.

(TC1X and TC2X); requirement of hits at these hodoscopes drastically reduced possible track candidates. To take an advantage of these hodoscopes, we first introduced a new concept called “road”. This was defined as follows. We listed all hit counters in TC1X and TC2X.³ A “road” was a strip spanned by two hit counters, one from TC1X and the other from TC2X. We formed all possible roads, and searched for track candidates within these roads. The process above is schematically shown in Figure 3.3(a). Note that the shaded region is excluded from the track search since it is outside of any roads. Up to this point, we searched for track candidates using only hit wire information. We can obtain more precise track parameters with drift time information from each wire. We fitted the hit positions to the function of $X = aZ + b$. As is well known, a drift chamber has a left-right ambiguity in determining the hit position. We checked both left and right case for each hit, and then selected a combination that gave the minimum χ^2 . We now obtained a set of track candidates, and their associated parameters, in the downstream Z-X plane.

The finding procedure in upstream X-view chambers was the same as that in downstream chambers except for definition of a road. In stead of TC2X hits, the X positions at the magnet center extrapolated from downstream track candidates were used. The role of TC1X was replaced by an area occupied by the neutral beam in the decay volume, from which any decay products originated. An example is shown in Fig.3.3(b). After finding track candidates, we also checked an existence of a hit at the corresponding counter in TC0X. And then, we performed the same procedure to get the track parameters in upstream X-view chambers.

Our next task is to find tracks in the upstream U- and V-view chambers. In this case, since we had no convenient device to define a road, we simply examined all possible combinations of pair-hits. The only requirement was that a candidate track had to pass through the beam region in the decay volume. Then the track parameters were obtained in a similar manner.

Track finding (3-dimensional)

Now we combine track segments in X,U, and V planes to construct 3-dimensional tracks. This procedure was actually carried out only in the upstream section.⁸ To this end, we chose two track candidates, one from the Z-U plane and the other from the Z-V plane, and linked together to form a 3-dimensional track. We examined it by imposing the following conditions. The qualified track, when projected onto the Z-Y plane, had to pass through the magnet

³In order to allow tracks to pass through the central gap of TC1X, the beam hole of TC1X was treated as a counter which was always fired in the “road” definition procedure.

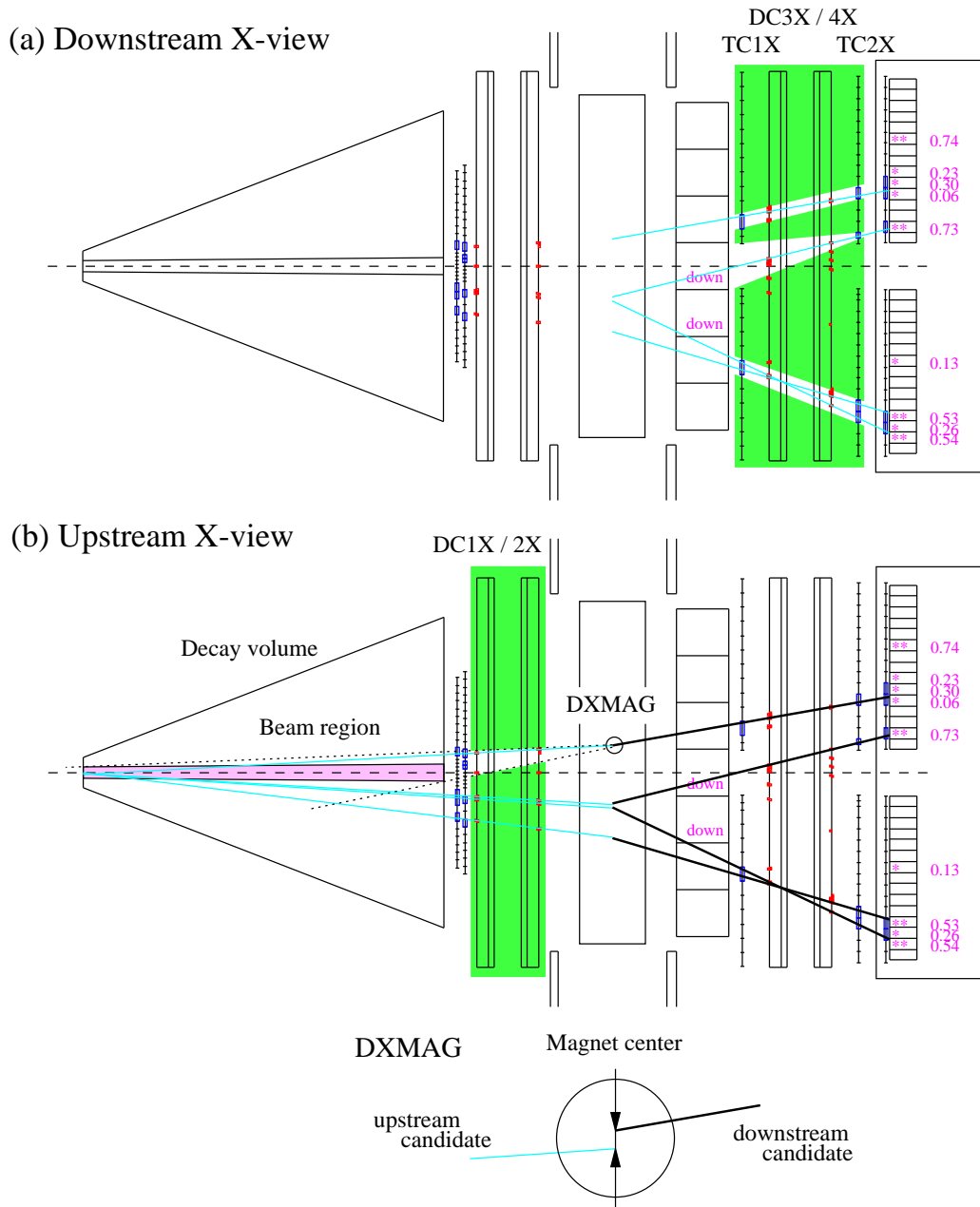


Figure 3.3: Schematic view of track search in X-view chambers. (a) Track search in downstream X-view chamber. Hits in TC1X and TC2X defined roads, shown as unshaded area. Four track candidates were found in this example. (b) Track finding in upstream X-view chamber. A road was defined by the information of downstream track candidates and the beam region in the decay volume. Only one roads is schematically shown as unshaded area.

aperture, the hit counters in TC2Y, and the front face of the calorimeter. In addition, the projection onto the Z-X plane had to be consistent with at least one of the track candidates formed with DC1X and DC2X. The actual criteria of the consistency was that the distance in the X-direction between them, measured at DC1X and DC2X, should be less than 2 mm.

Now we have two sets of track candidates; one is upstream 3-D tracks, and the other is downstream 2-D (Z-X plane) tracks. We picked up a pair of tracks, one from each set, and checked the following two conditions to make a consistent bent track. One condition is concerned with consistency of the two tracks at the magnet center, and the other is related to the downstream trajectory in the Z-Y plane. We extrapolated each track (downstream and upstream) to the magnet center, and calculated the difference in X-positions. This difference, called *DXMAG*, was required to be within 20 mm. (Much more tighter cut will be applied at the later analysis stage.) The downstream track at this stage had no Y information (2-D track). We extrapolated the upstream Z-Y trajectory, and adopted it as that of the downstream track. We then checked whether or not this 3-D track had actual hits in the downstream U- and V-view chambers as well as in the TC2Y hodoscope.

This is the end of the track finding process; we now have sets of track candidates, continuous from upstream to downstream of the magnet, with appropriate hits in all chamber planes and counter hodoscopes. Together with their track parameters, they were handed over to the next “fitting” process.

Precision track fitting

The purpose of the step is twofold: one is to obtain more accurate track parameters by an overall fit, and the other is to reject “bad” tracks with some criteria. It proceeded as follows. First we fitted all hit positions of the upstream 12 chambers (DC1/DC2 of X-X' U-U' V-V') to a straight line (3-D track), and calculated the χ^2 -value of the fit. Here the chamber's position resolution was taken to be 220 μm through all the chambers. We then calculated the confidence level associated with it. The resultant distribution, shown in Figure 3.4, should be flat if our χ^2 -distribution was obtained with ideal statistical ensemble. In reality, it shows a flat distribution with a sharp peak around $\text{CL} \simeq 0$. Most of the tracks in the peak were expected to stem from a false “track”, connecting unrelated hit points. However, they might contain a real track which had one or more spurious hits by, for example, an additional track crossing accidentally. With an intention to save those, we did repeated fits. Namely, we accepted the fit (and the track) if its confidence level is 1% or bigger. If not, we removed a hit one by one intentionally

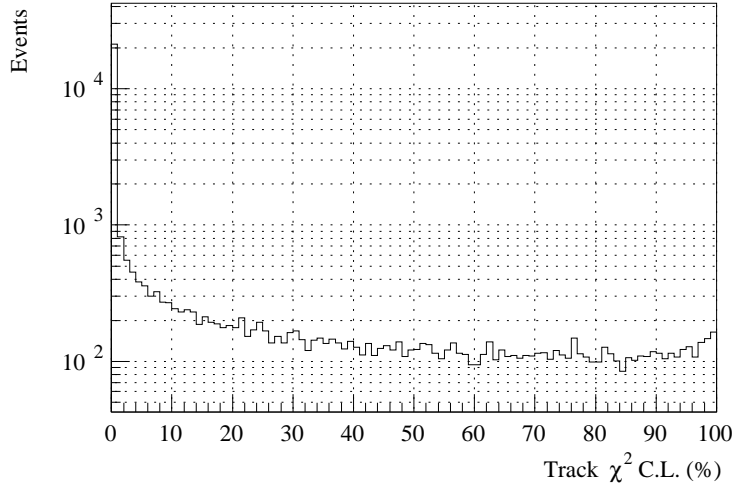


Figure 3.4: The confidence level distribution of the fit for the upstream chambers. All the hits from 12 readout planes were used for the fit. The peak around $CL \simeq 0\%$ contains false track as well as spurious hits (see text).

and recalculated its confidence level. This procedure was repeated until it found the fit with $CL \geq 1\%$ or there were only 9 original hits (out of 12 hits) left for the fit.

Having determined the best track parameters, we again calculated $DXMAG$, the difference in X-positions extrapolated by upstream and downstream tracks. This time, we applied a tight cut on $DXMAG$; it was especially useful to remove events in which one of the pions decayed into a muon inside the magnet. Note that the π -decay events turned out to be one of the most “dangerous” backgrounds (see Section 4.3). To determine the cut value, we made actual $DXMAG$ distributions as a function of observed track momentum p (see Section 3.2 for p). We obtained the width (σ) by a fit with the Gauss function. We employed a standard 3σ cut, which is shown in Figure 3.5. The curve in the figure was obtained by fitting the points to the function of $\sqrt{c_1^2 + (c_2/p)^2}$, where c_1 , c_2 denote some constants. It indicates that the dispersion in $DXMAG$ was originated dominantly from chamber resolution (related to c_1) and multiple Coulomb scattering (related to c_2/p).

3.2 Momentum of Charged Particles

We present in this section a method to determine charged particles’ momentum starting with track parameters obtained in the previous section. We

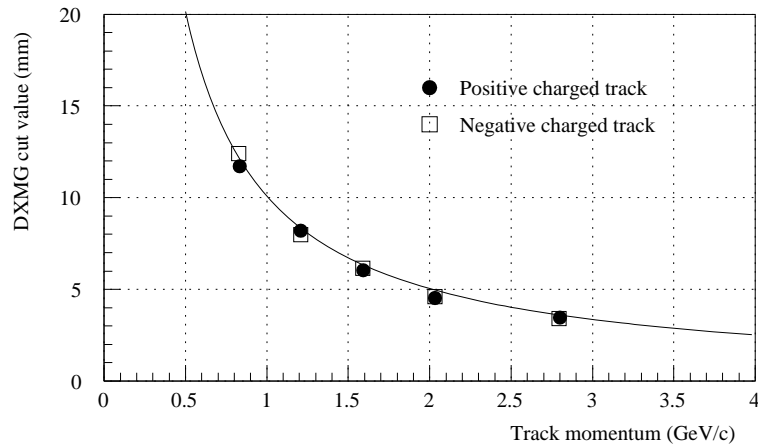


Figure 3.5: The cut value (3σ) of $DXMAG$ as a function of momentum. The deviation σ was determined by the Gaussian fit to the actual $DXMAG$ distributions. The curve in the figure was obtained by fitting the points to the function $\sqrt{c_1^2 + (c_2/p)^2}$. See text for c_1 and c_2 .

employed an effective field approximation for this purpose. We assumed a uniform magnetic field inside the magnet gap. The momentum of a charged particle is given by

$$p = 0.3qBR / \cos \lambda, \quad (3.3)$$

where p is the momentum in GeV/c , q the charge number of the particle, B the field strength in Tesla, R the radius of curvature in meter and λ the pitch angle.

The effective field B was determined in the following way. Prior to the experiment, we measured actual magnetic fields inside and outside the magnet gap. Given particle's momentum and incident trajectory, we could trace it with the actual magnetic field.⁴ The radius R could be calculated from the kick angle between upstream and downstream track directions. With R and p (and λ), an effective value of B for this particular track was determined from Eq.(3.3). We averaged such B 's over many trajectories with momenta generated by a Monte Carlo simulation. Having determined the effective B , momentum p for each track could be calculated. The pitch angle of upstream track was used as λ in the calculation.

⁴The Runge-Kutta method was employed.

3.3 Calorimetry

In order to measure energies and positions of electrons and photons, we used electromagnetic calorimeter, which was composed of CsI crystals. The scintillation light output of each crystal block, read by a photomultiplier and recorded as ADC counts, was proportional to the energy deposit by a particle. An electron or photon incident on a crystal caused an electromagnetic shower and deposited almost all energy to crystals around the incident position. To get their energies, we had to know, at first, the coefficients to convert an ADC count to a energy, called “calibration constant”. We also had to identify a group of crystals, called “cluster”, which belonged to a passage of one particle. These were realized by the energy calibration and the cluster finding procedures presented in this section. The position measurement of electromagnetic particles was also done using the cluster information. The method was checked by electron tracks, whose position could be measured both by the calorimeter and by the drift chambers.

3.3.1 Energy Calibration

Before any precise calibration of the calorimeter, the gain of photomultipliers were adjusted so as to get uniform pulse height to the same energy deposit. Actually, the number we made uniform was the ADC count to the passage by a minimum ionizing particle such as a muon and a pion. The deviation of each photomultiplier gain was adjusted within $\pm 10\%$ at the beginning of the entire experiment.

The gain change, for example, due to the decrease of scintillation lights, which was caused mainly by the radiation damage, was treated by the precise energy calibration. It was performed using electron tracks in the $K_L \rightarrow \pi e \nu$ decay (K_{e3}) obtained by a special trigger to enrich K_{e3} events. The K_{e3} candidates were required two tracks, one in each arm, with a vertex in the decay volume, and Čerenkov counter hits corresponding to one of the two tracks. The momentum of the electron and its incident position on the calorimeter were obtained by the spectrometer, as described in the previous section. At first, we chose one block to be calibrated. We requested this block to have more than 60% of the summed energy which included energy deposits in the surrounding 8 blocks. In case of the peripheral blocks, additional cuts on the incident position were imposed to avoid the influence of shower leakage. Now, the ratio of the summed energy (E) to the momentum (p) measured by the spectrometer was defined as E/p . Since electrons lost its all energy in the calorimeter by creating a shower, E/p should be unity within the resolution. We fitted the E/p distribution to the Gaussian shape

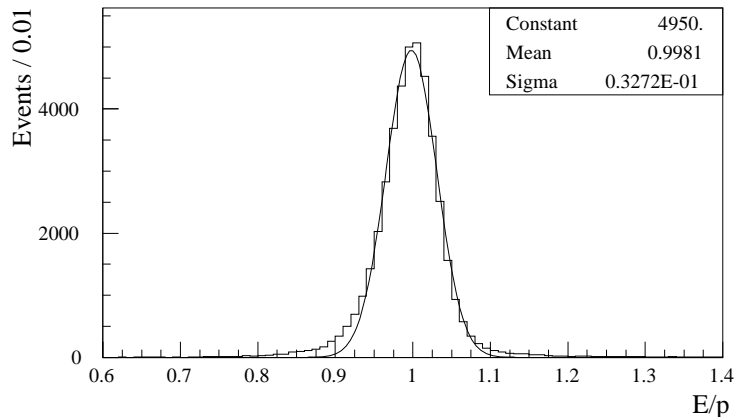


Figure 3.6: E/p distribution of all blocks for electrons. The curve indicates the best fit to the Gaussian form. The deviation at lower tail was considered to be the effect due to the radiation from electrons.

and adjusted the calibration constant of the target block so that the mean of E/p became one. We applied this process to all blocks and then repeated this entire procedure again with new constants. After third attempt, changes in the calibration constants were found to be within 1%, thus the process was terminated after the second iteration. Figure 3.6 shows an E/p distribution of all blocks into one histogram. The resolution of E/p was found to be about 3.3 % over all blocks.⁵

3.3.2 Cluster Finding and Cluster Position

Cluster Finding

The method of the cluster finding we adopted was to find a block which contained larger energy deposit than any of the 8 surrounding blocks. Figure 3.7(a) shows the schematics of the cluster finding procedure. When such a block had an energy of 10 MeV or more, and the summed energy including its surrounding blocks was more than 25 MeV, we considered it as a cluster. Note that if there were two clusters nearby, shown in Figure 3.7(b), the energy and position of both clusters might be incorrectly calculated. It caused the inefficiency in the analysis of physics modes. The influence of this effect due to the K_L decays could be estimated by Monte Carlo simulation, and will be discussed in Section 4.4. However, one due to accidental activities from beam backgrounds could not be treated in the same way. Its effect will

⁵The average momentum of electrons used in the calibration was about 1.5 GeV/c.

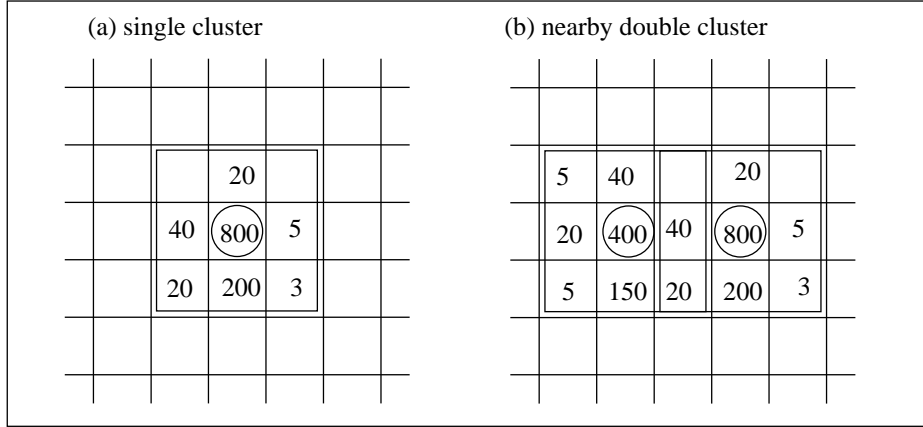


Figure 3.7: Schematic drawings of the cluster finding procedure. A number in each box indicates an energy deposit in MeV. The blocks marked with a circle were identified as a center of a cluster. Each figure represents (a) a typical case, and (b) a case in which there were two particle incident nearby and their showers merged each other. In this case, the energy of both clusters were incorrectly calculated. It caused the inefficiency in the analysis of physics modes, as will be discussed in Section 4.4.

be discussed in Section 4.5.1.

Cluster Position

Once a cluster was defined, the sum of energy (E), the center of gravity weighted by energy deposit (X_G, Y_G) were calculated. The point (X_G, Y_G) was used as the cluster position, in case that the incident particle was neither an electron nor a photon. In case of an electromagnetic component (e^\pm or γ), whose shower profile was well described by an exponential form, another calculation method was employed. Figure 3.8 shows the relation between X position of electrons measured by drift chambers (X_{DC}) and that by the calorimeter (X_G). X'_{DC} and X'_G in the figure are the local coordinates in which the center of the block was defined as the origin. It was found that the relation between X'_{DC} and X'_G also depended on the incident angle (θ) to the block, in addition to the well-known “S-curve” behavior [28]. We calculated the position X'_{calc} , as a function of X'_G and θ , by

$$X'_{calc} = b \cdot \sinh^{-1} [(X'_G/\Delta) \sinh(\Delta/b)] + A_1\theta + A_3\theta^3, \quad (3.4)$$

where Δ is a half width of a block, i.e. 35 mm. The coefficient b is a measure of the shower shape in the calorimeter while parameters A_1 and A_3 are the

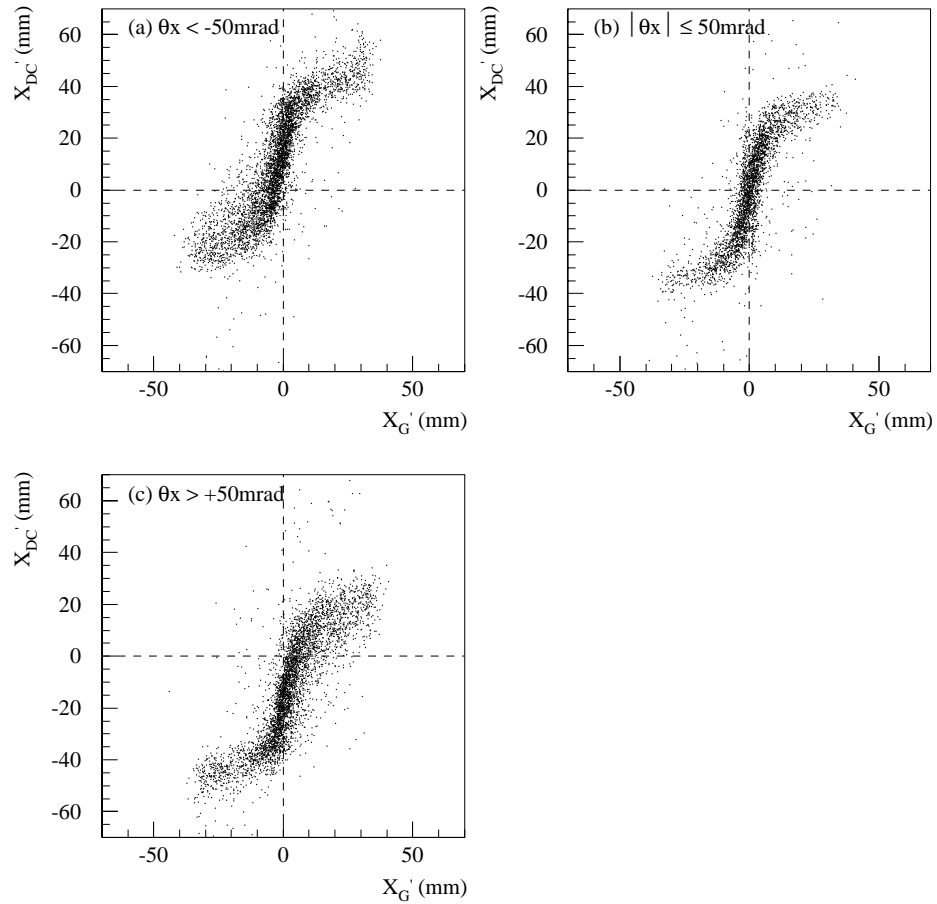


Figure 3.8: X position of electrons measured by drift chambers vs that by the center of gravity of a cluster in the calorimeter. The positions in both axes were represented in the local coordinate, explained in the text. Incident angles of electrons to the calorimeter were (a) -50 mrad or smaller, (b) within ± 50 mrad, and (c) $+50$ mrad or larger.

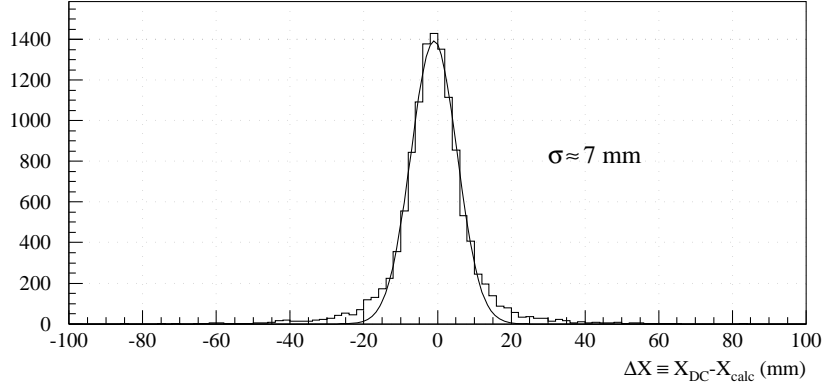


Figure 3.9: Position resolution of the calorimeter for electrons in the X-view.

correction coefficients for the incident angle. These parameters (A_1 , A_3 and b) were obtained by fitting the actual data to the function of Eq.(3.4). The position resolution, shown in Figure 3.9, was defined as difference between X'_{DC} and X'_{calc} , and was found to be about 7 mm.

3.3.3 Timing Requirement

To reduce accidental clusters, a timing requirement was imposed on signals from blocks, which were discriminated with a threshold voltage equivalent to about 50 MeV. Since the energy of incident particles extended over a wide range, the timing jitter due to the pulse height variation was a important matter. Figure 3.10(a) shows a scatter plot of TDC vs ADC counts in K_{e3} events. As can be seen in the figure, there existed obvious correlation between the hit time and the pulse height of blocks. To alleviate the timing jitter, we made a correction to TDC counts with ADC counts; the correction function was obtained by fitting the distribution to the polynomials. Figure 3.10(b) and (c) show a scatter plot of TDC vs ADC after the correction and its projection onto TDC axis, respectively. Fitting to the Gaussian shape, as shown in Figure 3.10(c), we found the timing resolution to be about 700 psec.⁶ We required a cluster to occur within ± 3.5 nsec (which is $\pm 5\sigma$ cut) of the event time. In the actual analysis process, the corrected TDC of the cluster's center block was examined. Note that in the region below 100 counts of ADC (equivalent to about 150 MeV), the dependence of TDC upon ADC value was so steep, as can be seen in Fig.3.10(a), that a careful correction was needed. Therefore, for simplicity, no timing cut was applied to the clusters

⁶ About 25 psec per count in the TDC we used.

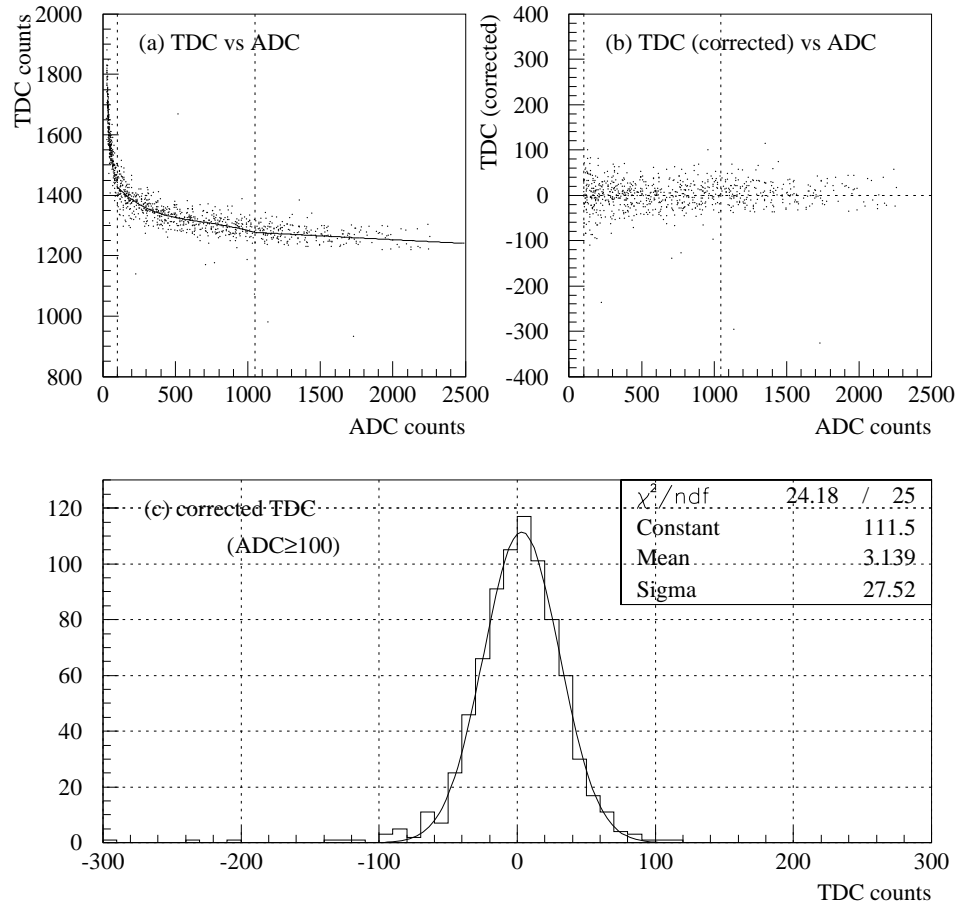


Figure 3.10: TDC distributions of the block in the calorimeter. (a) A scatter plot of TDC vs ADC counts. As can be seen in the plot, there existed clear correlation between the hit time and the pulse height of blocks. A curve in the plot represents a function, with which the correction of TDC was made. (b) The relation between ADC and TDC counts after the pulse height correction. Below 100 counts of ADC (~ 150 MeV), no correction was attempted (see text). (c) The distribution of corrected TDC counts. It is a projection of (b) onto TDC axis.

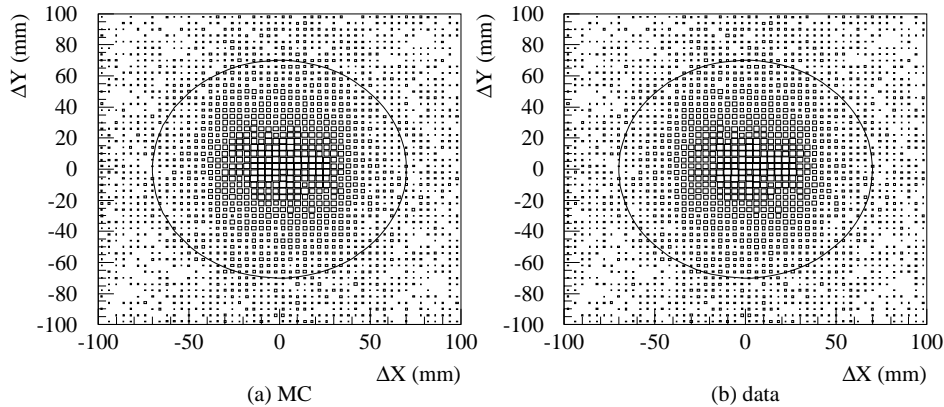


Figure 3.11: Scatter plots which indicate distance between track position and cluster position for (a) MC and (b) one set of data. They are drawn with proportional boxes. In both cases, the cluster position is represented by the center of gravity of a cluster.

with less than 200 MeV.

3.4 Particle Identification

Charged Cluster

Any charged particles, either electrons or pions, should have both tracks and clusters. We defined a “matched track” as the track whose projection onto the calorimeter was within 70 mm from a certain cluster. Figure 3.11 shows the distributions of the distance between track and cluster positions; (a) Monte Carlo events for $K_L \rightarrow \pi^+ \pi^- \pi_D^0$ and (b) an example of experimental data, respectively. $\Delta X(\Delta Y)$ in the figures were defined as $X_{DC} - X_G(Y_{DC} - Y_G)$, the distance between X(Y) position measured by drift chambers and that by the calorimeter. The cut value of 70 mm, represented as a circle in the plot, was determined from the distributions with some margins.

To identify species of charged particles, we used the information of their energy deposit in the calorimeter (E), their momentum measured by the spectrometer (p) and hits of Gas Čerenkov counter. An electron was identified as a matched track with its energy deposit in the calorimeter to be at least 200 MeV, the energy-to-momentum ratio (E/p) within the range of

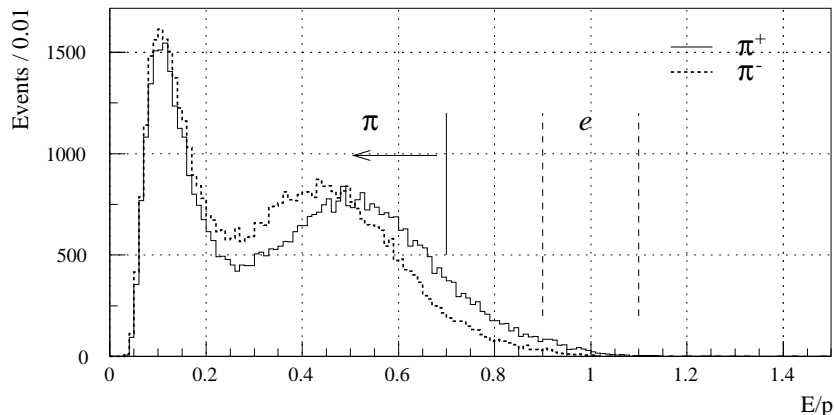


Figure 3.12: E/p distribution for π^+ (solid histogram) and π^- (dashed histogram) in events identified as $K_L \rightarrow \pi^+\pi^-\pi^0$. The $K_L \rightarrow \pi^+\pi^-\pi^0$ identification was not used the information of E/p . Pions in the region of $0.9 \leq E/p \leq 1.1$ would be misidentified as electrons.

$0.9 \leq E/p \leq 1.1$, and gas Čerenkov counter hits in corresponding cells. It can be seen in Fig.3.6, the E/p distribution for electrons, that the range was equivalent to $\pm 3\sigma$ cut.

A pion was identified as a matched track with $E/p < 0.7$. Figure 3.12 shows the E/p distribution for pions, which was obtained by pions in reconstructed $K_L \rightarrow \pi^+\pi^-\pi^0$ events, without particle identification by E/p . Note that we could not distinguish pions from protons or muons, thus what we called a pion might be a proton or a muon.

The probability to misidentify a pion as an electron was estimated to be 1.1% for π^+ and 0.3% for π^- by the number of pions in the region of $0.9 \leq E/p \leq 1.1$ in Figure 3.12. Combined with pion rejection factor of GC ($\sim 1/50$), the probability of misidentification $\pi \rightarrow e$ was expected to be $\sim 2 \times 10^{-4}$ in the worst case. The probability of misidentification $e \rightarrow \pi$ was estimated by fitting the lower tail of E/p distribution for electrons, shown in Fig.3.6, to an exponential function. It was found to be less than 3×10^{-4} in average.

Figure 3.13 shows an example of E/p distribution for the actual data at this reconstruction stage.

Neutral Cluster

A cluster which could not associate with any tracks on the matching condition, was considered as a “neutral cluster” generated by a neutral particle.

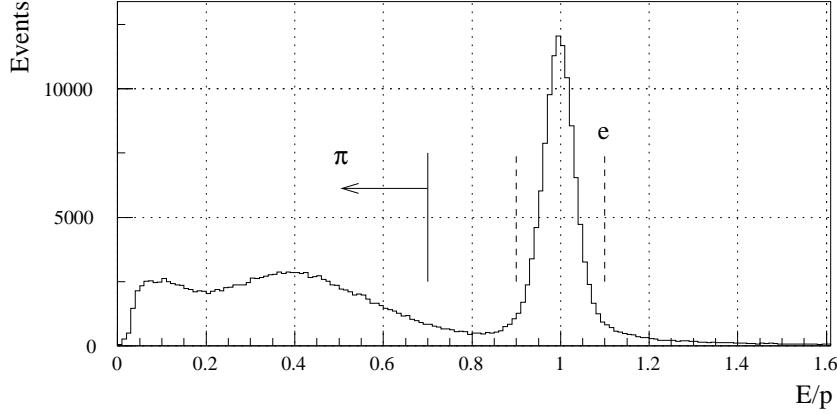


Figure 3.13: E/p distribution for the Vacuum data at the reconstruction stage of the particle identification.

And we defined a neutral cluster which have an energy of more than 200 MeV as a photon, though they might be other neutrals, for example, neutrons. Any photons were assumed to originate from a decay vertex (will be defined in the next section), and their momenta \vec{P}_γ were defined from their energy deposits and the directions of their cluster center from the vertex point.

The misidentification ($\pi \leftrightarrow e$, $\mu \rightarrow \pi$, $n \rightarrow \gamma$, etc.) would be the source of potential backgrounds in the analysis. These backgrounds could be eliminated only by kinematical constraints. Detailed consideration will be described in next chapter.

3.5 Pre-selection

The main purpose of this “pre-selection” is to reduce data size by imposing very loose conditions to the events. Before we present the detail of the conditions, we define a cross point of two straight lines (or tracks). Given two tracks, we searched for a line segment which gave the minimum distance between the two. If the segment was less than 10 mm long, its center was defined as the cross point. It is customary to use the word “Vertex” for it; however it is saved for another, more sophisticated, definition (see Sec.3.6).

The actual conditions are

- At least one track pair with unlike sign of charge,
- At least one cross point inside the region of $9.5\text{m} < Z < 13.3\text{m}$ (the decay volume),

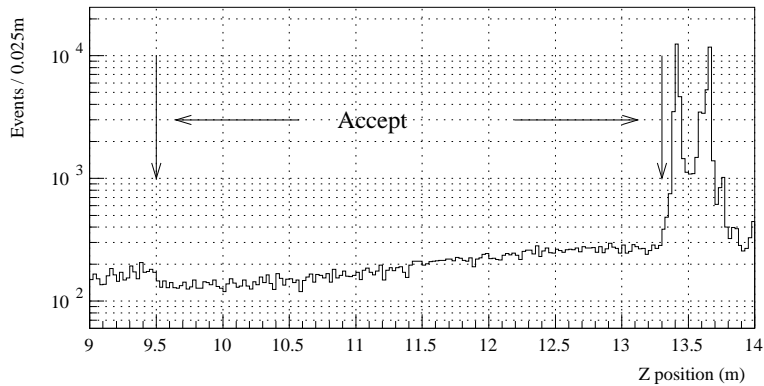


Figure 3.14: The distribution of a cross point Z position (see text for the definition). The arrows indicate the accepted region by pre-selection.

- 2 or more clusters with $E \geq 150\text{MeV}$,
- At least 2 “matched tracks” with $E/p \geq 0.7$.

These conditions were loose enough to have negligible influence on the subsequent offline analysis, but were very effective to reduce data size. The effectiveness is illustrated by Figure 3.14, which shows the actual Z position distribution of the cross point. There exist two clear peaks, corresponding with events coming from the decay volume window and the trigger counter TC0.

3.6 Decay Vertex determination

The process of event reconstruction ends with the pre-selection described in the previous section. For convenience, we describe here a process called decay vertex determination, which will be employed in the next chapter.

The decay vertex is a point where K_L decays into, for example, $\pi^+\pi^-e^+e^-$ or $\pi^+\pi^-\pi_D^0$. Existence of a well defined decay vertex is essential not only to guarantee the decay, but also to know photon’s momentum direction, if it exists.

In the actual reconstruction, we defined a vertex as a position which minimized the quantity,

$$\chi_v^2 \equiv \sum_i \left(\frac{d_i}{\sigma_i} \right)^2, \quad (3.5)$$

where i specifies a charged track in an event and d_i denotes the distance between the i -th track and the vertex point to be determined. The weight-

ing function σ_i in the denominator represents the extrapolation error at the vertex. We call σ_i the track-vertex resolution. Our first task is to determine these resolutions.

3.6.1 Determination of Track-Vertex Resolution

We expect the track-vertex resolution σ_i to have the following functional form:

$$\sigma_i = (z_0 - z) \sqrt{C_1^2 + \left(\frac{C_2}{p_i}\right)^2}. \quad (3.6)$$

The factor $\sqrt{C_1^2 + (C_2/p_i)^2}$ has the same physical basis as that of the *DXMAG* distributions; the C_1 term from chamber's position resolution, and C_2 term from the effect of multiple Coulomb scattering. The factor $(z_0 - z)$ represents the lever arm length of extrapolation. These parameters (C_1 , C_2 , and z_0) were determined with actual events. Actually, the following interactive procedure was applied to the $K_L \rightarrow \pi^+ \pi^- \pi_D^0$ events.

Suppose we know the exact vertex position, then the track-vertex distance d_i shows a distribution characterized by width σ_i . In particular, it can be determined as a function of p or z and thus the three parameters can be extracted from a fit. With these parameters, we can “predict” the value of σ_i from the track parameters above.⁷ Given the value of σ_i for each track, we can determine the vertex position through Eq.(3.5). With appropriate initial values for three constants (C_1 , C_2 , and z_0), we repeated the whole procedure several times until the constants converged sufficiently.

Figure 3.15 shows the track-vertex resolution of electron and pion tracks as a function of Z vertex position. The straight lines in the figure were linear fits to the points. These two straight lines cross the horizontal axis at $z = 13.9$ m, which gives z_0 . Fig.3.15 clearly illustrates validity of the functional form $(z_0 - z)$ in Eq.(3.6).

In order to extract the other factor in Eq.(3.6), we plotted a distribution of $d/(z_0 - z)$, the vertex-track distance divided by $z_0 - z$, and obtained its width by fitting. Fig. 3.16 shows the resultant width (resolution) as a function of the momentum; (a) for the electron tracks and (b) for the pion tracks. These data points can be well expressed by the function $\sqrt{C_1^2 + (C_2/p)^2}$. We obtained $C_1 = 0.38 \times 10^{-3}$ and $C_2 = 1.3 \times 10^{-3}$ GeV/c for pion, and $C_1 = 0.77 \times 10^{-3}$ and $C_2 = 1.5 \times 10^{-3}$ GeV/c for electron.

⁷This is an iterative process because we need the vertex position Z to determine σ_i . The iteration converged very quickly.

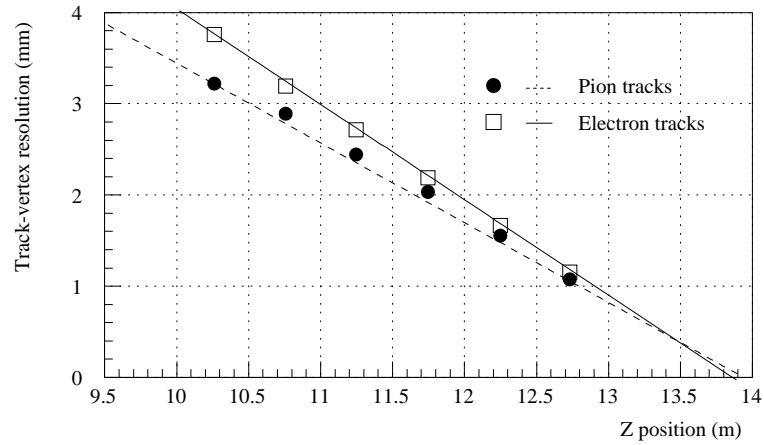


Figure 3.15: The track-vertex resolution as a function of Z position. The lines in this figure were obtained by linear fitting to the data points. The parameter z_0 is given by the crossing point between the line and the horizontal axis.

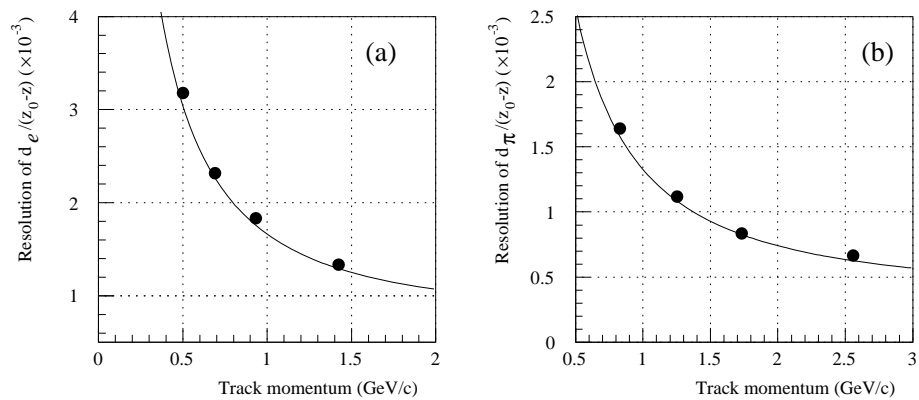


Figure 3.16: The resolution of (a) $d_e/(z_0 - z)$ and (b) $d_\pi/(z_0 - z)$ as a function of track momentum. The indexes e and π , indicate electrons and pions tracks, respectively. The curves in this figure were obtained by fitting to the function $\sqrt{C_1^2 + (C_2/p_i)^2}$.

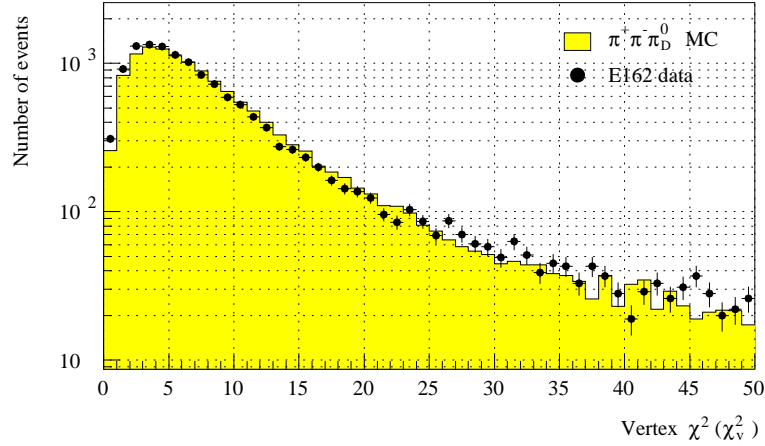


Figure 3.17: The χ_v^2 distributions of the real events (solid dots) and the Monte Carlo simulation (hatched histogram). The events were to satisfy all the conditions, except the χ_v^2 cut, imposed on the $K_L \rightarrow \pi^+\pi^-\pi_D^0$.

3.6.2 Calculation of Vertex χ^2

Now, a decay vertex was calculated as the point which minimized Equation (3.5). Figure 3.17 shows the χ_v^2 distribution for the following event samples: the actual data (dot) reconstructed as the $K_L \rightarrow \pi^+\pi^-\pi_D^0$ without this χ_v^2 cut, and the corresponding data (histogram) by a Monte Carlo simulation. Both distributions agreed well with each other.

Chapter 4

Analysis of the Physics Modes

The analysis of the physics modes, $K_L \rightarrow \pi^+\pi^-e^+e^-$ and $K_L \rightarrow \pi^+\pi^-\pi^0(\pi^0 \rightarrow e^+e^-\gamma)$, will be presented in this chapter. Although our main purpose is to measure the branching ratio of the former mode, it is also important to identify and study the latter. This is because the mode, denoted as $K_L \rightarrow \pi^+\pi^-\pi_D^0$, has the same decay products as the signal mode, except for an extra photon, with a large branching ratio. Thus, it can be used to determine an incident K_L flux. At the same time, it is expected to become a major background source.

The analysis of physics modes consists of several steps. The first step is called “General Event Selection”. In this step, events containing π^+ , π^- , e^+ and e^- are selected from the event sample obtained in the previous section. In addition, loose kinematical cuts and preparatory background rejection cuts are applied. Next, reconstruction of the normalization mode is carried out by applying tight kinematical cuts. The number of reconstructed events gives information on the incident K_L flux. Then, the signal mode is identified among overwhelming background events. This step is a heart of the present analysis. Finally, the calculation of branching ratio as well as estimation of possible systematic errors are performed.

Figure 4.1 shows the schematic flowchart of the analysis process. Below, we will describe each step in detail.

4.1 General Event Selection

The main aim of the General Event Selection is to select candidate events for both $K_L \rightarrow \pi^+\pi^-\pi_D^0$ and $K_L \rightarrow \pi^+\pi^-e^+e^-$ modes. Specifically, events were requested to have 4 (and only 4) charged particles composed of π^+ , π^- , e^+ and e^- with a common vertex in the beam region. Then loose kinematical

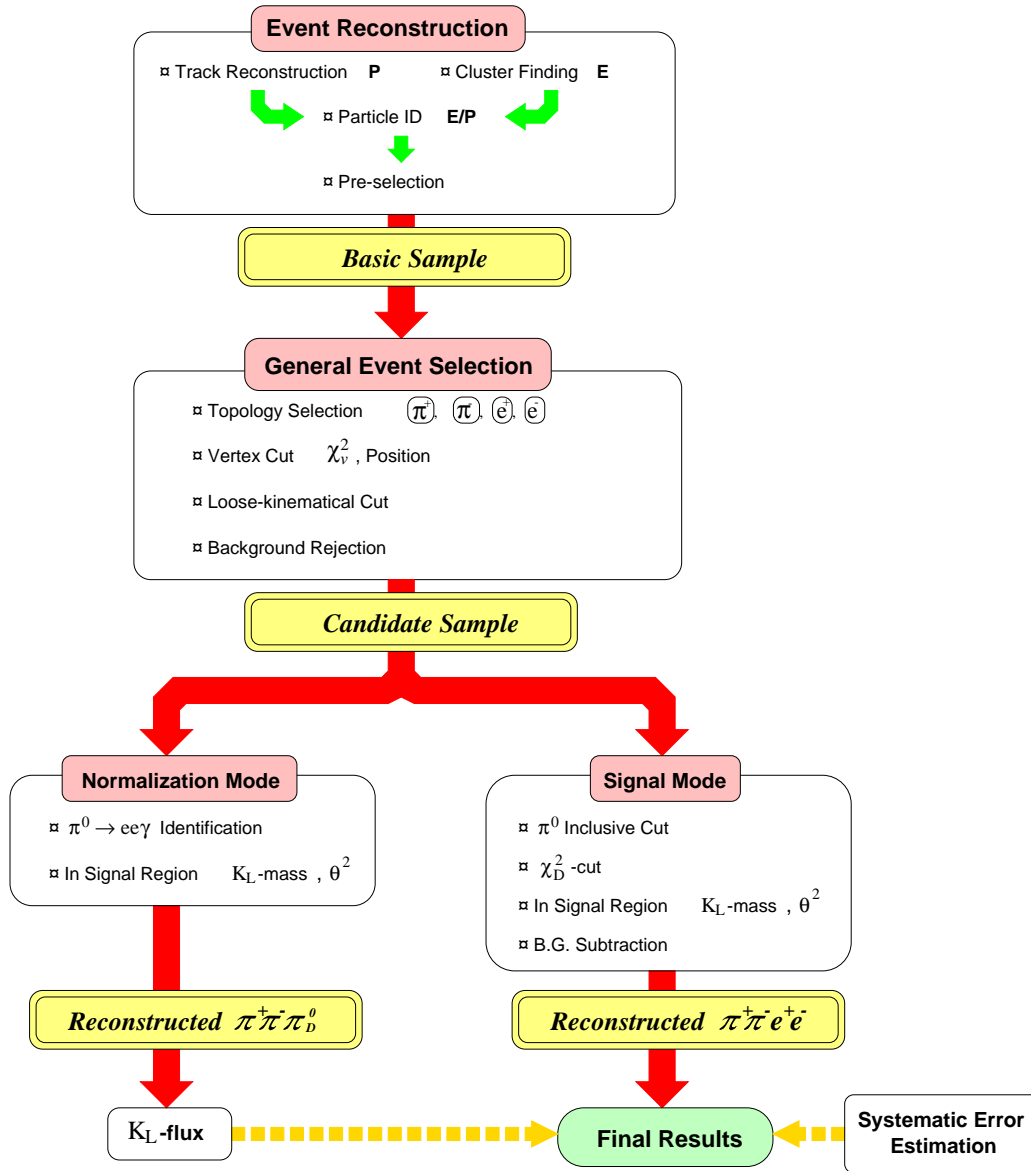


Figure 4.1: Schematic flowchart of the analysis. “Event Reconstruction” is to obtain basic physics quantities from raw data (Chapter 3). “General Event Selection” is to select candidate events for the physics modes. “Normalization Mode” and “Signal Mode” are the analysis step to identify $K_L \rightarrow \pi^+\pi^-\pi_D^0$ and $K_L \rightarrow \pi^+\pi^-e^+e^-$ events. The final branching ratio is calculated from the reconstructed events with subsidiary information by the Monte Carlo simulation.

cuts were applied to reduce data size. Finally, additional cuts were applied to reject backgrounds coming from nuclear interactions, external photon conversions etc.

Before we go into the main subject, we should comment on distinction between the normalization and signal modes. Up to now, bias due to an extra photon has been carefully avoided. Both hardware trigger and “Basic Reconstruction” process are common to the two modes. This is also true in the “General Event Selection” process.¹

4.1.1 Event Topology Selection

The analysis started with the “Basic Sample” obtained in Sec.3.5. At first, we selected events which had 4 (and only 4) charged tracks composed of π^+ , π^- , e^+ , and e^- candidates.

Next, we formed a vertex from these tracks by the method described in Section 3.6. We applied a cut on the vertex χ^2 (χ_v^2) to guarantee a well defined decay point. The actual cut value of $\chi_v^2 \leq 20$ was chosen as the following way. Figure 4.2 shows χ_v^2 distributions of the actual events (solid dots), the $K_L \rightarrow \pi^+\pi^-\pi_D^0$ Monte Carlo simulation (light-hatched histogram) and $K_L \rightarrow \pi^+\pi^-e^+e^-$ (dashed histogram) simulation. They are normalized to have the same maximum entries. It turns out that the $K_L \rightarrow \pi^+\pi^-\pi_D^0$ events with a π -decay ($\pi \rightarrow \mu\nu$) in flight make non-negligible backgrounds to the signal mode. The dark-hatched histogram shows a subset of $\pi^+\pi^-\pi_D^0$ simulation events with a π -decay (actually, decay in the region from decay vertex to DC1X). The cut value is shown by the arrow in the figure, was determined by looking at these distributions; it removed the tail part stemmed from π -decay events and/or spurious events. The χ_v^2 cut removed 75% of the π -decay events, while retained 78% of $K_L \rightarrow \pi^+\pi^-\pi_D^0$ without π -decay or $K_L \rightarrow \pi^+\pi^-e^+e^-$ events.

We also required a position of vertex to be inside the beam region of decay volume. The actual cut values are

$$\begin{aligned} |\angle X| &< 4 \text{ mrad} \\ |\angle Y| &< 20 \text{ mrad} \\ 9.6 \text{ m} &< Z < 13.25 \text{ m} \end{aligned} \quad (4.1)$$

where $\angle X$ and $\angle Y$ are expressed by the angle projected onto appropriate plane. They were determined from the beam collimators and the decay volume size.

¹Since the π^0 decays immediately in the $K_L \rightarrow \pi^+\pi^-\pi_D^0$ mode, it looks like a decay with a single vertex for our experimental resolutions.

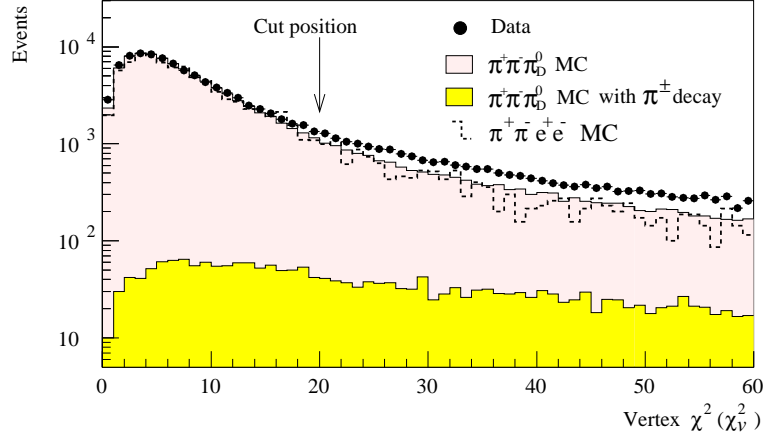


Figure 4.2: The vertex χ^2 distributions (χ_v^2). Shown are the actual data (solid dots), the $K_L \rightarrow \pi^+\pi^-\pi_D^0$ Monte Carlo simulation (hatched histogram) and the $K_L \rightarrow \pi^+\pi^-e^+e^-$ simulation (dashed histogram). The simulations are normalized to have the same maximum entry as the real data. The dark hatched histogram is a subset of $K_L \rightarrow \pi^+\pi^-\pi_D^0$, in which one of the pion decayed into a muon in the region between the vertex and DC1X. The cut value is shown as an arrow.

4.1.2 Loose Kinematical Cut

We applied very loose kinematical cuts to the data at this stage. Its purpose is purely reduction of the data to convenient size. We arranged two sets of conditions, one for $K_L \rightarrow \pi^+\pi^-e^+e^-$ and the other for $K_L \rightarrow \pi^+\pi^-\pi_D^0$, and retained those events that fulfilled either of the two (logical OR). The actual conditions are

$$\begin{aligned} 410 \text{ MeV}/c^2 &\leq M_{\pi\pi ee} \leq 590 \text{ MeV}/c^2 \\ \theta^2 &\leq 100 \text{ mrad}^2 \end{aligned} \quad (4.2)$$

for $K_L \rightarrow \pi^+\pi^-e^+e^-$ candidates, and

$$\begin{aligned} 410 \text{ MeV}/c^2 &\leq M_{\pi\pi ee\gamma} \leq 590 \text{ MeV}/c^2 \\ 100 \text{ MeV}/c^2 &\leq M_{ee\gamma} \leq 170 \text{ MeV}/c^2 \\ \theta^2 &\leq 100 \text{ mrad}^2 \end{aligned} \quad (4.3)$$

for $K_L \rightarrow \pi^+\pi^-\pi_D^0$ candidates. Here θ denotes the angle between the line from the target to the decay vertex and the reconstructed momentum vector summed over the entire decay products (see Fig.4.3). Hereafter, we call θ the target reconstruction angle. If the parent particle came from the target

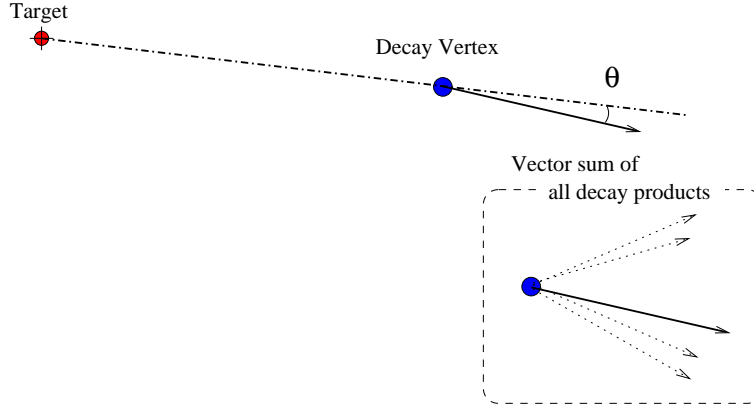


Figure 4.3: Definition of the target reconstruction angle θ .

and there was no particle escaped from detection, θ should be zero within the experimental resolution.

In searching for $K_L \rightarrow \pi^+\pi^-\pi_D^0$ candidates, if there were more than one photon candidates in an event, we selected the one with which the invariant mass of $e^+e^-\gamma$ ($M_{ee\gamma}$) was closest to π^0 mass (M_{π^0}).

4.1.3 Backgrounds Rejection

We introduce here background rejection cuts, which are useful to remove events coming from external photon conversions, nuclear interactions and pion decay events.

Backgrounds from Photon Conversions

There are several K_L decay modes which can mimic $K_L \rightarrow \pi^+\pi^-e^+e^-$ by an external photon conversion process, i.e. a process in which a photon converts into an e^+e^- pair in a material. Among them, the $K_L \rightarrow \pi^+\pi^-\pi^0(\pi^0 \rightarrow 2\gamma)$ and $K_L \rightarrow \pi^+\pi^-\gamma$ modes are potentially most dangerous because of their large branching ratio and existence of π^+ and π^- in the decay products. We examined the e^+e^- invariant mass (M_{ee}) to distinguish this process ($M_{ee} = 0$ ideally). Figure 4.4 shows the M_{ee} distributions, all obtained by Monte Carlo simulations, of the following processes:

- (a) $K_L \rightarrow \pi^+\pi^-\pi_D^0$.
- (b) $K_L \rightarrow \pi^+\pi^-e^+e^-$.
- (c) $K_L \rightarrow \pi^+\pi^-\pi^0(\pi^0 \rightarrow 2\gamma)$.

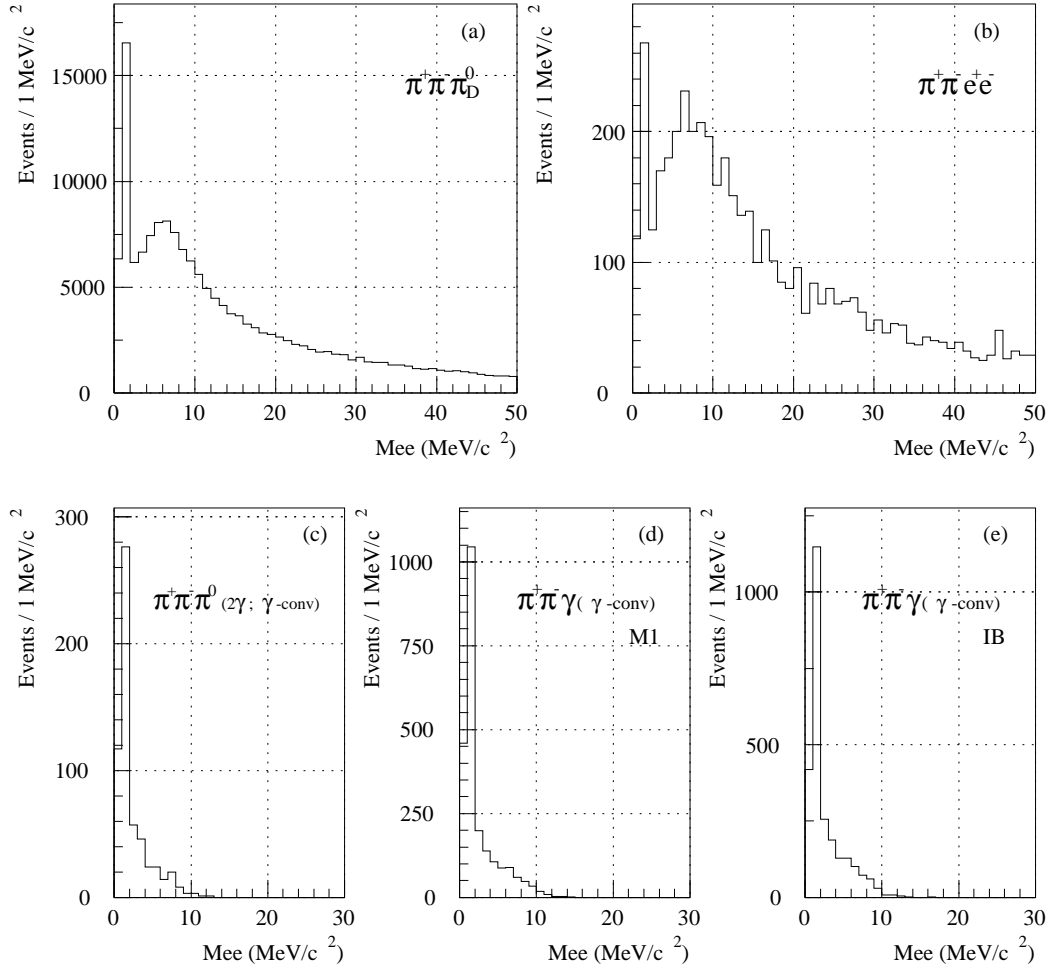


Figure 4.4: The reconstructed M_{ee} distributions. (a) $K_L \rightarrow \pi^+ \pi^- \pi_D^0$ MC, (b) $K_L \rightarrow \pi^+ \pi^- e^+ e^-$ MC, (c) $K_L \rightarrow \pi^+ \pi^- \pi^0$ ($\pi^0 \rightarrow 2\gamma$) with the γ conversion, (d) $K_L \rightarrow \pi^+ \pi^- \gamma$ (direct M1 emission) MC with the γ conversion and (e) $K_L \rightarrow \pi^+ \pi^- \gamma$ (internal bremsstrahlung) MC with the γ conversion.

(d) $K_L \rightarrow \pi^+\pi^-\gamma$ (direct M1 emission).

(e) $K_L \rightarrow \pi^+\pi^-\gamma$ (internal bremsstrahlung).

In the simulations (c) through (e), one photon was forced to convert into e^+e^- at the materials in the decay volume window. As expected, the M_{ee} distributions from the photon conversion peaked near $M_{ee} \simeq 0$. We demanded M_{ee} to be larger than 4 MeV/c².

The photon conversion process had another characteristic feature. Most of them occurred at the materials upstream of DC1, namely the decay volume window and TC0 scintillators.² The tracks by these pairs had almost the same trajectory up to the magnet. As a result, these tracks inclined to share many hit cells among the 12 layers of DC1X through DC2X'. When the number of shared cell (N_{shared}) was large, M_{ee} was often calculated incorrectly because of erroneous track parameters. Figure 4.5 shows the N_{shared} distributions for the same data sets (a) through (e) in Fig.4.4. From these distributions, we determined to demand $N_{\text{shared}} < 8$. By studying the Monte Carlo simulations, it was found that these cuts (M_{ee} and N_{shared}) excluded more than 98.7% of e^+e^- pairs originating from the photon conversion, while the efficiencies for $K_L \rightarrow \pi^+\pi^-e^+e^-$ and $K_L \rightarrow \pi^+\pi^-\pi_D^0$ modes were found to be 86% and 78%, respectively.

Pion momentum asymmetry

Backgrounds also stemmed from nuclear interactions. They were generated by interactions of abundant neutrons in the beam with, for example, gas atoms in the decay volume. Their rejection was especially important for the Helium data. In fact, there were many ways to remove them; obviously the kinematical cut imposed on the invariant mass was the most powerful means. Here we describe a method called a pion asymmetry cut.

We first note that our detector system can reliably distinguish electrons from other particles; however, what we call a pion might be a muon or a proton. Therefore if the nuclear interactions produced two charged particles, such as protons and/or π^\pm , accompanying π_D^0 ($\pi_D^0 \rightarrow e^+e^-\gamma$), they might be identified as $\pi^+\pi^-e^+e^-$ candidates. Now we note the nuclear interactions, such as $nN \rightarrow \pi^-pX$, tend to produce fast protons. This results in a large momentum imbalance between the two charged (+/-) particles. This fact is in contrast with $K_L \rightarrow \pi^+\pi^-e^+e^-$, in which the π^+/π^- momenta are more or less balanced. Thus we defined an asymmetry in pion momentum by $A_{+-} = (p_{\pi^+} - p_{\pi^-})/(p_{\pi^+} + p_{\pi^-})$, and applied a cut on this quantity.

²Since a track reconstruction demand a corresponding fire on the TC0 scintillators, a track by a photon conversion downstream TC0 is forbidden.

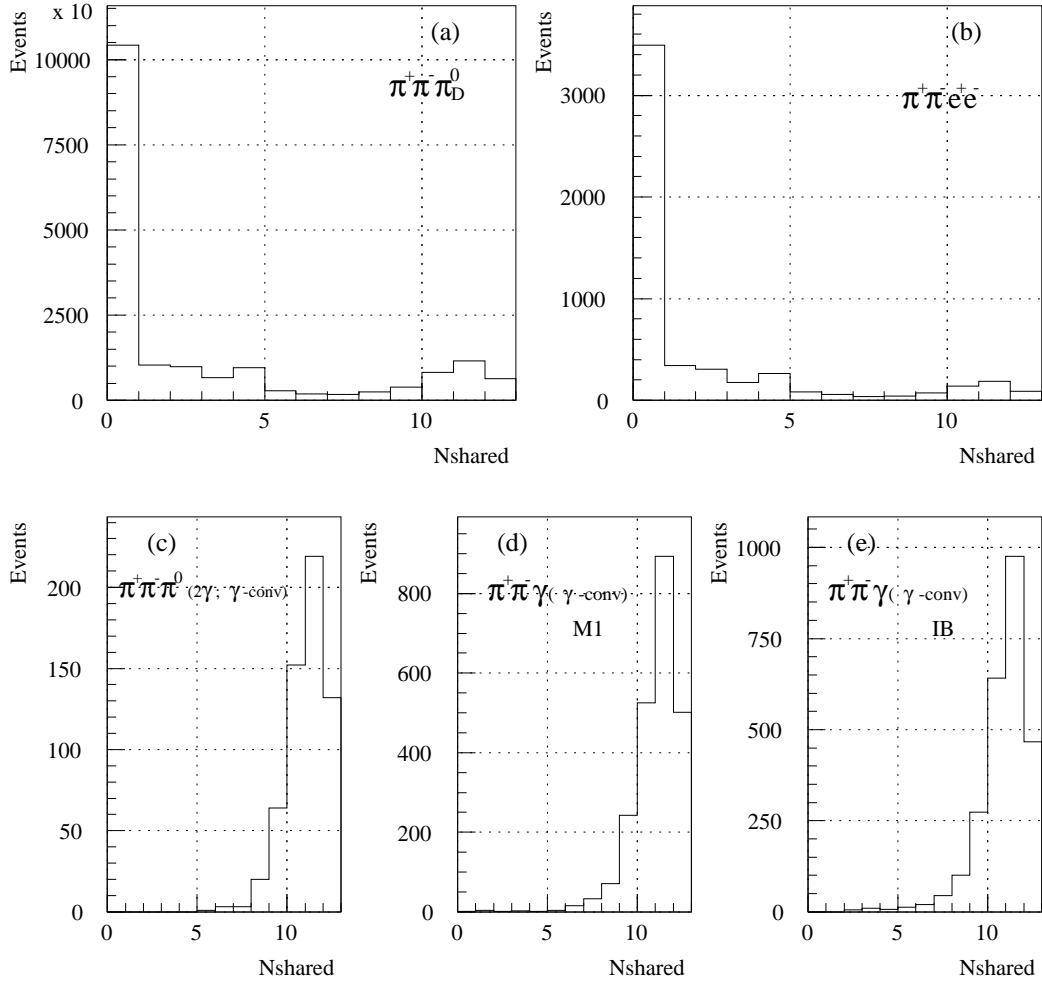


Figure 4.5: The N_{shared} distributions. The data sets (a) through (e) are same in Figure 4.4.

Before we describe the detail of this cut, we will show its usefulness in rejecting another class of backgrounds; these stemmed from the decay of pions. If one of the charged pions in $K_L \rightarrow \pi^+\pi^-\pi_D^0$ decayed into muons in flight, its momentum would be calculated incorrectly. Most of such π -decay events could be removed in the previous analysis stage, namely, the *DXMAG* cut and vertex χ^2 cut. However, when the decay happened to occur near the magnet center or right downstream of the K_L decay vertex, the event could satisfy the above cuts and would become serious backgrounds by making the $\pi^+\pi^-e^+e^-$ invariant mass large enough to be inside the signal box. It turns out that these events have a relatively large momentum asymmetry, and can be removed by the cut at least partially.

Figure 4.6 shows the A_{+-} distributions for the following data sets:

- (a) The Monte Carlo events ($K_L \rightarrow \pi^+\pi^-e^+e^-$),
- (b) The Monte Carlo events ($K_L \rightarrow \pi^+\pi^-\pi_D^0$),
- (c) The actual events ($M_{\pi\pi} > 370\text{MeV}/c^2$),
- (d) The subset of (b) with a π -decay and $M_{\pi\pi ee} \geq 480\text{ MeV}/c^2$.

In the actual analysis, we required pion candidates to satisfy $|A_{+-}| \leq 0.5$. This demand reduced efficiently the background events due to the nuclear interactions as well as the pion decay events in $K_L \rightarrow \pi^+\pi^-\pi_D^0$.

Based upon the Monte Carlo simulations, it was found that the efficiency of this cut was 89.2% for $K_L \rightarrow \pi^+\pi^-e^+e^-$ and 95.7% for $K_L \rightarrow \pi^+\pi^-\pi_D^0$.

4.2 Analysis of the Normalization mode $K_L \rightarrow \pi^+\pi^-\pi_D^0$

In this section, the analysis of the $K_L \rightarrow \pi^+\pi^-\pi_D^0$ mode will be presented. As mentioned before, it is very important to identify this mode and study its nature in this experiment. The reason is twofold. First of all, the mode is used as the normalization process, namely to calculate the incident K_L flux and to determine the detector efficiencies. It is particularly suited for this purpose since it has the same decay products as the signal mode, except for a photon. Thus we expect most of uncertainties to cancel out in calculating efficiencies of track reconstruction, particle identification and so on. We should also note that its branching ratio is large and well known. The second reason is that the mode is expected to become the main backgrounds to the signal mode. The advantages mentioned above become disadvantages in this respect. Thus, in any case, the study of this mode is of crucial importance.

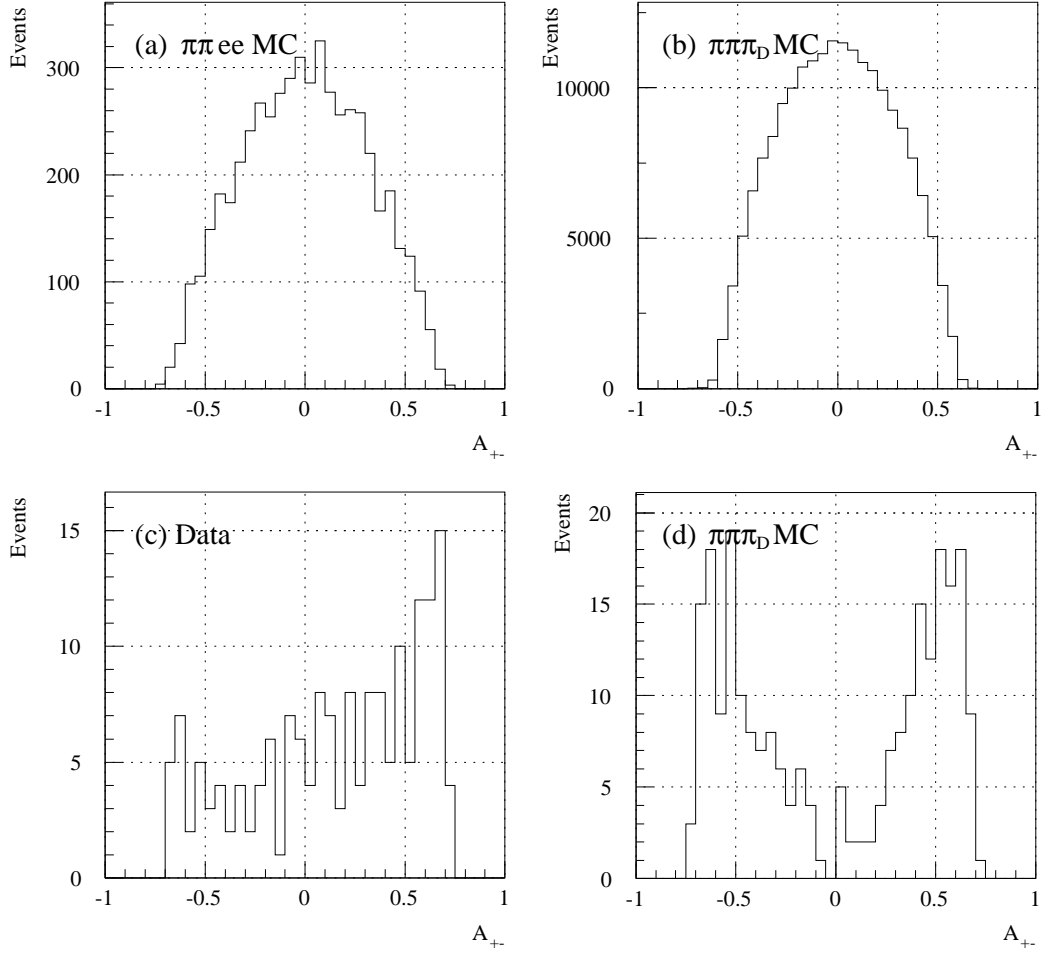


Figure 4.6: The A_{+-} distributions. (a) the $K_L \rightarrow \pi^+\pi^-e^+e^-$ MC, (b) the $K_L \rightarrow \pi^+\pi^-\pi_D^0$ MC, (c) the actual events with $M_{\pi\pi} > 370\text{MeV}/c^2$ (where the effect of $\pi^+\pi^-\pi_D^0$ events is small) and (d) the subset of (b) with a π -decay and $M_{\pi\pi ee} \geq 480\text{ MeV}/c^2$.

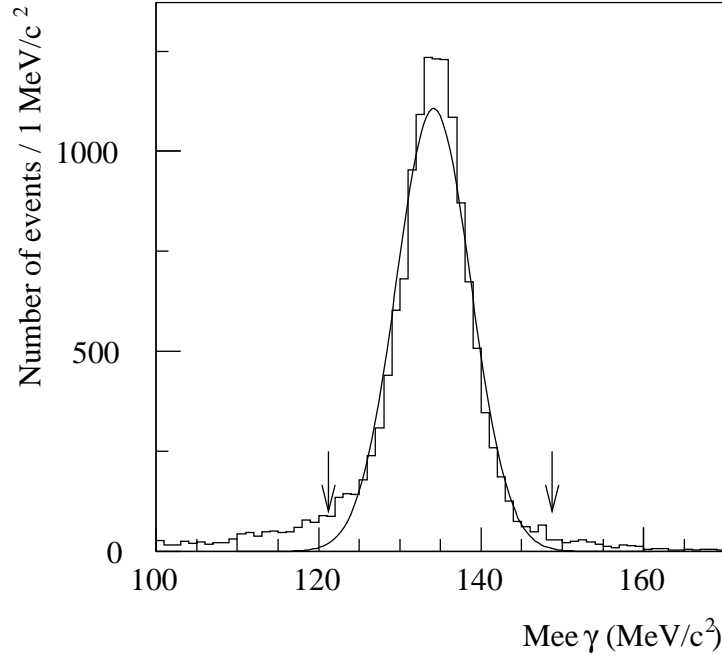


Figure 4.7: The distribution of $e^+e^-\gamma$ invariant mass for $K_L \rightarrow \pi^+\pi^-\pi_D^0$ candidates. The curve in the figure is a fit by the Gaussian form. The arrows indicates the cut values.

4.2.1 Reconstruction of $K_L \rightarrow \pi^+\pi^-\pi_D^0$

The reconstruction of $K_L \rightarrow \pi^+\pi^-\pi_D^0$ was started with “Candidate Sample” obtained in Section 4.1, i.e. those events that had π^+ , π^- , e^+ , and e^- with a common vertex in the decay region. We selected the events that contained at least one photon candidate(s), and then tried to reconstruct π^0 with e^+ and e^- . In case there were 2 or more photon candidates, we chose the one which had the $e^+e^-\gamma$ invariant mass ($M_{ee\gamma}$) closest to the π^0 mass (M_{π^0}). Figure 4.7 shows the resultant $M_{ee\gamma}$ distribution. The π^0 mass resolution σ_π was obtained by fitting the distribution to the Gaussian form and was found to be about $4.6 \text{ MeV}/c^2$. To identify the Dalitz decay, we requested $M_{ee\gamma}$ to be within $3\sigma_\pi$ ($= 13.8 \text{ MeV}/c^2$) of M_{π^0} . This cut was called the π^0 mass cut.

Next, we calculated the $\pi^+\pi^-e^+e^-\gamma$ invariant mass ($M_{\pi\pi ee\gamma}$). Figure 4.8 shows the $M_{\pi\pi ee\gamma}$ distribution after the π^0 mass cut. The mass resolution for K_L , denoted as σ_K , was obtained by fitting the distribution to the Gaussian form and was found to be about $5.5 \text{ MeV}/c^2$. $M_{\pi\pi ee\gamma}$ was also required to be within $3\sigma_K$ ($= 16.5 \text{ MeV}/c^2$) of the K_L mass (M_{K_L}). This requirement was called the K_L mass cut. The third requirement was related the $\pi^+\pi^-e^+e^-\gamma$

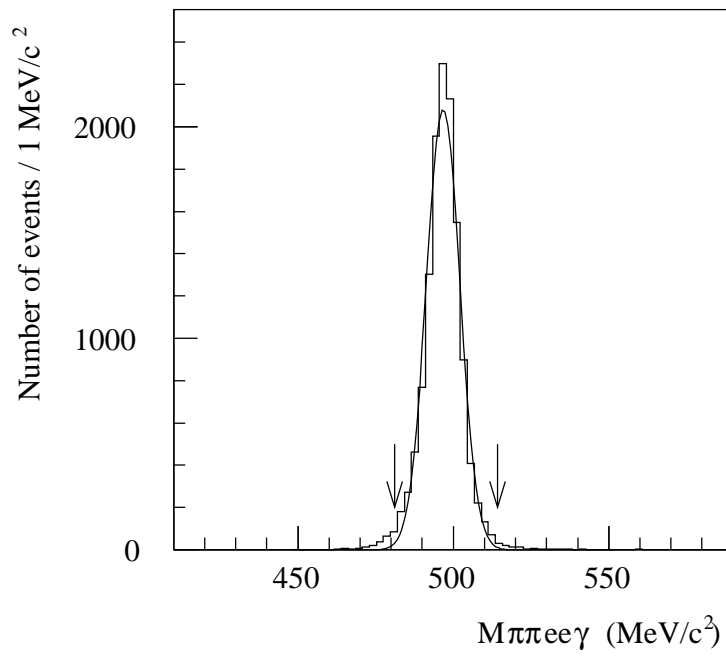


Figure 4.8: The distribution of $\pi^+\pi^-e^+e^-\gamma$ invariant mass for $K_L \rightarrow \pi^+\pi^-\pi_D^0$ candidates after the π^0 mass cut. The curve in the figure is a fit by the Gaussian form. The arrows indicates the cut values.

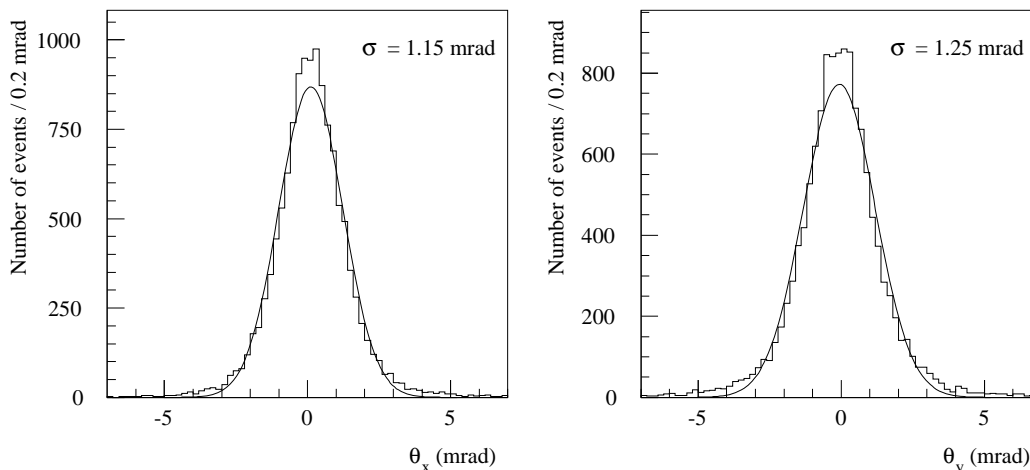


Figure 4.9: The distributions of (a) θ_x and (b) θ_y of $K_L \rightarrow \pi^+\pi^-\pi_D^0$ candidates. The curves in the figures are fits by Gaussian form.

reconstruction angle θ , the angle between the reconstructed momentum of the $\pi^+\pi^-e^+e^-\gamma$ system and the line connecting the target and decay vertex (see Section 4.1.2). In the actual analysis, we calculated two projection angles θ_x and θ_y , the angle θ projected onto the Z-X and Z-Y plane, respectively. Figure 4.9(a) and (b) show the resultant distributions of θ_x and θ_y . The distributions were fitted to the Gaussian form yielding their resolutions to be 1.15 mrad and 1.25 mrad, respectively. Approximating these widths to be equal, a distribution of $\theta^2 = \theta_x^2 + \theta_y^2$ becomes the χ^2 -distribution with two degree of freedom.³ Figure 4.10 shows the actual θ^2 distribution, in which the arrow represents a cut on θ^2 . The cut value, 20 mrad², was determined in such a way that the fraction of rejected events was equivalent to a standard 3σ cut.

Figure 4.11 shows the scatter plot of θ^2 vs $M_{\pi\pi ee\gamma}$ after the π^0 mass cut. The box in the figure, which represents the K_L mass cut and θ^2 cut, was defined as the signal region for $K_L \rightarrow \pi^+\pi^-\pi_D^0$. The events remained inside the signal region were identified as the $\pi^+\pi^-\pi_D^0$ events in this analysis. After all, we obtained 12212 of the reconstructed $\pi^+\pi^-\pi_D^0$ events, of which 2066 events in the Helium run, and 10146 events in the Vacuum run.

We now argue about possible background contamination into the $\pi^+\pi^-\pi_D^0$ signals. The main source came from the $K_L \rightarrow \pi^+\pi^-\pi^0$ mode, in which one of the two photons from π^0 converted into an e^+e^- pair externally (i.e. in the beam line materials). This process was studied by a Monte Carlo simulation

³It turns out this is a simple exponential function.

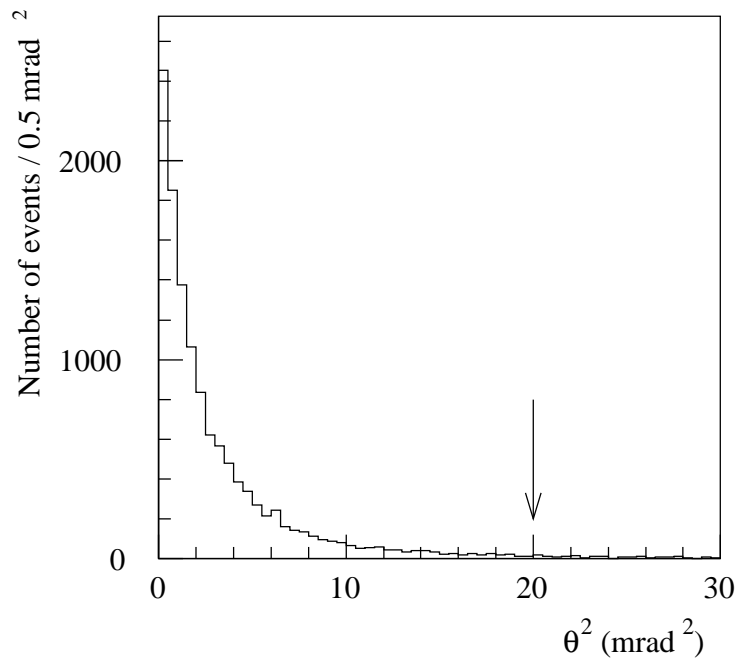


Figure 4.10: The θ^2 distribution $K_L \rightarrow \pi^+\pi^-\pi_D^0$ candidates after the π^0 and K_L mass cuts. The arrows indicates the cut value.

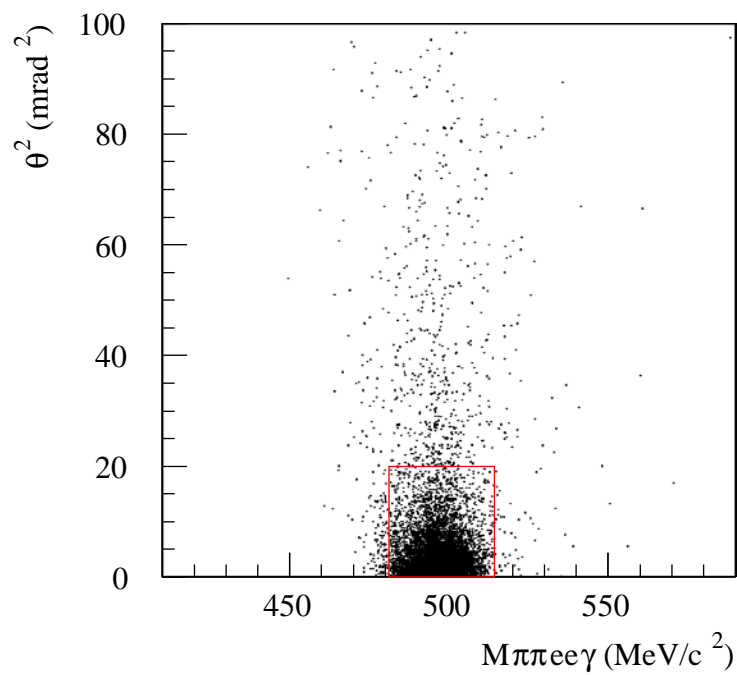


Figure 4.11: The scatter plot of θ^2 vs $M_{\pi\pi ee\gamma}$ after π^0 mass cut. The box indicates the M_{K_L} and θ^2 cut, i.e. the signal region for $K_L \rightarrow \pi^+\pi^-\pi_D^0$.

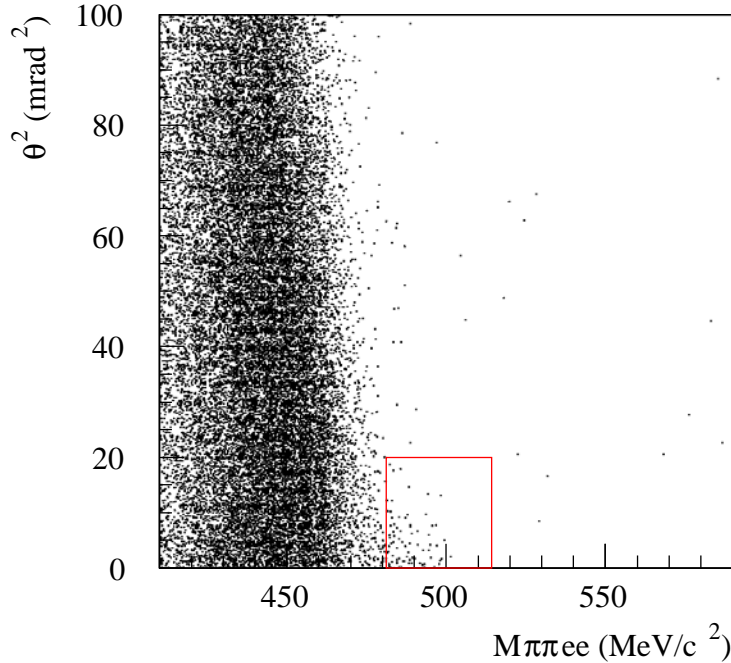


Figure 4.12: The scatter plot of θ^2 vs $M_{\pi\pi ee}$. The box indicates the signal region.

and was found to be less than 1% of the signal. Other contamination is negligibly small. The details of this estimation will be described in Section 4.5.2.

4.3 Analysis of the Signal mode $K_L \rightarrow \pi^+\pi^-e^+e^-$

In this section, we describe the analysis of the signal mode $K_L \rightarrow \pi^+\pi^-e^+e^-$. The analysis was started with the “Candidate Sample” obtained in Section 4.1, same as the normalization mode. The main task here was to select $K_L \rightarrow \pi^+\pi^-e^+e^-$ events from overwhelming background events. The nature of the task is illustrated in Figure 4.12, which shows the scatter plot of θ^2 vs $M_{\pi\pi ee}$ (of the $\pi^+\pi^-e^+e^-$ system). The signal region for $K_L \rightarrow \pi^+\pi^-e^+e^-$, indicated by the box in the figure, is defined in the same way as that for $K_L \rightarrow \pi^+\pi^-\pi_D^0$. The figure also displays sources of the backgrounds: they come from $K_L \rightarrow \pi^+\pi^-\pi_D^0$ decays since most of the events fell in the mass region below the K_L mass. In addition, there existed several events whose mass is larger than K_L . They were from nuclear interactions still remaining in the sample. In the following, we present the method to reject these backgrounds and identify the signals.

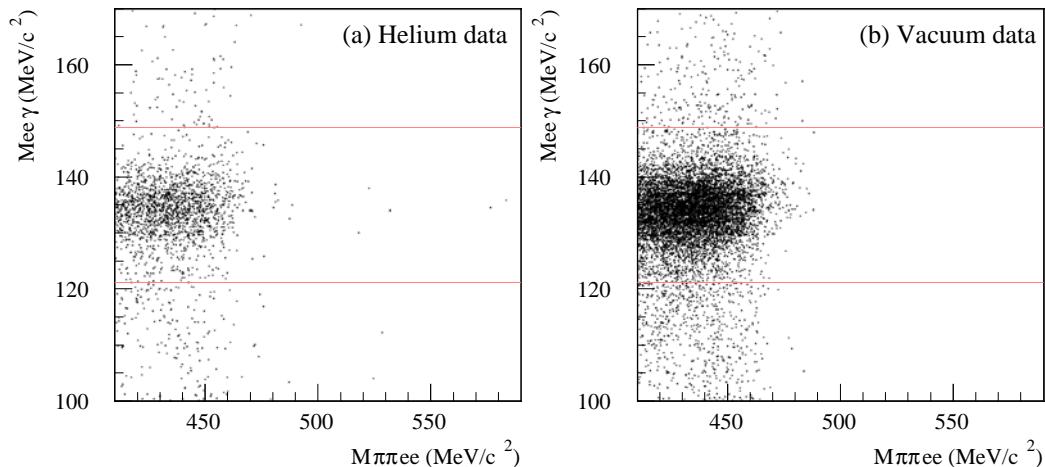


Figure 4.13: The scatter plot of $M_{ee\gamma}$ vs $M_{\pi\pi ee}$ obtained with the events that contain a photon(s). (a) the Helium data and (b) the vacuum data. The lines indicate the π^0 inclusive cut applied to the data.

4.3.1 π^0 Inclusive Cut

First, we deal with events which contain photon candidate(s). At first sight, we are tempted to remove all of them since our signal mode does not include photons. In reality, however, a simple “photon veto” is not possible because it leads to a huge sensitivity loss due to an accidental photon. In stead, we removed the events which contained the Dalitz decay, i.e. $\pi^0 \rightarrow e^+e^-\gamma$. This cut, called the π^0 inclusive cut, was effective to remove the $K_L \rightarrow \pi^+\pi^-\pi_D^0$ decays and/or the events originated from nuclear interactions. Figure 4.13(a) and (b) show the scatter plots of $M_{ee\gamma}$ vs $M_{\pi\pi ee}$ for the events that had photon candidate(s).⁴ The figures correspond to (a)the Helium data, and (b)the Vacuum data, respectively. There exists a clear cluster of events with $M_{ee\gamma} \simeq M_{\pi^0}$, forming a horizontal band. Most of them satisfy $M_{\pi\pi ee} < M_{K_L}$; their origin is obviously identified as $K_L \rightarrow \pi^+\pi^-\pi_D^0$. In addition, we observe several events, especially in the Helium data, located in the region above the K_L mass. Their origin is most likely nuclear interactions. We removed the events which satisfied the condition $|M_{ee\gamma} - M_{\pi^0}| < 3\sigma_\pi$.

This cut caused over-veto against the $K_L \rightarrow \pi^+\pi^-e^+e^-$ events when they had accidental photons. The over-veto probability was found to be about 1% and will be discussed in detail in Section 4.5.1.

⁴When plural photons existed in one event, the value closest to π^0 mass was employed as $M_{ee\gamma}$.

4.3.2 Backgrounds from $K_L \rightarrow \pi^+\pi^-\pi_D^0$ with missing γ

Now we are in a position to deal with the $K_L \rightarrow \pi^+\pi^-\pi_D^0$ decay in which the photon is escaped from detection by one reason or another. At first, we assumed existence of a photon, with an arbitrary momentum \vec{p}_γ , in every remaining event at this stage.

Then we defined the following quantity χ_D^2 :

$$\chi_D^2(\vec{p}_\gamma) \equiv \left(\frac{M_{ee\gamma} - M_{\pi^0}}{\sigma_{M_{\pi^0}}} \right)^2 + \left(\frac{M_{\pi\pi ee\gamma} - M_{K_L}}{\sigma_{M_{K_L}}} \right)^2 + \left(\frac{\theta_x}{\sigma_{\theta_x}} \right)^2 + \left(\frac{\theta_y}{\sigma_{\theta_y}} \right)^2. \quad (4.4)$$

In this expression, $\theta_x(\theta_y)$ denotes the $\pi^+\pi^-e^+e^-\gamma$ reconstruction angle⁵ projected onto the Z-X(Z-Y) plane. The denominator in each term is the corresponding resolution (see below for the actual values). This χ_D^2 expresses likelihood of an event being originated from $K_L \rightarrow \pi^+\pi^-\pi_D^0$. In another words, with an appropriate \vec{p}_γ value, $\chi_D^2(\vec{p}_\gamma)$ becomes very small for $K_L \rightarrow \pi^+\pi^-\pi_D^0$, but in general it remains large for $K_L \rightarrow \pi^+\pi^-e^+e^-$. We thus minimized $\chi_D^2(\vec{p}_\gamma)$ by varying \vec{p}_γ . (From now on, we denote the minimized $\chi_D^2(\vec{p}_\gamma)$ by χ_D^2 .) In Equation (4.4), we adopted the resolutions determined from the reconstructed $K_L \rightarrow \pi^+\pi^-\pi_D^0$ events. The actual values are:

$$\begin{aligned} \sigma_{M_{\pi^0}} &= 4.6 \text{ MeV}/c^2, \\ \sigma_{M_{K_L}} &= 5.5 \text{ MeV}/c^2, \\ \sigma_{\theta_x} \simeq \sigma_{\theta_y} &= 1.2 \text{ mrad} \end{aligned} \quad (4.5)$$

(see Section 4.2.1).

Before we set a cut value on χ_D^2 , we first examine effectiveness of this method in more detail. To this end, we compared the experimental χ_D^2 distribution with Monte Carlo simulations. At first, we calculated χ_D^2 's of the reconstructed $K_L \rightarrow \pi^+\pi^-\pi_D^0$ events without using its observed photons. Figure 4.14 shows the resultant χ_D^2 distribution together with the Monte Carlo data. They agree well with each other. Next, we compared the χ_D^2 distribution of all the events with the corresponding $K_L \rightarrow \pi^+\pi^-\pi_D^0$ Monte Carlo simulation. Note that there is no π_D^0 ($e^+e^-\gamma$ whose invariant mass is M_{π^0}) in this event sample (due to the π^0 inclusive cut). As shown in Figure 4.15, they both show a peak at $\chi_D^2 \simeq 0$ and agree well with each other. It proves that most of the experimental events originated from $K_L \rightarrow \pi^+\pi^-\pi_D^0$, as expected.

Finally we studied a restricted set of the events which satisfied the kinematical constraints having important implication to the signals; specifically

⁵Note that the decay products were assumed to contain a photon with \vec{p}_γ .

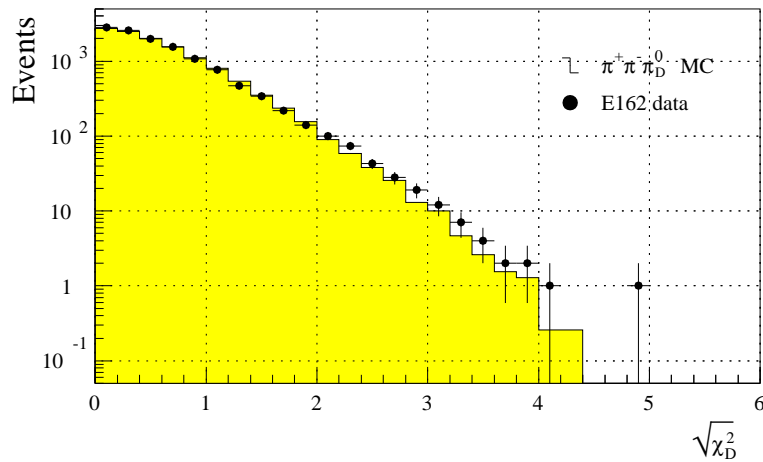


Figure 4.14: The minimized χ_D^2 distributions of the reconstructed $\pi^+\pi^-\pi_D^0$ events, together with the corresponding Monte Carlo simulation normalized with K_L -flux. Note that the horizontal axis $\sqrt{\chi_D^2}$.

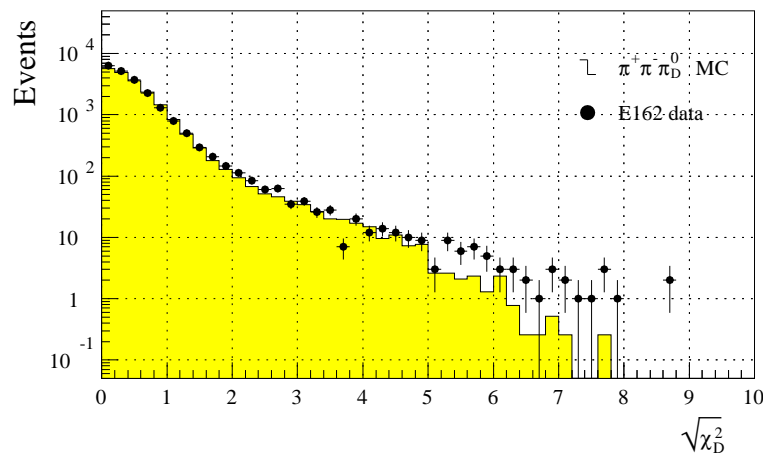


Figure 4.15: The $\sqrt{\chi_D^2}$ distribution of all events remaining at this stage, together with the corresponding $K_L \rightarrow \pi^+\pi^-\pi_D^0$ Monte Carlo simulation normalized with K_L -flux.

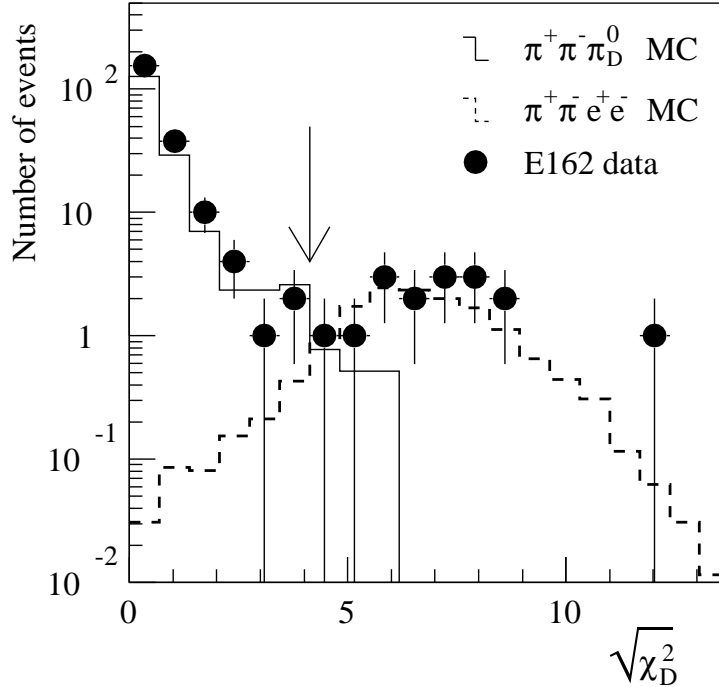


Figure 4.16: The $\sqrt{\chi_D^2}$ distributions. Shown are the actual data (Solid dots), the $\pi^+\pi^-e^+e^-$ Monte Carlo simulation (solid histogram) and the $\pi^+\pi^-\pi_D^0$ Monte Carlo simulation (dashed histogram). The K_L flux in the simulation was normalized with the reconstructed $\pi^+\pi^-\pi_D^0$ events, and the branching ratio for $\pi^+\pi^-e^+e^-$ was assumed to be obtained by our final result. The arrow indicates the cut value ($\chi_D^2 = 17$).

the constraints were $|M_{\pi\pi ee} - M_{K_L}| < 5\sigma_K (= 27.5 \text{ MeV}/c^2)$ and $\theta^2 \leq 20 \text{ mrad}^2$. The resultant χ_D^2 distribution is shown by the solid circle in Figure 4.16. We notice that the distribution has two components; a large peak at $\sqrt{\chi_D^2} \simeq 0$ and a small and broad peak at $\sqrt{\chi_D^2} \simeq 7$. The solid histogram is a Monte Carlo simulation for $K_L \rightarrow \pi^+\pi^-\pi_D^0$. The K_L flux in the simulation is normalized with the reconstructed $\pi^+\pi^-\pi_D^0$ events. The histogram (the shape and magnitude) represents the main part of the data very well. The dashed histogram is a Monte Carlo simulation for $K_L \rightarrow \pi^+\pi^-e^+e^-$. Its branching ratio is assumed to be given by our final result (see Section 4.4). We observe that the broad peak can be explained very well by the $K_L \rightarrow \pi^+\pi^-e^+e^-$ simulation. We removed the events with $\chi_D^2 < 17$ as being consistent with $K_L \rightarrow \pi^+\pi^-\pi_D^0$. Examining the Monte Carlo simulations, this cut was found to remove 99.7% of $K_L \rightarrow \pi^+\pi^-\pi_D^0$ events with the efficiency of 92% for

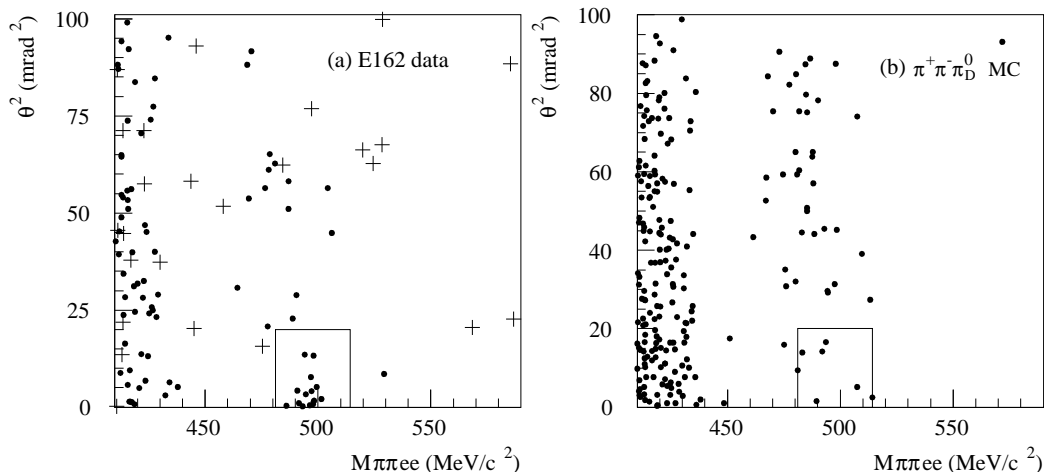


Figure 4.17: (a) The θ^2 vs $M_{\pi\pi ee}$ scatter plot of the $K_L \rightarrow \pi^+\pi^-e^+e^-$ candidate events after the χ_D^2 cut. The solid dots represent the Vacuum data and the plus the Helium data. The box indicates the signal region. (b) The corresponding scatter plot obtained by the $\pi^+\pi^-\pi_D^0$ MC simulation. Note that the MC statistics is 5 times more than the Vacuum data.

$K_L \rightarrow \pi^+\pi^-e^+e^-$. The arrow in the figure indicates our cut value on χ_D^2 . It is evident from the plot that the χ_D^2 cut effectively separated the signal from the overwhelming backgrounds.

4.3.3 Signal Identification and Background Subtraction

Figure 4.17(a) shows the scatter plot of θ^2 vs $M_{\pi\pi ee}$ after the χ_D^2 cut. The solid dots represent data from the Vacuum run, while the pluses represent data from the Helium run. The final conditions are

$$\begin{aligned} |M_{\pi\pi ee} - M_{K_L}| &< 16.5 \text{ MeV}/c^2 \quad (3\sigma_K) \\ \theta^2 &< 20 \text{ mrad}^2 \end{aligned} \quad (4.6)$$

for the events to be identified as the $K_L \rightarrow \pi^+\pi^-e^+e^-$ decay. The cuts are the same as those for $K_L \rightarrow \pi^+\pi^-\pi_D^0$, and are indicated by the box in Figure 4.17(a). Figure 4.17(b) shows a corresponding scatter plot for the $\pi^+\pi^-\pi_D^0$ Monte Carlo simulation. Note that the Monte Carlo statistics is 5 times more than the Vacuum data. We can observe clearly a cluster of events in the signal region in the experimental data, but not in the $\pi^+\pi^-\pi_D^0$ Monte Carlo simulation. We also notice that there are non-negligible backgrounds.

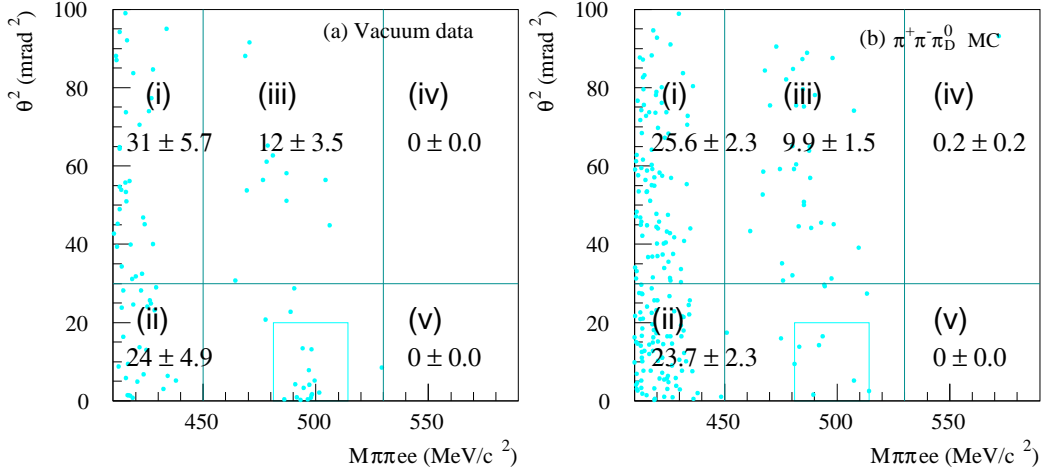


Figure 4.18: The number of background events in each region from (i) to (v). (a) the Vacuum data and (b) $\pi^+\pi^-\pi_D^0$ Monte Carlo simulation normalized with the reconstructed $\pi^+\pi^-\pi_D^0$.

For the Vacuum data, they consist of two distinct bands uniformly distributed along the θ^2 -axis, which are reproduced qualitatively well by the $\pi^+\pi^-\pi_D^0$ simulation.

To study the background quantitatively, we divided the $M_{\pi\pi ee}-\theta^2$ plane into several regions, and compared the data and simulation in each region individually. Figure 4.18 shows the number of events in the regions from (i) to (v) for (a) the vacuum data and (b) the $\pi^+\pi^-\pi_D^0$ Monte Carlo simulation whose K_L flux was normalized with the reconstructed $\pi^+\pi^-\pi_D^0$. It indicates that for the vacuum data, the background events were understood quantitatively, and they were well explained by the $\pi^+\pi^-\pi_D^0$ Monte Carlo simulation. From studying the Monte Carlo events, it was found that there existed two mechanisms for the $\pi^+\pi^-\pi_D^0$ events to pass through the χ_D^2 cut. One is γ -radiation: events in which e^+/e^- radiates γ -rays internally or externally would lose its energy. The backgrounds remaining in the region (i) and (ii) correspond to this γ -radiation type. The other is π -decay: events in which π^+/π^- decays at the center of magnet or just downstream of the K_L decay vertex would have wrong momentum assignment. The backgrounds remaining in the region (iii) correspond to this π -decay type.

In the Helium data, however, there are a certain number of events unexplainable by the $\pi^+\pi^-\pi_D^0$ simulation, especially in the high mass region. They were most likely originated from nuclear interactions, since the Helium run was different from the Vacuum run only in the decay volume materials.

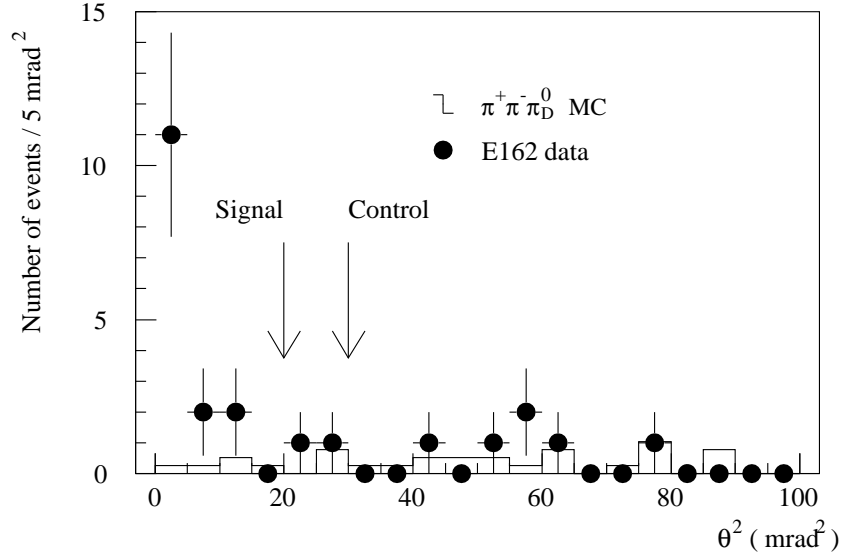


Figure 4.19: The θ^2 projection of the $K_L \rightarrow \pi^+ \pi^- e^+ e^-$ candidate events with $|M_{\pi\pi ee} - M_{K_L}| < 3\sigma_K$. The solid line in the figure represents the $\pi^+ \pi^- \pi_D^0$ MC simulation. The K_L flux was normalized with the number of reconstructed events as $\pi^+ \pi^- \pi_D^0$. The arrow indicate the signal and control region boundaries.

Thus, we concluded that the $\pi^+ \pi^- \pi_D^0$ decay and nuclear interactions events to be the main background source for $\pi^+ \pi^- e^+ e^-$.

Background subtraction

We now want to estimate the number of background events inside the signal region. The background events from $\pi^+ \pi^- \pi_D^0$ have no distinct structure along the θ^2 -axis as shown in Figure 4.17(a) and (b). We expect that the nuclear interaction events distribute themselves also uniformly along the θ^2 -axis, because they loose memories of the angle θ with many unobserved reaction products. Therefore, we projected the events with $|M_{\pi\pi ee} - M_{K_L}| < 3\sigma_{M_{K_L}}$ onto the θ^2 -axis. Figure 4.19 shows the projection result. The dots represents the experimental data, and the solid line represents $\pi^+ \pi^- \pi_D^0$ Monte Carlo simulation. The K_L flux in the simulation was normalized with the reconstructed $\pi^+ \pi^- \pi_D^0$ events. A clear peak can be observed at $\theta^2 = 0$ only in the experimental data; the $\pi^+ \pi^- \pi_D^0$ Monte Carlo simulation shows a flat distribution along the θ^2 -axis.

We defined the “control” region with $30 \text{ mrad}^2 < \theta^2 < 100 \text{ mrad}^2$. The

signal region correspond to $\theta^2 < 20 \text{ mrad}^2$ in this plot. For the Vacuum data, we observed 4 events in the control region, and 15 events in the signal region. For the Helium data, we observed 2 events in the control region, while no events in the signal region. In the $\pi^+\pi^-\pi_D^0$ Monte Carlo simulation, we observed 5.2 events in the control region, and 1.3 events in the signal region. We assumed that the shape of the background distribution is given by the $\pi^+\pi^-\pi_D^0$ Monte Carlo simulation. This assumption can be justified by quantitative as well as qualitative agreement between the experimental data and the simulation in the control region. We then renormalized the $\pi^+\pi^-\pi_D^0$ simulation in such a way that the number of events in the control region agreed with that of the experimental data. This “renormalization” procedure was to take into account the contribution from the nuclear interaction and other unknown background source(s). We stress that the backgrounds from nuclear interaction are seen mainly in the Helium data, and the amount of the Helium data is much less than that of Vacuum. This fact, together with the flat distribution along θ^2 direction, justifies the treatment above.

From the procedure described above, we estimated the number of backgrounds inside the signal region events to be 1.5. By subtraction out the backgrounds statistically we determined the number of signal events to be 13.5 ± 4.0 , where the error represents the data and Monte Carlo statistics.

4.4 Calculation of the Branching Ratio

The branching ratio is expressed by

$$Br(K_L \rightarrow \pi^+\pi^-e^+e^-) = \frac{N(\pi^+\pi^-e^+e^-)}{A(\pi^+\pi^-e^+e^-) \cdot \eta(\pi^+\pi^-e^+e^-)} \cdot \frac{1}{F(K_L)}, \quad (4.7)$$

where A , η , N and F denote the acceptance, efficiency, number of observed events, and the incident K_L flux, respectively. We can write down a similar expression for $K_L \rightarrow \pi^+\pi^-\pi_D^0$. Since we know the branching ratio for $K_L \rightarrow \pi^+\pi^-\pi_D^0$, we can, in principle, calculate the K_L flux F . In practice, however, we take the ratio of the two to obtain

$$\begin{aligned} Br(K_L \rightarrow \pi^+\pi^-e^+e^-) &= Br(K_L \rightarrow \pi^+\pi^-\pi_D^0) \times Br(\pi^0 \rightarrow e^+e^-\gamma) \\ &\times \frac{A(\pi^+\pi^-\pi_D^0)}{A(\pi^+\pi^-e^+e^-)} \cdot \frac{\eta(\pi^+\pi^-\pi_D^0)}{\eta(\pi^+\pi^-e^+e^-)} \cdot \frac{N(\pi^+\pi^-e^+e^-)}{N(\pi^+\pi^-\pi_D^0)}. \end{aligned} \quad (4.8)$$

This expression is superior because most of uncertainties would cancel out in the ratio. In Equation (4.8), division between the acceptance and efficiency is somewhat arbitrary; in this analysis, we define the acceptance by the geometrical one plus hardware trigger (Level 1 and Level 2) efficiencies. On

the other hand, efficiencies of the detector and/or the cuts employed in the analysis procedure, are classified as the efficiency. The acceptances and efficiencies were determined relying heavily on Monte Carlo simulations as well as various detector efficiencies determined experimentally. Before we present the detailed procedure of their determination, we show the summaries in Table 4.1 through Table 4.3. In each table, the 3rd column labeled as “ratio” is a quantity for the normalization mode (1st column) divided by the corresponding one for the signal mode (2nd column).

Table 4.1: Number of events (N)

	$\pi^+\pi^-\pi_D^0$	$\pi^+\pi^-e^+e^-$	ratio
Signal with error	12212 ± 110	13.5 ± 4.0	905 ± 268

Table 4.2: Detector acceptance (A)

		$\pi^+\pi^-\pi_D^0$	$\pi^+\pi^-e^+e^-$	ratio
geometrical ^a		2.24×10^{-3}	5.25×10^{-3}	0.427
Trigger level 1	$N(\text{TC23}) \geq 3$	0.976	0.975	1.001
	$N(\text{TC1X}) \geq 2^b$	0.930	0.963	0.966
	$N(\text{TC2Y}) \geq 2^b$	0.999	0.998	1.001
	$N(\text{GC}) \geq 2$	0.916	0.886	1.034
	$N(\text{TC0X}) \geq 3$	0.704	0.842	0.836
	$N(\text{CSIX}) \geq 2^b$	0.935	0.854	1.095
	$N(\text{CSIY}) \geq 2^b$	0.969	0.946	1.024
	Total	0.530	0.564	0.940
Trig.Level 2		0.823	0.890	0.925
Total		9.77×10^{-4}	2.64×10^{-3}	0.370

^a All of decay products into the calorimeter.

^b At least 1 in each arm.

Detector Acceptance

The detector acceptance is divided into a geometrical acceptance and level 1 and level 2 trigger efficiencies. The geometrical acceptance is defined as

Table 4.3: Analysis efficiencies (η)

		$\pi^+\pi^-\pi_D^0$	$\pi^+\pi^-e^+e^-$	ratio
General event selection	Track finding (≥ 4)	0.587	0.627	0.936
	Matched track (=4)	0.482	0.526	0.916
	$\pi^+\pi^-e^+e^-$ Topology	0.951	0.947	1.005
	Vertex cut ^a	0.666	0.683	0.975
	γ finding	0.924	—	0.924
	Total	0.193	0.242	0.799
Kinematical event selection	Loose Kinematical cut	0.987	0.991	0.997
	M_{ee} cut ^b	0.780	0.856	0.911
	$ A_{+-} < 0.5$	0.957	0.892	1.073
	π^0 mass cut	0.944	—	0.944
	$\chi_D^2 \geq 17$	—	0.915	1.094
	K_L mass, θ^2 cut	0.961	0.949	1.013
	Total	0.669	0.657	1.018
Accidental activity (π^0 inclusive cut)		0.409	0.455 (0.989)	0.899 (1.011)
Total		0.0529	0.0723	0.731

^a Cuts for vertex χ^2 and vertex position.^b Cuts for M_{ee} and N_{shared} .

the probability that all decay products are accepted into the calorimeter.⁶ This was determined by a Monte Carlo simulation, and was found to be $2.24 \times 10^{-3}/5.25 \times 10^{-3} = 0.427$. From now on, we use the convention,

$$(\text{quantity for } \pi^+\pi^-\pi_D^0)/(\text{corresponding one for } \pi^+\pi^-e^+e^-) = \text{ratio}$$

to simplify the notation. The level 1 trigger efficiency consisted of geometrical acceptance of various trigger counters and efficiencies of the trigger logic requirements. It was found to be $0.530/0.564 = 0.940$. Finally, the level 2 trigger efficiency was determined to be $0.823/0.890 = 0.925$. Combining these three factors together, the overall detector acceptance was $(9.77 \times 10^{-4})/(2.64 \times 10^{-4}) = 0.370$. The main difference between the two modes stemmed from the geometrical acceptance; the $\pi^+\pi^-\pi_D^0$ mode, which had an extra γ -ray, was smaller than $\pi^+\pi^-e^+e^-$.

Analysis efficiency

As to the analysis efficiencies, most of them were common to both signal and normalization modes and they tended to cancel out in the ratio. The total efficiency of analysis was found to be $5.29\%/7.23\% = 0.731$ (see the bottom row in Table 4.3). Below we will describe some notable features in Table 4.3.

The differences in efficiencies between the two modes were mainly due to the existence of an extra photon in $\pi^+\pi^-\pi_D^0$. In Table 4.3, items labeled as “Matched Track (= 4)”, “ γ finding” and “ π^0 mass cut” were influenced by the photon. Of these, the first one, “Matched Track”, demands some explanation: if the photon was close to other decay products on the calorimeter, clusters began to overlap each other. This in turn affected the energy and/or position measurements, resulting in the efficiency loss in the track matching. Multiplying these three effects together, we found the effect of the extra photon to be $0.420/0.526 = 0.798$.

The next largest differences were caused by the kinematical cuts related to M_{ee} and A_{+-} . The efficiency due to the M_{ee} cut was $0.789/0.856 = 0.911$, while that of A_{+-} was $0.957/0.892 = 1.073$. The χ_D^2 cut was applied only to the signal mode: its efficiency was $1.0/0.915 = 1.094$. We found that the other effects caused smaller difference in the efficiency ratio.

Extra hit(s) in our detector by an accidental coincidence with real events of $\pi^+\pi^-\pi_D^0$ and/or $\pi^+\pi^-e^+e^-$ might cause inefficiency in the event recon-

⁶We allow the case that a pion decays into a muon in flight and the muon is accepted into the calorimeter, since it is not discriminated from a pion in our detector system and analysis. For a similar reason, the case that a photon converts into an e^+/e^- pair downstream of the analyzing magnet and they are accepted into the calorimeter, is also allowed in the case of $K_L \rightarrow \pi^+\pi^-\pi_D^0$ mode.

struction procedure. To estimate the effect of accidental activities, we used Monte Carlo events overlaid by “noise” events which were obtained experimentally by a random trigger (Trig.4). The detail of this estimation will be described in Section 4.5.1. Here we quote its final result; it was found to be $0.409/0.455 = 0.899$. As expected, degree of accidental activities varied with the K_L beam intensity: the values quoted above were those correspond to the average intensity. The systematic error associated with them will be also examined in Section 4.5.1.

We finally comment on the over-veto probability of the π^0 inclusive cut. This effect has been already included in the simulation of the accidental activity. We list it in the parenthesis to see its effect separately; it was found to be $1.0/0.989 = 1.011$.

Final Branching Ratio

We have now determined all necessary ratios to calculate the branching ratio;

$$\begin{aligned} A(\pi^+\pi^-\pi_D^0) / A(\pi^+\pi^-e^+e^-) &= 0.37 \\ \eta(\pi^+\pi^-\pi_D^0) / \eta(\pi^+\pi^-e^+e^-) &= 0.73 \\ N(\pi^+\pi^-e^+e^-) / N(\pi^+\pi^-\pi_D^0) &= 13.5/12212 . \end{aligned}$$

Using the known branching ratio of $Br(K_L \rightarrow \pi^+\pi^-\pi^0) = 0.13$ and $Br(\pi^0 \rightarrow e^+e^-\gamma) = 1.2 \times 10^{-2}$ [29], we finally arrived at

$$Br(K_L \rightarrow \pi^+\pi^-e^+e^-) = (4.4 \pm 1.3) \times 10^{-7} ,$$

where the error represents the statistical uncertainty.

4.5 Discussions on Systematic Error

In calculating the final branching ratio, we have only considered statistical uncertainty. In addition, there exist some uncertainties in estimating quantities in Equation (4.8). These are treated as systematic errors. For convenience, we divide them into 4 categories; those related to (i) the acceptance, (ii) the efficiency, (iii) the number of the events and (iv) the branching ratios $Br(K_L \rightarrow \pi^+\pi^-\pi^0)$ and $Br(\pi^0 \rightarrow e^+e^-\gamma)$. Several comments are in order here. First, division between the first two categories is artificial, but is useful for clear and easy understandings. Second, we will quote the systematic error in %; this means the error under consideration can change the final result in that fraction. As will be shown below, the systematic error amounts to be 11.3% in total; this value should be compared with the statistical error of $\sim 30\%$. Below, we will describe each category in the order listed above.

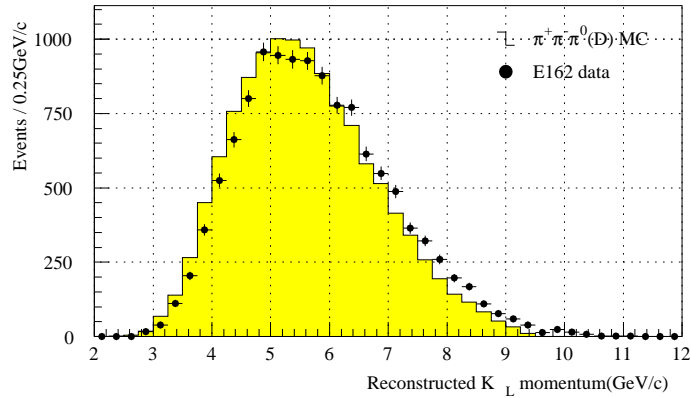


Figure 4.20: The K_L momentum distributions obtained with reconstructed $\pi^+\pi^-\pi_D^0$ events. The dots are the experimental data, and the histogram is the Monte Carlo simulation.

4.5.1 Acceptance-efficiency Calculations

As mentioned, we used a Monte Carlo simulation to calculate the acceptance. Various data were used as an input to the simulation. Although the input data were very accurate, they still had some uncertainties, which resulted in the error in the final branching ratio.

K_L momentum spectrum uncertainty

Calculation of the detector acceptance depends upon the parent spectrum (i.e. the K_L momentum at the production target) used as an input to the Monte Carlo simulation.⁷ A change in the spectrum results in a change in the acceptance ratio of the two modes and hence the branching ratio.

We constructed a model of the parent spectrum, and examined it by comparing various experimental distributions with predicted ones. These include the K_L momentum spectra measured via the $K_L \rightarrow \pi^+\pi^-\pi^0$ ($\pi^0 \rightarrow 2\gamma$) and/or $K_L \rightarrow \pi^+\pi^-\pi_D^0$ modes, the vertex Z-position distributions observed by $K_L \rightarrow \pi^+\pi^-\pi^0$ and/or $K_L \rightarrow \pi^+\pi^-\pi_D^0$, and so on. Although we tuned various parameters, we could not find the “perfect” parent spectrum. Thus there remained some discrepancy between the observed and predicted K_L momentum spectrum, as shown in Figure 4.20. We recalculated the acceptance using a “corrected” parent spectrum which could reproduce the observed one

⁷To some extent, this also applies to the analysis efficiency. Thus we actually checked the product of the acceptance and efficiency. However, to present a clear discussion, we simply call it the acceptance instead of the acceptance-efficiency product.

in Fig.4.20. The difference in acceptance occurred with the recalculation was treated as an systematic error. In terms of the final branching ratio, the error was 4.8% and was the largest contribution in this category.

Matrix element of theoretical model

We need the matrix elements of both $K_L \rightarrow \pi^+\pi^-e^+e^-$ and $K_L \rightarrow \pi^+\pi^-\pi_D^0$ modes to calculate the acceptance. This is because they determine the spatial and momentum distributions of the decay products, which in turn affect the acceptance. We used a theoretical mode [10] for $K_L \rightarrow \pi^+\pi^-e^+e^-$. However, this involves several coupling constants determined experimentally with some errors. Among them, the parameter called g_{M1} is found to influence the acceptance most. This parameter, determined by the branching ratio measurement of the direct emission component in $K_L \rightarrow \pi^+\pi^-\gamma$, has an experimental error of 2%. We altered it from its nominal value by $\pm 3\sigma$. It change the acceptance, and hence the final result, by 3.8%.

The matrix element for the $K_L \rightarrow \pi^+\pi^-\pi^0$ is characterized by the parameters called Dalitz plot parameters. They were determined experimentally and had some errors. We also altered these values by $\pm 3\sigma$, and found the change in the acceptance and efficiency to be less than 1%.

Summing up in quadrature, we concluded the effect of uncertainties in the matrix elements to be 3.9% in total. This is the second largest error in this category.

Distribution of z Decay Vertex

The acceptance and, to some extent, efficiency depend upon the decay Z-position. Figure 4.21(a) shows the ratio of $A \cdot \eta$ as a function of Z. Figure 4.21(b) shows the Z-vertex distribution of the reconstructed $K_L \rightarrow \pi^+\pi^-\pi_D^0$ events obtained with the experimental (solid dots) and Monte Carlo (hatched histogram) data. Unfortunately, there is some discrepancy between the two; it might come, for example, from an local efficiency drop in the beam region of the counters and chambers. Fortunately, this discrepancy makes very little effect in the final result thanks to the uniform $A \cdot \eta$ ratio shown in Fig.4.21(b). Adopting the Z-vertex distribution given by the experimental data instead of that by the simulation data, we calculated its actual effect numerically. We found it to be 1.2% in the final branching ratio, and regarded this to be a systematic error.

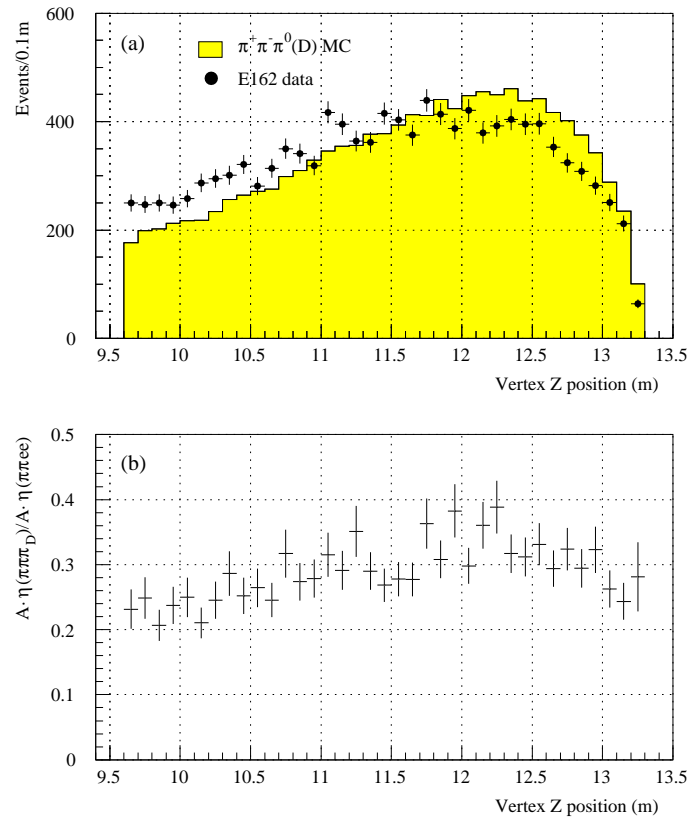


Figure 4.21: (a) The Z vertex distributions obtained with the reconstructed $K_L \rightarrow \pi^+ \pi^- \pi^0_D$ events. The dots are the experimental data, and the solid histogram is the Monte Carlo simulation. (b) The $A \cdot \eta$ ratio of the normalization to signal mode.

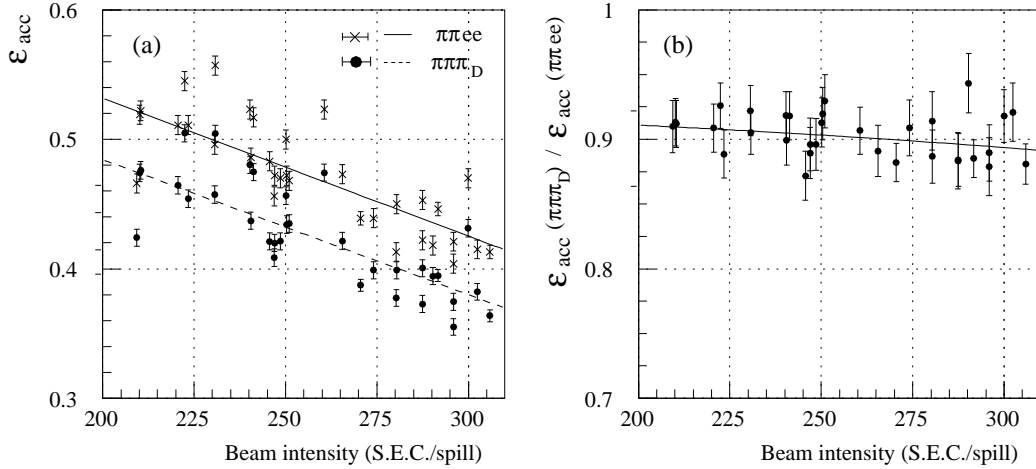


Figure 4.22: (a) The ratio of reconstruction efficiencies with to without overlaid Trig.4 data (ϵ_{acc}). The horizontal axis represents intensity of Trig.4 data expressed by S.E.C./spill. The dots represent $\pi^+\pi^-e^+e^-$, and the circles represent $\pi^+\pi^-\pi_D^0$. The line in the figure was obtained by the linear fit. (b) The ratio of efficiency. The curve in the figure is the ratio of the two fitted lines in (a).

Accidental Activity

To estimate influence of accidental activities, we used the data obtained by a random trigger (Trig.4). These Trig.4 events should simulate accidental activities. We amalgamated these events with the Monte Carlo events that were successfully reconstructed as $K_L \rightarrow \pi^+\pi^-e^+e^-$ and/or $K_L \rightarrow \pi^+\pi^-\pi_D^0$. We then analyzed them again to see the effect of amalgamation, or equivalently the accidental activities.

The result of this attempt is shown in Figure 4.22(a). In the figure, the horizontal axis shows the beam intensity in which the Trig.4 data was taken; it is expressed in units of the S.E.C. beam monitor.⁸ The vertical axis shows the quantity called efficiency ratio. It is defined by

$$\epsilon_{\text{acc}} = \frac{\eta(\text{Test events with Trig.4})}{\eta(\text{Test events without Trig.4})},$$

where η represents the reconstruction efficiency for the event sample in the parenthesis. The solid circle and cross points, respectively, represent the

⁸A proton beam intensity monitor by output from a secondary emission chamber placed upstream the production target.

efficiency ratio for the $K_L \rightarrow \pi^+\pi^-e^+e^-$ and $K_L \rightarrow \pi^+\pi^-\pi_D^0$ modes. The error bars are statistical ones. We observe the efficiency ratio to decrease with the beam intensity. The straight lines in Fig.4.22(a) are the linear fit to the data points.

In Fig.4.22(b), we plot the ratios of the efficiency ratio for the two modes; $\varepsilon_{\text{acc}}(K_L \rightarrow \pi^+\pi^-\pi_D^0)/\varepsilon_{\text{acc}}(K_L \rightarrow \pi^+\pi^-e^+e^-)$. The gentle curve in the figure is the ratio of the two fitted lines in Fig.4.22(a). The typical beam intensity was 272 in S.E.C./spill during the data taking, and more than 90% of the data was taken in the region from 220 to 310 S.E.C./spill. The efficiency ratio necessary to calculate the final branching ratio (see Eq.(4.8)) was affected by accidental activities; however, as can be seen from Fig.4.22(b), its dependence on the beam intensity was very weak. We considered the efficiency at 272 S.E.C./spill as nominal, and defined its dispersion associated with the dispersion in the beam intensity as a systematic error.

In summary, we obtained 0.455 and 0.409 as the efficiencies by accidental activities of the signal and normalization modes, respectively. And we found the systematic error in the final branching ratio to be 1.9%.

Over-veto probability by π^0 inclusive cut

In the signal mode analysis, we employed the π^0 inclusive cut, which effectively rejected the backgrounds from $\pi^+\pi^-\pi_D^0$ and nuclear interaction events (see Section 4.3.1). This cut might cause over-veto for the $\pi^+\pi^-e^+e^-$ events that had an extra photon accidentally reconstructed as π^0 (with the e^+/e^- pair). Figure 4.23 shows the resultant over-veto probability as a function of the beam intensity in units of the S.E.C. beam monitor. It could affect the final branching ratio by $1.1\% \pm 0.2\%$, but was neglected in the actual analysis. We treated this as a systematic error in the efficiency calculations.

Monte Carlo statistics

In general, the number of Monte Carlo events is limited, and thus it has statistical error. In subtracting the backgrounds in the signal region (see Sec.4.3.3), we used the Monte Carlo events to fix the background shape. The statistical error associated with it has been included as the statistical error of the observed signal events. Here we treat the statistical error of the Monte Carlo events in determining the acceptance and efficiency.

The numbers of reconstructed events are 3617 and 29545, respectively, for the $K_L \rightarrow \pi^+\pi^-e^+e^-$ and $K_L \rightarrow \pi^+\pi^-\pi_D^0$ modes. We found the errors in the acceptance and/or efficiency to be 1.7% and 0.6%, respectively. Summing up in quadrature, we assign 1.8% error in the final branching ratio from this

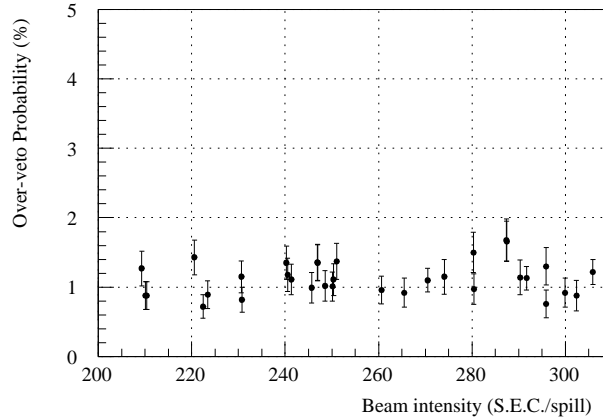


Figure 4.23: The over-veto probability by π^0 inclusive cut for $\pi^+\pi^-e^+e^-$ Monte Carlo events overlaid Trig.4 data. The horizontal axis represents the beam intensity of Trig.4 expressed by S.E.C./spill.

category.

4.5.2 Estimation of the Number of the Events

In this category we treated the systematic errors related to the number of the events $N(\pi^+\pi^-e^+e^-)$ and/or $N(\pi^+\pi^-\pi_D^0)$.

Background subtraction in the final signals

We checked stability of the background subtraction by employing different signal and control regions. Actually, widening the region in the $M_{\pi\pi ee}$ direction, we tried $|M_{\pi\pi ee} - M_{K_L}| < 5\sigma_K$ and $< 7\sigma_K$ instead of $< 3\sigma_K$. In Table 4.4, we list the number of events in the respective regions and the number of the signal events obtained by the same subtraction method (see Section 4.3.3). The errors in the table represent the statistical ones. The maximum change in the number of the signal events was 1.0. We considered this difference as a systematic error (7.4%).

Nuclear interaction

In the final background subtraction, we assumed almost flat shape along θ^2 (actually the shape of $\pi^+\pi^-\pi_D^0$ MC) for the backgrounds. Here we consider the systematic error associated with this assumption. Under this assumption, we estimated the number of background events as follows. We found

Table 4.4: stability of the background subtraction

$M_{\pi\pi ee}$ region	Data		$\pi^+\pi^-\pi_D^0$ MC		After subtraction
	Signal	Control	Signal	Control	
3σ	15	6	1.3	5.2	13.5 ± 4.0^a
5σ	16	13	2.1	7.8	12.5 ± 4.3
7σ	17	18	2.1	8.8	12.8 ± 4.6

^a Statistical error.

6 events in the Helium data in the region of $|M_{\pi\pi ee} - M_{K_L}| < 7\sigma_K$ and $30 \text{ mrad}^2 < \theta^2 < 100 \text{ mrad}^2$. On the other hand, based upon the Monte Carlo simulation, we expect 1.49 events in this region from the $K_L \rightarrow \pi^+\pi^-\pi_D^0$ mode. The discrepancy in the Helium data can be filled with nuclear interactions, since we could explain the backgrounds in the Vacuum data quantitatively by $\pi^+\pi^-\pi_D^0$ MC. Assuming further that nuclear interactions distribute uniformly in the $M_{\pi\pi ee}$ direction, we expect 1.93 events in the ‘‘control’’ region of $|M_{\pi\pi ee} - M_{K_L}| < 3\sigma_K$ and $30 \text{ mrad}^2 < \theta^2 < 100 \text{ mrad}^2$. From this value and the assumption of background shape, we expect 0.48 events of nuclear interaction events inside the signal region. This should be compared with zero event actually observed. In reality, we subtracted out this contribution for simplicity. This treatment is correct as long as the assumed shape of background is correct. Discarding this assumption, we might suppose the other extreme, i.e. the nuclear interaction changed its shape inside the signal region to give zero event. This resulted in 3.6% change in the final branching ratio. Any other shape assumptions made less effects, as long as it is consistent with null event observation in the signal region. We thus assigned 3.6% of the systematic error due to shape assumption of the nuclear interaction.

Contamination by external gamma conversion

The decay mode $K_L \rightarrow \pi^+\pi^-\gamma$ and $K_L \rightarrow \pi^+\pi^-\pi^0(\pi^0 \rightarrow 2\gamma)$ might produce background events when one of the photons converts into an e^+/e^- pair externally. The former becomes the background for the signal mode and the latter for the normalization mode. These processes were again studied by Monte Carlo simulations.

The background contamination due to the $K_L \rightarrow \pi^+\pi^-\gamma$ is found to be less than 1% of the reconstructed $K_L \rightarrow \pi^+\pi^-e^+e^-$. The contamination from the $K_L \rightarrow \pi^+\pi^-\pi^0(\pi^0 \rightarrow 2\gamma)$ is also found to be less than 1% of the reconstructed $K_L \rightarrow \pi^+\pi^-\pi_D^0$. In summary, the contamination due to the

photon conversion process would change the final results by 1.4% at most, and this is treated as a systematic error.

4.5.3 Systematic Error from Other Sources

The final category is related to the current experimental errors on the branching ratios $Br(K_L \rightarrow \pi^+\pi^-\pi^0)$ and $Br(\pi^0 \rightarrow e^+e^-\gamma)$. They had the experimental errors of 1.6% and 2.7% respectively [29]. This could change our final result accordingly. Summing up in quadrature, We assigned a systematic error of 3.1%.

4.5.4 Summary of Systematic Errors

Table 4.5 summarizes our systematic errors, which are divided into three categories.

Table 4.5: Summary of systematic errors in the branching ratio.

	Source	uncertainty
Acceptance efficiency	K_L momentum spectrum	4.8%
	Matrix element	3.9%
	Accidental activity	1.9%
	Monte Carlo statistics	1.8%
	Z distribution of Decay Vertex	1.2%
	π^0 inclusive cut	1.1%
Number of Events	Background subtraction	7.4%
	Nuclear interaction	3.6%
	Contamination from γ conversion	1.4%
$Br(K_L \rightarrow \pi^+\pi^-\pi_D^0)$		3.1%
Total		11.3%

Summing up all the uncertainties in quadrature, the over all systematic error for the final branching ratio was found to be 11.3%.

Chapter 5

Conclusion

In this thesis, the observation of the decay mode $K_L \rightarrow \pi^+\pi^-e^+e^-$ and the experimental measurement of its branching ratio has been reported.

The decay mode $K_L \rightarrow \pi^+\pi^-e^+e^-$ can provide a new testing ground for CP violation. This is because it is expected to occur via a $\pi^+\pi^-\gamma^*$ intermediate state whose two dominant amplitudes are different in CP properties. Thus CP violation may be observed as an interference between the two.

The experiment, called KEK-E162, was conducted with the 12 GeV Proton Synchrotron (PS) at KEK. Data were taken in two distinctive time periods in 1996 and 1997. One period is called “Helium” run and the other “Vacuum” run, representing the condition of the decay volume, respectively. Using only the Helium data, we already reported the branching ratio upper limit, improved by factor 5 at that time [12]. In this thesis, we analyzed almost all available data including the Vacuum one; this has enabled us to establish the decay mode and to measure its finite branching ratio.

The experiment was performed using a neutral beam line at KEK-PS. The detector for the experiment consisted of a magnetic spectrometer system to obtain trajectories and momenta of charged particles, a calorimeter to measure energies and positions of electromagnetic components, a gas Čerenkov counter for an electron identification and trigger scintillation hodoscope counters.

The data analysis was divided into two phases. The first phase was a step to obtain basic physics quantities, such as momentum, energy, vertex position, charge and species of particles, and so on. The second phase was a step to select K_L decay modes by various topological and kinematical cuts. In particular, two modes, the signal mode $K_L \rightarrow \pi^+\pi^-e^+e^-$ and mode $K_L \rightarrow$

$\pi^+\pi^-\pi_D^0(\pi_D^0 \rightarrow e^+e^-\gamma)$, were analyzed and identified.

After various cuts to remove backgrounds, especially, from $\pi^+\pi^-\pi_D^0$ and the nuclear interaction, we finally obtained 15 candidates of $K_L \rightarrow \pi^+\pi^-e^+e^-$ with 1.5 background level. This is a clear evidence of the decay mode $K_L \rightarrow \pi^+\pi^-e^+e^-$. The backgrounds originated most likely from nuclear interactions in the Helium run and from $\pi^+\pi^-\pi_D^0$ in the Vacuum run; the latter has been well understood by the simulation quantitatively as well as qualitatively.

The $K_L \rightarrow \pi^+\pi^-\pi_D^0$ mode was employed to determine the incident K_L flux. This mode is suitable for normalization, since it has a large branching ratio and the same event topology as the signal mode except a photon. The resultant number of the $\pi^+\pi^-\pi_D^0$ reconstructed events was 12212 with less than 1% backgrounds.

In order to determine acceptance and efficiency, we employed Monte Carlo simulations. We note, for calculation of the branching ratio, the acceptance and/or efficiency ratio of the two modes was needed and thus most of uncertainties common to the two modes were expected to cancel out. Finally, based on the 13.5 events identified as the $K_L \rightarrow \pi^+\pi^-e^+e^-$ mode, we determined its branching ratio to be

$$Br(K_L \rightarrow \pi^+\pi^-e^+e^-) = (4.4 \pm 1.3 \text{ (stat.)} \pm 0.5 \text{ (syst.)}) \times 10^{-7} ,$$

where the first (second) error represents statistical (systematic) uncertainty.

This result is consistent with the theoretical prediction [10] as well as the recent experimental measurement based on 36.6 ± 6.8 observed events at FNAL [15]. Finally, we conclude this experiment has established the decay mode $K_L \rightarrow \pi^+\pi^-e^+e^-$.

Appendix A

Monte Carlo Simulation

The Monte Carlo simulation has mainly two functions. One is to calculate detector acceptances and analysis efficiencies of the $K_L \rightarrow \pi^+\pi^-e^+e^-$ and $K_L \rightarrow \pi^+\pi^-\pi_D^0$ modes, which are needed for determination of the branching ratio. The other is to understand backgrounds, i.e. to determine various cuts to select signal and reject backgrounds efficiently and to estimate the expected number of backgrounds remaining in the signal region. Our simulation program was based on GEANT 3.21 [30], which was developed at CERN and having been widely used in particle physics experiments. GEANT is a tool that simulate flights of particles, their decays and interactions with materials.

In this appendix, we describe the detail of the Monte Carlo simulation employed in the analysis. At first, the simulation of K_L decay is described. Next, we make a comparison between the reconstructed $\pi^+\pi^-\pi_D^0$ sample and the corresponding Monte Carlo sample for a cross check of our Monte Carlo system.

A.1 K_L Production and decays

The simulation started with the K_L generation in the production target. The position of the production was determined uniformly in the target. Its momentum direction was also determined uniformly within the solid angle of ± 4 mrad (horizontal) \times ± 20 mrad (vertical) defined by the aperture of the collimator, while its magnitude was determined according to a spectrum shown in Figure A.1. This spectrum was obtained by KEK-E137 group [31] who had used the same beam line and had taken data at the same production angle (2°) as us previous to our experiment. If the K_L decay occurred upstream the entrance of the decay volume, or it passed through the decay

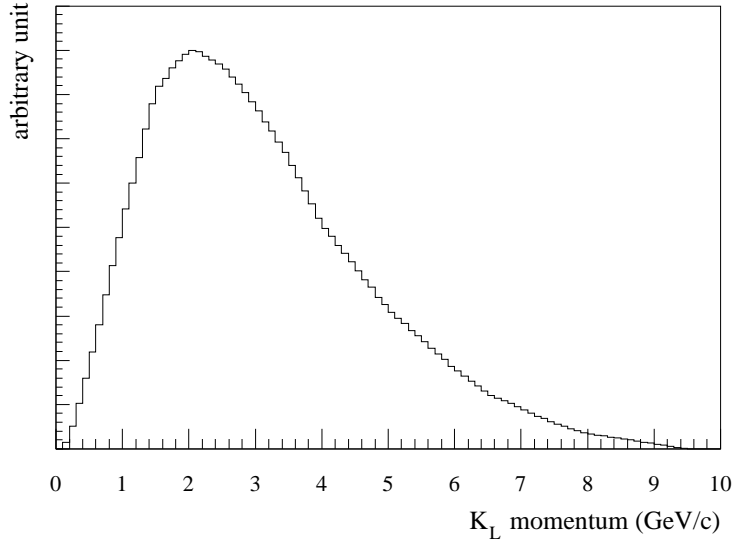


Figure A.1: K_L momentum spectrum employed in the Monte Carlo simulation.

volume, the program went on the generation of a new K_L . Once the K_L decayed in the decay volume, the control of the process moved to the routine which described kinematics of the specific decay mode.

$$K_L \rightarrow \pi^+ \pi^- \pi_D^0$$

The decay mode $K_L \rightarrow \pi^+ \pi^- \pi_D^0$ includes two decay process. In the case of $\pi_D^0 \rightarrow e^+ e^- \gamma$, the Kroll-Wada spectrum [32] was used. In the case of $K_L \rightarrow \pi^+ \pi^- \pi^0$, we used the matrix element \mathcal{M} written by Dalitz plot parameters [29] such as

$$\begin{aligned} |\mathcal{M}|^2 &= 1 + 0.670u + 0.079u^2 + 0.0098k^2 \\ u &= (s_3 - s_0)/m_{\pi^+}^2, \quad v = (s_1 - s_2)/m_{\pi^+}^2 \\ s_i &= (P_K - P_i)^2, \quad s_0 = 1/3(s_1 + s_2 + s_3), \end{aligned}$$

where P_K is the kaon four momentum vector, and P_i are the four momentum vectors of the i -th pion, and $i = 1, 2, 3$ corresponds to π^+ , π^- and π^0 , respectively.

$$K_L \rightarrow \pi^+ \pi^- e^+ e^-$$

In the case of the $K_L \rightarrow \pi^+ \pi^- e^+ e^-$ decay, we employed the distribution obtained by the calculation of the matrix element in Ref.[11]. In this paper,

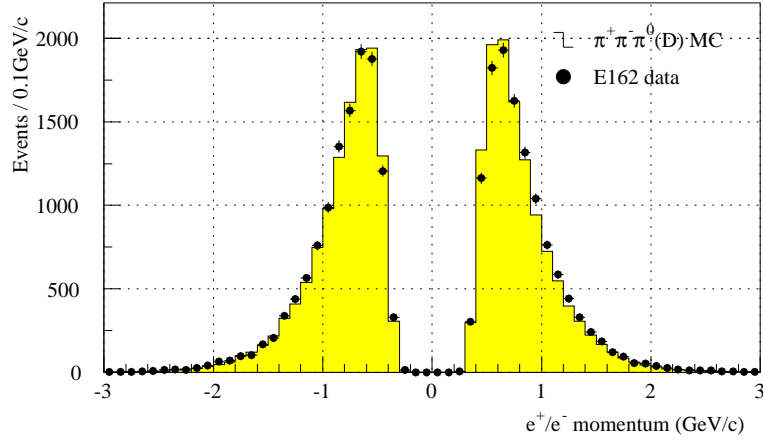


Figure A.2: The comparison of e^+ and e^- momentum distribution for the $K_L \rightarrow \pi^+\pi^-\pi_D^0$ events between the experimental data and Monte Carlo simulation. The sign of the momentum represents the charge of e^\pm .

the matrix element for $K_L \rightarrow \pi^+\pi^-e^+e^-$ is written as

$$\mathcal{M}(K_L \rightarrow \pi^+\pi^-e^+e^-) = \mathcal{M}_{br} + \mathcal{M}_{mag} + \mathcal{M}_{CR} + \mathcal{M}_{SD}, \quad (\text{A.1})$$

where \mathcal{M}_{br} and \mathcal{M}_{mag} are the amplitudes associated with the internal bremsstrahlung and direct M1 emission parts of the $K_L \rightarrow \pi^+\pi^-\gamma$ amplitude. In addition, \mathcal{M}_{CR} is the contribution of K^0 charge radius, as described in Sec.1.1. The last term \mathcal{M}_{SD} is an amplitude associated with the short-distance interaction $s \rightarrow de^+e^-$.

A.2 System Cross Check

Using the reconstructed $K_L \rightarrow \pi^+\pi^-\pi_D^0$ sample, We compared distributions of various kinematical variables with corresponding ones of the Monte Carlo. The resultant distributions are shown in Figures A.2-A.5. As can be seen in figures, both of the actual data and the Monte Carlo simulation agreed well with each other.

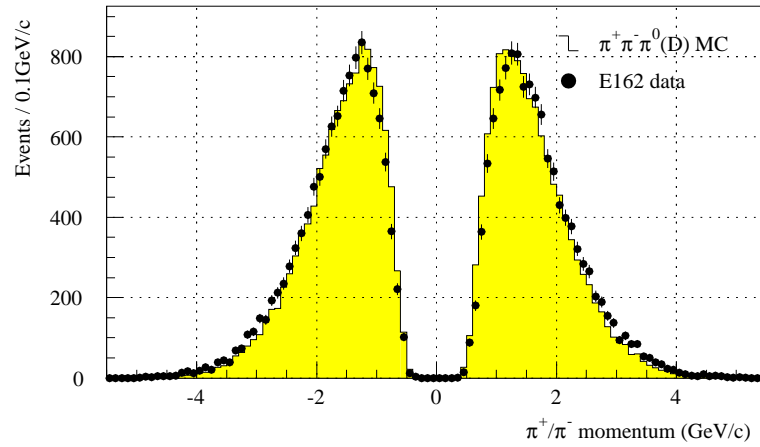


Figure A.3: The comparison of π^+ and π^- momentum distribution for the $K_L \rightarrow \pi^+\pi^-\pi_D^0$ events between the experimental data and Monte Carlo simulation. The sign of the momentum represents the charge of π^\pm .

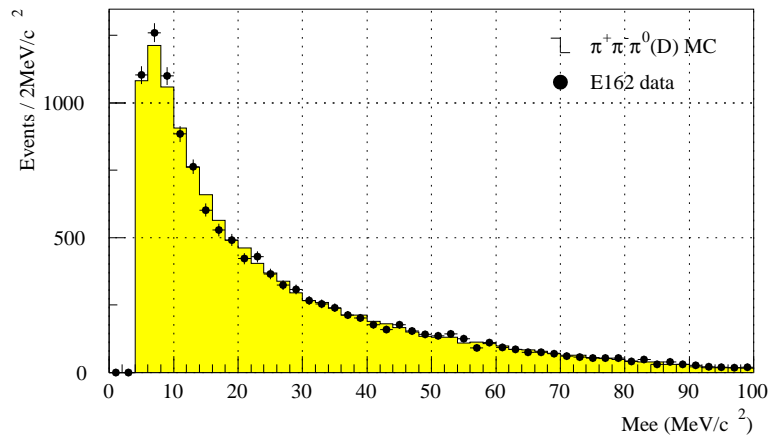


Figure A.4: The comparison of e^+e^- invariant mass distribution for the $K_L \rightarrow \pi^+\pi^-\pi_D^0$ events between the experimental data and Monte Carlo simulation.

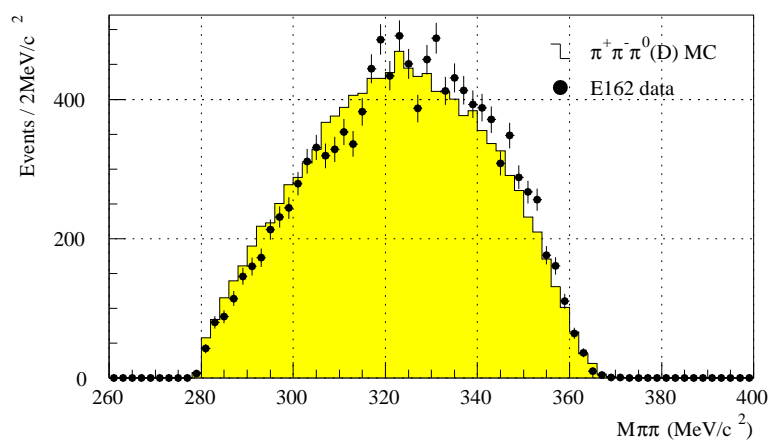


Figure A.5: The comparison of $\pi^+\pi^-$ invariant mass distribution for the $K_L \rightarrow \pi^+\pi^-\pi_D^0$ events between the experimental data and Monte Carlo simulation.

Bibliography

- [1] J. H. Chrestenson *et al.*, Phys. Rev. Lett. **13**, 138 (1964).
- [2] L. Wolfenstein, Phys. Rev. Lett. **13**, 562 (1964).
- [3] A. Alavi-Harati *et al.*, Phys. Rev. Lett. **83**, 22-27 (1999).
- [4] V. Fanti *et al.*, hep-ex/9909022, (September, 1999).
- [5] S. Weinberg, Phys. Rev. Lett. **37**, 657 (1976).
- [6] A. A. Anselm and D. I. D'YAKONOV, Nucl. Phys. B**145**, 271 (1978).
- [7] M. Kobayashi and T. Maskawa, Prog. Theor. Phys. **49**, 652 (1973).
- [8] A. Alavi-Harati *et al.*, hep-ex/9908020, (August, 1999).
- [9] E. J. Ramberg *et al.*, Phys. Rev. Lett. **70**, 2529 (1993).
- [10] L. M. Sehgal and M. Wanninger, Phys. Rev. D**46**, 1035 (1992); *ibid.* **46**, 5209 (E) (1992).
- [11] P. Heilinger and L. M. Sehgal, Phys. Rev. D**48**, 4146 (1993).
- [12] T. Nomura *et al.*, Phys. Lett. B**408**, 445 (1997).
- [13] T. Nomura, Ph.D thesis, Kyoto University, (January, 1998).
- [14] N. Sasao, Proceedings of the SLAC topical conference, (August, 1997).
- [15] J. Adams *et al.*, Phys. Rev. Lett. **80**, 4123 (1998).
- [16] T. Yamashita *et al.*, Nucl. Inst. Meth. A**283**, 709 (1989).
- [17] T. Yamashita *et al.*, Nucl. Inst. Meth. A**317**, 213 (1992).
- [18] O. Sasaki, IEEE Trans. Nucl. Sci. **38**, 281 (1991).

- [19] S. Kubota *et al.*, Nucl. Inst. Meth. A**268**, 275 (1988).
- [20] H. Kurashige *et al.*, IEEE Trans. Nucl. Sci. **35**, 1018 (1988).
- [21] O. Sasaki *et al.*, IEEE Trans. Nucl. Sci. **35**, 342 (1988).
- [22] H. Hinterberger and R. Winston, Rev. Sci. Instr. **37**, 1094 (1966).
- [23] C. R. Kerns, IEEE Trans. Nucl. Sci. **24**, 353 (1977).
- [24] Y. Takeuchi *et al.*, Nucl. Inst. Meth. A**430**, 447-454 (1999).
- [25] K. Murakami *et al.*, Phys. Lett. B**463**, 333 (1999).
- [26] H. Kurasige *et al.*, IEEE Trans. Nucl. Sci. **41**, 1267 (1994).
- [27] T. K. Ohska *et al.*, IEEE Trans. Nucl. Sci. **33**, 98 (1986).
- [28] G. A. Akopdjanov *et al.*, Nucl. Inst. Meth. **140**, 441 (1977).
- [29] Particle Data Group, C. Caso *et al.*, Eur. Phys. J. C**3**, 1-794 (1998).
- [30] Detector Description and Simulation Tool, CERN Program Library Long Writeup W5013.
- [31] T. Akagi *et al.*, Phys. Rev. D**51**, 2061 (1995).
- [32] N. M. Kroll and W. Wada, Phys. Rev. **98**, 1355 (1955).